Dipl.-Ing. Caroline Hiebl, BSc.

Ion Dynamics in the Li-Bearing Thiophosphate Li_6PS_5I and the Phyllosilicate $Li_{0.5}[Mg_{2.5}Li_{0.5}]Si_4O_{10}F_2$

DOCTORAL THESIS

to achieve the university degree of

Doktorin der technischen Wissenschaften (Dr.techn.)

submitted to

Graz University of Technology

Supervisor

Univ.-Prof. Dr. Martin Wilkening

Institute for Chemistry and Technology of Materials

Graz, December 2020

AFFIDAVIT

I declare that I have authored this thesis independently, that I have not used other than the declared sources/resources, and that I have explicitly indicated all material which has been quoted either literally or by content from the sources used. The text document uploaded to TUGRAZonline is identical to the present doctoral thesis.

EIDESSTATTLICHE ERKLÄRUNG

Ich erkläre an Eides statt, dass ich die vorliegende Arbeit selbstständig verfasst, andere als die angegebenen Quellen/Hilfsmittel nicht benutzt und die den benutzten Quellen wörtlich und inhaltlich entnommenen Stellen als solche kenntlich gemacht habe. Das in TUGRAZonline hochgeladene Textdokument ist mit der vorliegenden Dissertation identisch.

_____

Date/Datum, Signature/Unterschrift

Abstract

In order to accomplish the transition from fossil fuel use to the generation of energy via renewable resources, powerful and safe storage systems are essential. Solid-state electrolytes will pave the way for such advanced energy storage systems. Aside from those bigger units, there is a persistent demand for lithium-ion batteries for portable devices. Solid-state batteries offer higher energy densities. Increased densities allow for downsizing the entire system. Hence, such systems are appealing for very small applications. Furthermore, ceramic solid electrolytes enhance the safety of a battery concerning fire hazards and leakage by replacing the conventionally used highly flammable liquid. Thus, the next generation of lithium-ion batteries, utilizing solid ionic conductors, is highly anticipated - not only by the automotive industry but also for portable consumer electronics.

Over the last decade, intensive research efforts led to a large variety of promising solid ion conducting materials. Proper engineering of suitable solid electrolytes, controlling interfacial resistances within the battery cells as well as stability issues are, however, challenging issues to overcome in the next years. For the optimization of synthesis routes, it is crucial to precisely know how different parameters during processing influence ion dynamics within the material.

Therefore, the focus of this thesis was on the one hand to gain some in-depth understanding of the lithium ion transport in nanocrystalline thiophosphate Li_6PS_5I prepared by ball milling, and on the other hand to study the influence of a layered structure on the lithium ion transport in the phyllosilicate $Li_{0.5}[Mg_{2.5}Li_{0.5}]Si_4O_{10}F_2$. The influence of high-energy ball milling on Li^+ dynamics in argyrodite-type Li_6PS_5I was studied by means of ^7Li, ^6Li and ^{31}P nuclear magnetic resonance (NMR), as well as by broadband impedance spectroscopy. As structural disorder, particularly anion site disorder, in halide containing argyrodites yields high ionic conductivities, enhanced ionic conductivity was expected for mechanically treated Li_6PS_5I.

Broadband conductivity spectroscopy and diffusion-induced ^7Li NMR spin-lattice relaxation measurements were also used for the investigation of lithium ion diffusion in layer-structured hectorite-type $Li_{0.5}[Mg_{2.5}Li_{0.5}]Si_4O_{10}F_2$ to determine dynamic parameters such as jump rates and activation energies . This type of structure is considered as a promising starting point since the ions can be transported easily along its lattice planes. Indeed, conductivity isotherms and resistivity data strongly point to a fast 2D ionic conduction process in the hectorite.

In the following, a theoretical introduction of relevant scientific basics as well as the measurement methods used, will be given. The results of the previously mentioned experiments are published in peer-reviewed journals and can be found in chapter (3) of this thesis.

Kurzfassung

Um den Übergang von der Verwendung fossiler Brennstoffe hin zu der Gewinnung von Energie über erneuerbare Ressourcen zu schaffen, sind leistungsstarke und sichere Energiespeichersysteme essenziell. Festkörperelektrolyte können den Weg für solch ausgereifte Energiespeichersysteme ebnen. Neben diesen großen Anwendungen herrscht eine ungebrochene Nachfrage nach Lithium-Ionen-Batterien für mobile Geräte. Festkörperbatterien bieten hohe Energiedichten. Diese Eigenschaft erlaubt es, auch sehr kleine, miniaturisierte Batterien zu entwickeln, die zurzeit auf ein hohes Interesse stoßen. Weiters erhöhen keramische Festkörperelektrolyte die Sicherheit einer Batterie in Bezug auf Brandgefahr und der Gefahr des Auslaufens der herkömmlichen, hochentflammbaren Flüssigelektrolyte. Aus diesem Grund wird die nächste Generation von Lithium-Ionen-Batterien nicht nur von der Automobilindustrie, sondern auch für die Verwendung in tragbarer Unterhaltungselektronik mit Spannung erwartet.

Im letzten Jahrzehnt führten intensive Forschungsbestrebungen zu einer großen Anzahl von vielversprechenden festen ionenleitenden Materialien. Die gezielte Präparation von leistungsfähigen Festelektrolyten, die Kontrolle von Grenzflächenwiderständen innerhalb der Batteriezelle sowie Stabilitätsprobleme stellen eine wesentliche Herausforderung dar, die es in den folgenden Jahren zu lösen gilt. Zur Optimierung von Syntheserouten müssen die Einflüsse unterschiedlicher Prozessparameter auf die Ionendynamik innerhalb des Materials bekannt sein.

Aus diesem Grund lag der Fokus dieser Dissertation einerseits auf dem grundlegenden Verständnis des Lithiumionentransports in dem nanokristallinen Schwefelphosphat Li_6PS_5I, welches durch Kugelmahlen präpariert wurde, und andererseits auf der Erforschung des Einflusses einer Schichtstruktur auf den Lithiumionentransport in dem Phyllosilikat $Li_{0.5}[Mg_{2.5}Li_{0.5}]Si_4O_{10}F_2$.

Der Einfluss des Effektes des Hochenergiekugelmahlens auf die Ionendynamik in Li_6PS_5I mit Argyroditstruktur wurde mittels ^7Li, ^6Li and ^{31}P Kernspinresonanz sowie Impedanzspektroskopie studiert. Strukturelle Unordnung führt bei halogenhaltigen Argyroditen zur hohen Ionenleitfähigkeiten. Durch eine mechanische Behandlung von strukturell geordnetem Li_6PS_5I wurde eine Erhöhung der ionischen Leitfähigkeit erwartet. Impedanzspektroskopie sowie diffusionsinduzierte ^7Li-NMR-Spin-Gitter-Relaxationsmessungen wurden auch für die Untersuchung der Lithiumionendiffusion in dem schichtstrukturierten Hectorit $Li_{0.5}[Mg_{2.5}Li_{0.5}]Si_4O_{10}F_2$ angewandt um dynamische Parameter wie Sprungraten und Aktivierungsenergien zu bestimmen. Im Allgemeinen sind 2D-Ionenleiter vielversprechend und für ihre schnellen Li-Transportpfade entlang der Gitterebenen bekannt. Tatsächlich zeigen die Leitfähigkeitsisothermen und Widerstandsdaten einen schnellen, zweidimensionalen Leitfähigkeitsprozess der Ionen in $Li_{0.5}[Mg_{2.5}Li_{0.5}]Si_4O_{10}F_2$.

Im Folgenden wird eine theoretische Einführung in die relevanten naturwissenschaftlichen Grundlagen sowie die verwendeten Messmethoden gegeben. Die Ergebnisse der zuvor erwähnten Experimente sind bereits in Fachjournalen publiziert worden und in Kapitel (3) dieser Dissertation zu finden.

Inhaltsverzeichnis

1 Introduction

Humanity´s demand for energy seems unlimited. Year after year the world´s energy consumption is increasing. This ongoing trend puts the environment in danger, since most of the energy is still, to a great extent, derived from fossil sources.[1] Climate change is real and human society is reaching a point, where it is impossible to deny it. Albeit some individuals still would like to ignore it for economic reasons. The Paris Agreement on global climate change was ratified by governments worldwide to limit global warming.[2] It is well known that the usage of fossil fuels leads to greenhouse gas emissions disturbing the sensitive balance of our atmosphere. Therefore, the transition to renewable energy sources is urgently needed. But unlike fossil fuels, some renewable energy sources like sunlight or wind are subjected to fluctuations. This intermittent behavior leads to the need for powerful energy storage systems being able to level out peak energy demand times. Here lithium-ion batteries come into play. But of course, they are not limited to balancing power grids, they offer many more application possibilities. Electromobility for example, is another major topic in the fight against climate change. The electrification of cars will make transport independent of fossil fuels. Other applications comprise mobile phones, portables, but also miniature designs for very small devices.

Until today, liquid electrolytes are commonly used in lithium-ion batteries despite being potential fire hazards. Those organic liquid electrolytes are extremely flammable, and leakages are possible. The risk of thermal runaway necessitates security measures, which take up space and weight. These difficulties fueled the search for safe alternatives to liquid electrolytes and paved the way for the investigation of solid electrolyte materials. Solid ionic conductors enable the fabrication of all-solid-state batteries. Their advantages are increased safety, enhanced energy density and the possibility of miniaturization and simplification of the whole system.

In the search of alternatives to flammable liquid electrolytes, a wide range of promising alternatives were explored. Amongst them ceramic materials were intensively investigated. Ceramic solid electrolytes for lithium ion conduction comprise a large number of different candidate materials such as NASICON- and (thio)LISICON-type lithium ion conductors, garnet-structured materials, perovskites, argyrodites, lithium-nitrides, -hydrides and -halides.[3,4]

Fabrication and optimization of solid ionic conductors is however challenging. Albeit some of the investigated materials already show a quite promising ionic conductivity, profound knowledge about ion dynamics needs to be acquired to enhance their conductive properties even further. For the application in all-solid-state batteries, ionic conductivities of several mS cm^{-1} and above over a wide temperature range are needed.[5] For example by controlling grain sizes and structural disorder via the preparation process, one can tailor ionic conductivities. Another option is doping of the ceramic materials, which can change site occupancies within the structure and improve ionic transport.

This thesis deals with the investigation of two different classes of ceramic solid electrolytes in order to understand their ionic transport mechanisms in a better way. The classes analyzed include the thiophosphate Li_6PS_5I and the phyllosilicate $Li_{0.5}[Mg_{2.5}Li_{0.5}]Si_4O_{10}F_2$. They were examined via different spectroscopic techniques such as nuclear magnetic resonance (NMR) and conductivity spectroscopy as well as x-ray diffraction.

The findings of the investigation of the ion dynamics of a halide thiophosphate after nano-structuring via high-energy ball milling, are reported in two publications, which can be found in chapter (3). Structural disorder is supposed to enhance lithium ion conductivity in this group of materials. Therefore, the ball milled sample was studied by means of ^{7}Li NMR spin-lattice relaxation measurements and by broadband impedance spectroscopy. ^{31}P NMR spin-lattice relaxation measurements were used to probe PS_4^{3-} rotational jump processes that may influence Li^+ translational dynamics.

Furthermore, the synthetic fluorohectorite $Li_{0.5}[Mg_{2.5}Li_{0.5}]Si_4O_{10}F_2$, which belongs to the group of phyllosilicates, was analyzed. It serves as a model material for two-dimensional ionic transport along the lattice planes. Again, hectorite-type $Li_{0.5}[Mg_{2.5}Li_{0.5}]Si_4O_{10}F_2$ was investigated by nuclear magnetic resonance spectroscopy as well as broadband impedance spectroscopy to study the lithium ion transport within the material. By using these measurement techniques, the detection of fast 2D ionic conduction processes was possible.

The findings about lithium ion conduction within those ceramics can help scientists and engineers to understand structure-conductivity relationships and encourage the improvement of those materials.

In the following chapter (2), the design and working principle of lithium ion batteries and the basics of diffusion will be discussed. In addition, chapter (2) comprises the fundamentals of analytical methods such as solid-state nuclear magnetic resonance spectroscopy, impedance spectroscopy and x-ray diffraction. Finally, the published results of the investigations of the thiophosphate and fluorohectorite are presented in chapter (3).

2 Theory and Methods

2.1 Electrochemistry

Before going into detail with the fundamentals of lithium-ion batteries, some electrochemical basics will be covered in the following chapter.

An electrochemical cell, where the direct conversion of chemical into electrical energy takes place via reactions at the electrode interfaces under the delivery of electricity, is called galvanic element.[6] It is a voltage source, where the oxidation and reduction processes are separated from each other. Within the cell the charge is transported via ions between the electrodes.[7]

A very well-known example to demonstrate the electronic and ionic fluxes in a galvanic cell is the *Daniell element* consisting of a copper cathode, a zinc anode as well as their metal sulfates as electrolyte solutions (see Figure 1). The electrodes are dipped into the electrolytes and are locally separated in half-cells. An external ion conducting salt bridge connects those compartments. Additionally, an external circuit ensures the exchange of electrons. By closing the circuit, zinc ions go into solution by oxidation of the zinc anode, while copper is deposited at the cathodic side via reduction reactions. Together, they form a redox pair[7]:

$$\mathrm{Zn} \rightarrow \mathrm{Zn^{2+}} + 2\mathrm{e^-} \tag{2.1}$$

$$\mathrm{Cu^{2+}} + 2\mathrm{e^-} \rightarrow \mathrm{Cu} \tag{2.2}$$

$$\mathrm{CuSO_4} + \mathrm{Zn} \rightarrow \mathrm{ZnSO_4} + \mathrm{Cu} \tag{2.3}$$

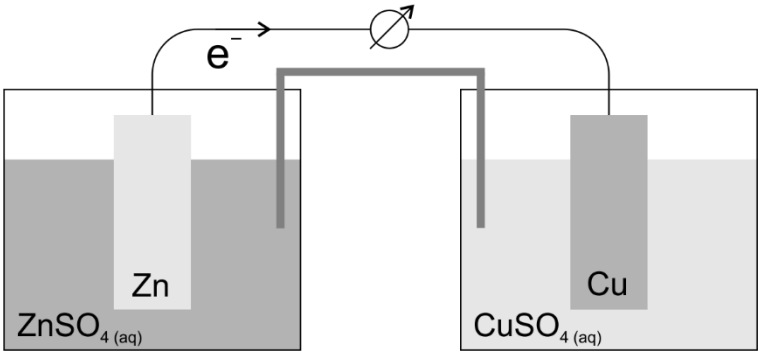

Figure 1: Daniell element - schematic description [7]

Per definition, the electrode, where the oxidation takes place during the discharge process, is called anode. At the cathode the reduction reaction occurs. To define the cell voltage the potential difference between the electrodes at equilibrium conditions can be measured. This means that no reactions must take place and no external electric current can flow. The potential of a half cell - the standard electrode potential - is determined by referencing it to the standard hydrogen electrode. In general, materials for anodes and cathodes are chosen in a way, that their potentials are far away from each other, leading to large potential differences. The standard electrode potential of lithium for example is below −3 V and it has quite a low density, which makes it an attractive anode material.[7]

The change in free energy ΔG of a reversible electrochemical cell is equal to the electrical energy[8]:

$$nFE = -\Delta G, \tag{2.4}$$

with the cell potential *E*, also denoted as the electromotive force (EMF) of the cell and *n*, the number of moles of electrons exchanged during the cell reaction.

The *Nernst equation* shows the dependence of the equilibrium electrode potential *E* of a half-cell on the compound concentration (with $\mathrm{Me^{z+} + ze^- \rightleftharpoons Me}$, $\mathrm{for\ a\ metal-ion\ electrode}$)[7,9]:

$$E = E^0 + \frac{RT}{zF} \cdot ln \frac{c_{Me^{z+}}}{c_{Me}}, \tag{2.5}$$

where E^0 is the standard potential vs. NHE (normal hydrogen electrode), *R* the universal gas constant (8,3 J mol^{-1} K^{-1}), *F* the Faraday constant (96485 C mol^{-1}) and *z* represents the number of electrons exchanged. The cell potential difference of two electrodes in an electrochemical cell can be calculated by $E = E_{\mathrm{cathode}} - E_{\mathrm{anode}}$.[9]

The determination of the converted mass in an electrochemical cell can be done via *Faraday´s laws*. Faraday´s first law states, that the converted mass *m* is directly proportional to the charge exchanged $Q = I \cdot t$. According to the second law, the weight of the elements formed by the same amount of charge, that passes through the cell is proportional to their molar masses but indirectly proportional to the

electrons exchanged $m_1/m_2 = (M_1/z_1)/(M_2/z_2)$.[6] The electronic current *I* and the mass *m* can be related by:

$$m = \frac{Q \cdot M}{zF} = \frac{M \cdot I \cdot t}{zF}. \tag{2.6}$$

Here, *t* denotes the time, *M* the molar mass, *z* the exchanged electrons and *F* is the Faraday constant.[7]

2.2 Secondary Lithium-Ion Batteries

To give the reader some insight into secondary lithium-ion batteries, which are rechargeable, their basic working principle as well as their components will be described in the following chapter.

The simplified standard lithium-ion battery consists of two electrodes, namely an anode and a cathode, separated via the electrolyte material, which is a liquid or solid ionic conductor. The electrodes are both equipped with current collectors that are connected via an external circuit. The fundamental requirement regarding the electrode materials, that enables rechargeable storage systems, is the reversibility of the insertion and extraction of lithium ions (see Figure 2). During charge or discharge of the battery, the electrode materials undergo redox reactions leading to a flow of electrons via the external circuit as well as to ionic conduction through the electrolyte.[10] When a cell is assembled it is usually in a discharged state and must be charged first.[7] When charged the lithium ions are extracted from the cathode and are transported to the anodic side of the battery via the electrolyte while the electrons take the external circuit as can be seen in Figure 2.[10]

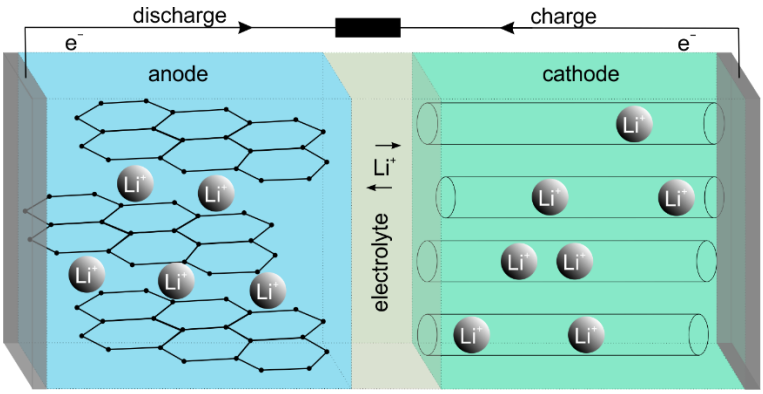

Figure 2: Simplified Li-ion battery model: The electrodes are separated via a lithium conducting electrolyte, current collectors enable electrical conduction via an external circuit.[6,10]

As the main focus of this thesis was on the characterization and development of solid-state ionic conductors, electrode materials and liquid electrolytes will only be outlined briefly to give the reader an idea of the basic concepts.

As electrolyte materials several non-aqueous liquid and solid compounds lie within the realms of possibility. The lithium insertion material serving as the cathode in a lithium-ion battery needs to possess several characteristics. To mention some of them, the insertion cathode should be chemically stable against the electrolyte, the structural changes during charge and discharge need to be reversible and as small as possible and the chemical potential should be high to allow for large cell voltages. In lithium batteries the use of pure metallic lithium anodes causes stability issues. Inorganic liquid electrolytes cause so-called solid electrolyte interfaces (SEI) at the surface of the lithium metal anodes.[10] The SEI is a thin layer, which is an electronic insulator but an ionic conductor.[7] Ionic conductivity is, however, supposed to be relatively low. Despite being passivating and therefore avoiding onward corrosion, it leads to lithium dendrite growth due to non-uniform deposition, and ultimately to a short circuit in the cell. This led to the development of lithium insertion anodes to replace metallic lithium. A commonly used anode compound is graphite. For insertion anodes quite similar requirements as for cathodes must be met (e.g. chemical stability), but in contrast they need a low lithium chemical potential.[10]

As a standard example, the electrode reactions for the discharge of Sony´s commercial lithium ion cell with a graphitic anode and an $LiCoO_2$ cathode from 1991 are shown here[11]:

$$Li_{1-x}CoO_2 + xLi^+ + xe^- \xrightarrow{discharge} LiCoO_2 \tag{2.7}$$

$$Li_xC_6 \xrightarrow{discharge} xLi^+ + xe^- + C_6 \tag{2.8}$$

$$Li_xC_6 + Li_{1-x}CoO_2 \xrightarrow{discharge} C_6 + LiCoO_2 \tag{2.9}$$

2.2.1 Positive Electrode Materials

Over the last decades a variety of electrode materials have been evaluated towards their practicability for lithium-ion batteries. Electrodes are composed of about 90 % active material (of the dry volume) and conductive agents as well as binders and are connected to current collectors. For cathodes the current collector usually is aluminum foil, while for the anodic part it consists of copper foil.[12]

For cathodic active materials, layered oxides with lithium and transition metals like $LiMO_2$ with M = V, Cr, Co or Ni have quite high electrode potentials with respect to metallic lithium. They have a α-$NaFeO_2$ structure, where Li^+- sheets and transition metal oxide sheets alternate, which allows fast two-dimensional Li^+ diffusion.[7,10] A problem regarding their safety is the possibility of a thermal runaway.[13] $LiCoO_2$ is has been used in commercial lithium ion batteries due to offering a high cell voltage (~4 V) and high gravimetric density. A disadvantage of pure $LiCoO_2$ is the relatively low practical capacity because only 0.5 lithium ions per formula unit can be extracted reversibly. Otherwise stability issues arise. Surface modification with for example nano-Al_2O_3 can help to improve this drawback.[7,10,14,15] Other investigated alternatives to $LiCoO_2$ are variations of $LiNi_xMn_yCo_zO_2$.[13]

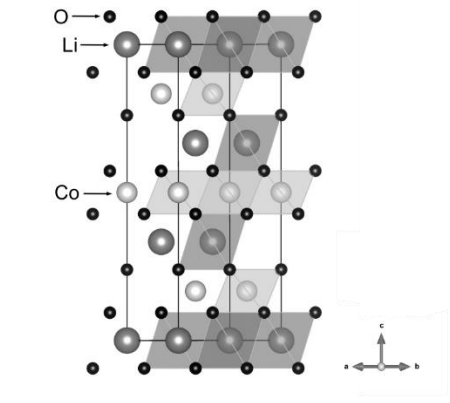

Figure 3: Structure of $LiCoO_2$ (ICSD no. 51767)

Furthermore, spinel oxide cathodes like LiM_2O_4 with M = Ti, V or Mn were studied.[16,17] From an environmental and financial point of view there is an advantage in using manganese in LiM_2O_4 in contrast to cobalt or nickel. Unfortunately, $LiMn_2O_4$ suffers from cyclability problems and lower discharge capacities than its cobalt and nickel counterparts.[7,10] Besides, other spinel oxides such as $Li_4Ti_5O_{12}$ or the phosphor-olivine $LiFePO_4$ were studied for the application as anode materials.[7] $LiFePO_4$ has advantages regarding the cost effectiveness and an environmentally friendly nature in comparison with most of the aforementioned cathode materials. Albeit its high stability during cycling, the low conductivities in this material are detrimental. Nevertheless, these issues are tackled by nanostructuring, coatings and doping.[13]

2.2.2 Negative Electrode Materials

For anodes in lithium-ion batteries carbon stands out because of beneficial characteristics like its low weight and an electrochemical potential almost reaching that of pure lithium.[10] The insertion of lithium ions during charge into the carbon host is reversible and the structure remains intact:

$$Li_xC_n \rightleftharpoons xLi^+ + xe^- + C_n \tag{2.10}$$

This insertion is dependent on many factors such as crystallinity, morphology, and structure of the lithiated carbons. Carbonaceous materials vary in crystallinity. There are so-called graphitic and non-graphitic carbons. The former ones are ordered with carbon atoms building layered planar honeycomb structures (graphene layers), that are interconnected via Van der Waals forces to organized stacks. If the crystallites of the carbon material are disordered, they are referred to as non-graphitic carbons.[7] Figure 4 offers an overview of the synthetic and natural carbonaceous materials, that can be used as anode materials in lithium-ion batteries.[12] Graphite electrodes can take up one lithium atom per 6 carbon atoms (C_6Li).[10] A concomitant phenomenon of carbonaceous materials is the irreversible lithium adsorption when the cell is charged for the first time. This leads to an irreversible capacity loss, which is associated with SEI formation and corrosion phenomena at the electrode. After this, Li^+ can be recovered up to 100% during further cycling. Lithium metal anodes would reach theoretical capacities of 3860 mAh g^{-1}, which is much larger than that of a C_6Li anode with 372 mAh g^{-1}. In contrast to metallic lithium anodes, where SEI formation takes place during each cycle and the electrode surface is repeatedly rebuilt, carbon electrodes are passivated after the first cycle.[7] Also other materials like intermetallic compounds (e.g. Li-Si, Li-Sn, Li-Sb…), nitrides and phosphides were explored in order to find suitable anodes.[10] Lithium alloys suffer from lower energy densities in contrast to pure metal anodes because of the additional weight that comes with the extra metallic species.[7] Another severe problem is the volume change of the host structure that can reach up to 300 % for the silicon-alloy anode. Spinel type $Li_4Ti_5O_{12}$ was also investigated as an alternative to graphite. It offers a long cycle life and due to its high potential versus lithium it is a safer option than graphite.[13]

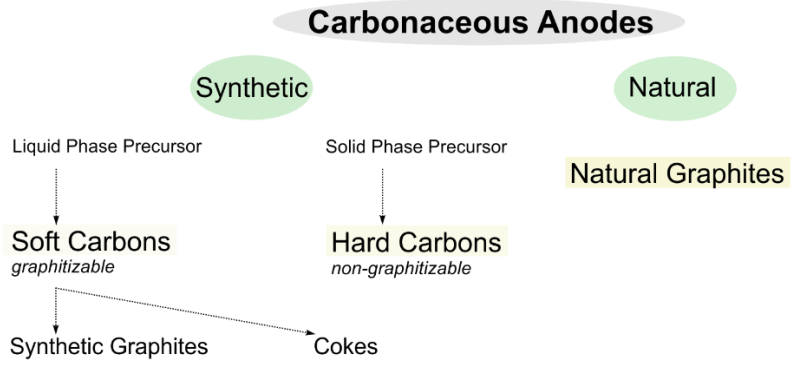

Figure 4: Overview of carbonaceous anode materials [12]

2.2.3 Liquid Nonaqueous Electrolytes

For lithium-ion batteries one can choose from various nonaqueous liquid electrolytes. In general, they consist of a mixture of organic solvents and a lithium containing ionic salt.[7] Criteria that should be met for liquid electrolyte candidates are conductivities being at least in the mS cm^{-1} range, good chemical and thermal stabilities and a large liquid range and electrochemical window, as well as low toxicity and cost.[7,13] Furthermore, short-circuiting should not lead to explosions. Therefore, the desired features also comprise non-flammability.[13] Up to now it is almost impossible to meet all requirements.

The solvents are often mixtures of cyclic and open chain organic compounds. The former ones offer high dielectric constants that are important for the dissolution of the lithium salts, whereas the latter ones serve to reduce the viscosity.[13] The addition of salts can extend the liquid range. Examples for frequently used solvents are ethylene carbonate, propylene carbonate, dimethyl carbonate and ethyl methyl carbonate.[7] Salts for electrolyte mixtures need to show a decent solubility in the solvents and be (electro)chemically stable. In the ideal case, both, solvent and salt, should be economically and environmentally friendly. Salts currently utilized are e.g. $LiPF_6$ and $LiClO_4$.[7] At present, the problem that arises with the use of organic solvents is their hazardous potential due to their high flammability.[13] So far, it is a balancing act between using liquid nonaqueous electrolytes that possess high conductivities and suffering from safety issues. In general, the right electrolyte composition is chosen individually depending on the electrodes used and the intended application.[13] Additionally, some electrode materials would need compatible (liquid) electrolytes, operating at a larger voltage range (> 5 V).[12] To improve the electrolyte system different additives are added. Their purposes are numerous and are ranging from enhancing the SEI formation, protecting the cathode, inhibiting aluminum corrosion or acting as flame retardants to many more.[7] In standard liquid lithium-ion cells, the electrolyte is soaked into a separator membrane. This prevents short circuits by inhibiting any electrical contact between the electrodes.[13] Other electrolytes consist of polymers or glassy structures, but this is beyond the scope of this thesis.

2.2.4 Inorganic Solid Electrolytes

Recent research focuses on the development of solid-state electrolytes for lithium-ion cells. The aim is to replace the currently used organic liquid electrolytes in order to improve the safety and power density of those cells. Solid electrolytes can be fabricated as extremely thin layers and therefore, pave the way for much lighter and smaller systems operating over a wide temperature range.[10] Some of the drawbacks are problems with the charge transfer kinetics leading to interfacial resistances.[18] Apart from the application in battery cells there is a wide range of other research fields solid-state electrolytes can be used for. Amongst them are solid oxide fuel cells, sensors or smart windows.[4] Requirements for a suitable solid electrolyte material usable in electrochemical cells are high lithium ionic conductivity within a reasonable

temperature range, chemical stability regarding the electrode materials and the thermal expansion coefficients should be similar to the electrodes in order to ensure contact. Furthermore, they should be feasible from an environmental and economic point of view and easy to fabricate.[3] In contrast to organic electrolytes, solid-state ionic conductors offer some advantages, e.g. enhanced life-time and safety. Especially the higher thermal stability and lower flammability enable a reduction of safety measures, leading to a simplification of the system.[4]

Lithium ion conducting solids considered as electrolytes vary from crystalline or amorphous/glassy materials to composites. The experimental part of this thesis comprises solid electrolytes of the crystalline section.

Some examples for crystalline solid-state electrolytes are NASICON- and (thio)LISICON-type lithium ion conductors, garnet-structured materials, perovskites, argyrodites, lithium-nitrides, -hydrides and -halides.[3,4] An example for a perovskite is $Li_{3x}La_{2/3-x}TiO_3$ (LLTO) and for sodium super ionic conductor (NASICON)-like structures it is $Li_{1.3}Al_{0.2}Ti_{1.7}(PO_4)_3$ (LATP). Both materials unfortunately suffer from stability problems in contact with metallic lithium.[3] A lithium super ionic conductor (LISICON)-like electrolyte is $Li_{3+x}(P_{1-x}Si_x)O_4$, where the oxygen position can be exchanged with sulfur leading to $Li_{3+x}(P_{1-x}Si_x)S_4$.[4,19] The classes of argyrodites and garnet-like solid electrolytes are described in detail below. Up to now no universal formula for the synthesis of the perfect solid electrolyte has been found. The difficulties lie within the lack of a general route for the enhancement of the lithium ion conductivity as many different structures exist. Substitution may be one way to boost the conductivities, but there are many more factors playing a role. The lattice has to possess the right sizes of sites and channels to encourage lithium diffusion.[4]

Smaller monovalent ions are superior to multivalent ions when it comes to conduction in solids. At ambient temperature low activation energies are key for high ionic conductivities but within a structural family the conductivities can vary widely (5 - 6 orders of magnitude).[4,7] To facilitate ionic transport in the solid electrolyte system, synthesis routes are chosen such that they ensure enhanced lattice structures with adequate defect concentrations and mobilities. All solid-state lithium-ion batteries share one major problem, which is ensuring the constant contact between the solid electrodes and the solid electrolyte. Different thermal expansion coefficients of the materials used, can impair the quality of the contact at the interfaces. For the preparation of solid electrolytes - depending on the nature of the materials used - several procedures are available. Examples are solid-state reactions, wet chemical techniques or sintering. For thick-film electrodes tape casting or screen printing can be applied and for thin-film solutions sputtering, evaporation techniques or also spin-coating are the methods of choice.[7] The key goals for solid-state electrolytes are the increase in energy and power density, long-term stability, safety and facile processing.[20]

In the following, two examples of promising solid-state electrolyte classes, namely argyrodites and garnets, will be described in more detail. For the workgroup in Graz these two classes served as model substances to study the origins of fast ion transport in solids.

2.2.4.1 Garnets

In general, the ideal garnet crystallizes in a face centered cubic structure with space group $Ia\bar{3}d$ and the structure offers a high degree of possible chemical substitutions. The general chemical formula is $A_3B_2(CO_4)_3$ with e.g. A = Ca, Mg, Y La or a rare earth element, B = Al, Fe, Ga, Ge, Mn, Ni or V, C = Si, Ge or AL In this structure the coordination of the site A is eight-fold, of B six-fold and for C it is four-fold with respect to the oxygen ions.[21] The garnet structure is very versatile and allows a broad spectrum of cations, differing in valence state and size, to reside in it without noteworthy alterations of the symmetry.[22]

The class of garnet-type solid ion conductors was first introduced as potential solid-state electrolytes for lithium-ion batteries by Thangadurai *et al.* in 2003. They focused on Nb- and Ta-containing garnet related lithium metal oxides ($Li_5La_3M_2O_{12}$ with M = Nb or Ta), that offer a bulk conductivity of $\sim 10^{-6}$ S cm^{-1} at ambient temperature. Furthermore, they found $Li_5La_3Ta_2O_{12}$ to be chemically stable in contact with elemental lithium.[23] Those findings attracted interest in refining the synthesizing methods and in the search for other compositions that show high ionic conductivities making those materials utilizable in future commercial solid-state battery applications.[21]

So-called lithium stuffed garnets exhibit high ionic conductivities. They contain more than the standard eight cations per formula unit (with 4 - 7 lithium ions pfu). This means, that the cationic species will not only reside on the positions known from stoichiometric garnets.[24] The upper limit of lithium ion content is x = 7.5 for $Li_xB_3C_2O_{12}$ and the highest ionic conductivity is assumed to lie around $x = 6.4 \pm 0.1$.[25] Structural analysis of $Li_5La_3M_2O_{12}$ with M = Nb or Ta via neutron diffraction revealed, that the lithium ions not only occupy tetrahedral (24*d*) but also octahedral (96*h*/48*g*) sites. Those two kinds of coordination polyhedra share faces (each octahedra is connected to two tetrahedra) and allow for very small lithium-lithium distances despite electrostatic repulsion. The octahedra are thought to be distorted if one neighboring tetrahedral site is occupied and therefore, the octahedral lithium ion tends to reside closer to the shared face with an empty tetrahedral site. On the distorted octahedral site, the repulsion between the lithium ions can be reduced (see Figure 5). This is also referred to as “clustering of lithium ions”. The octahedra are connected by sharing edges among each other. The interconnection of tetrahedra and octahedra leads to a three-dimensional lithium diffusion pathway.[26] With an increase in the lithium content in the garnet structures, the number of octahedrally coordinated lithium cations increases, while vacancies form at the tetrahedral sites.[24] Not only the amount of lithium but also other factors like the sintering temperature during the preparation play a part regarding the ionic conductivity of garnet related materials.[27]

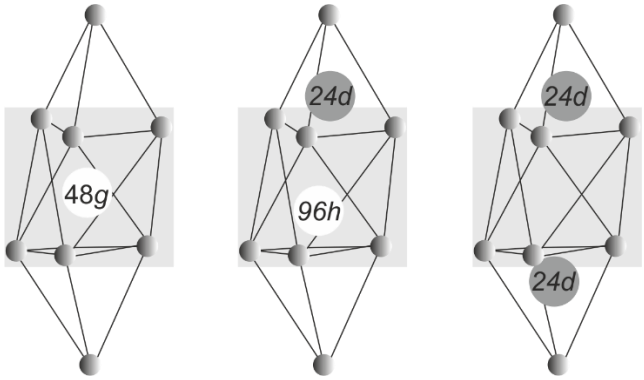

Figure 5: Possible lithium ion distributions over the tetrahedral (24*d*) and octahedral (48*g* and 96*h*) sites in $Li_{5+x}La_{3-x}A_xM_{2-y}B_yO_{12}$ with the ions A = divalent, B = tri-/tetravalent and M = pentavalent.[21]

In 2007, Murugan *et al*. investigated cubic $Li_7La_3Zr_2O_{12}$ (LLZO) as a promising candidate for the application as solid ionic conductor (crystallographic structure seen in Figure 6). The high ionic conductivity ($\sim 10^{-4}$ S cm^{-1} at ambient temperature) as well as chemical and thermal stability of this material and the good prospects in terms of an economic and environmental point of view were emphasized.[22] LLZO can also exist in a tetragonal phase. While the annealing temperature used by Murugan *et al*. for cubic LLZO was 1230 °C, Awaka *et al*. synthesized tetragonal LLZO using much lower temperatures (980 °C).[22,28] This tetragonal polymorph (space group $I4_1/acd$) shows an ionic conductivity, that is about two orders of magnitude lower than that of the cubic structure at room temperature. Lithium cations reside on three different sites - tetrahedral 8*a*, distorted octahedral 16*f* and 32*g*. The tetrahedral and octahedral sites are completely ordered (lithium atoms and vacancies), which could be the reason for diminished ionic conductivity.[28] In order to successfully synthesize LLZO in the cubic modification, the preparation process is crucial. Choosing the right temperatures and number of calcination steps is essential. Another factor is the use of Al_2O_3 crucibles during the sintering process. Otherwise tetragonal LLZO is obtained. It is assumed that aluminum stabilizes the cubic modification. This was verified by the NMR experiments of Buschmann *et al.* They were able to show that aluminum resides at the 24*d* sites and that its distribution will increase the lithium disorder during sintering.[29] As the cubic phase of undoped LLZO is not stable at ambient temperature, DFT calculations revealed that via doping (with e.g. Al^{3+}) Li^+ vacancies are formed because of charge compensation.[30,31] The tetragonal modification is lower in energy due to an ordered lithium sublattice, where all the lithium sites are either filled or empty, and therefore, the repulsion between the lithium cations is reduced. In contrast to this, in the cubic phase it is disordered, which means the lithium sites are partially occupied. As a result of the vacancy formation caused by Al^{3+} doping, a transition to the cubic phase can take place. The free energy is lowered and an increase in entropy can be seen. This will most probably happen at an alumina concentration of x = 0.2 with $Li_{7-2x}Al_xLa_3Zr_2O_{12}$ (at zero temperature).[31] Also other cations like Ga^{3+} were investigated for supervalent doping of the LLZO structure. In Ga-LLZO with space group *I*-43*d* (for $x > 0.07$ with $Li_{7-3x}Ga_xLa_3Zr_2O_{12}$), Ga^{3+} is thought to occupy the tetrahedral 12*a* lattice site.[30]

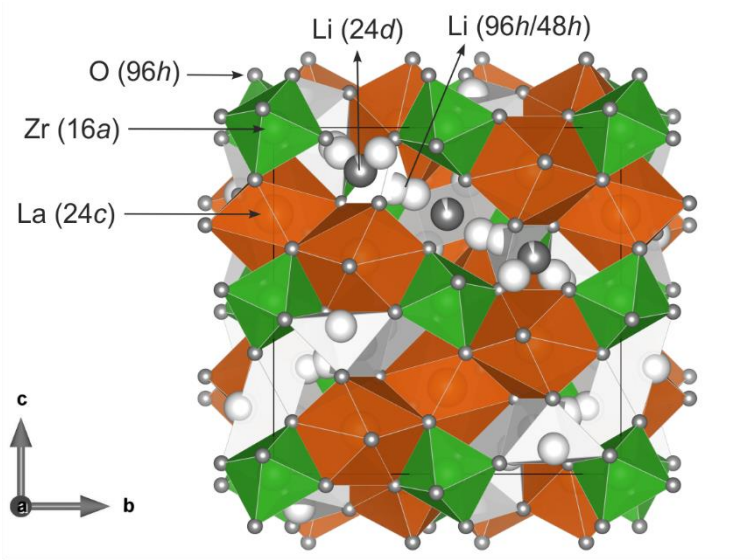

Figure 6: Crystallographic structure of cubic $Li_7La_3Zr_2O_{12}$ ICSD no. 422259

A good overview about the history of the development and current challenges of garnet-like structures for the use as lithium ion conductors in solid-state batteries can be found in the review articles of Thangadurai[21], Zeier[32] and Liu[33].

Garnet Degradation

Despite the reported chemical stability of garnet-related materials, especially in contact with metallic lithium anodes, there is evidence for H^+/Li^+ exchange reactions in contact with humidity or immersion in water. In 2010 Nyman *et al*. tried to increase the ionic conductivity by decreasing the tetrahedrally bound lithium of the Li_5-phases $Li_5La_3M_2O_{12}$ with M = Nb or Ta via heat treatment and aqueous procedures. Their NMR studies indicated that the aqueous H^+/Li^+ exchange of powder samples yielded a depopulation of the less mobile tetrahedral lithium positions. During the exchange process in the aqueous solutions an increase in its pH-value can be observed, which is attributed to the H^+ exchange (= formation of LiOH).[34] With an increase in the lithium content of garnet-like structures and therefore, an increase in the lithium ion concentration in the octahedral sites, the H^+/Li^+ exchange takes place to a smaller degree. This was shown for $Li_{5+x}Ba_xLa_{3-x}Nb_2O_{12}$ after water treatment at room temperature. For $Li_5La_3Nb_2O_{12}$ the exchange was 89% complete. The exchange reaction in this material can be reversed by 5M $LiNO_3$ and it was demonstrated that also the ionic conductivity can be recovered. Furthermore, the cubic structure remains unchanged as verified by powder x-ray diffraction.[35] Another study used organic acids as proton source for $Li_{5+x}Ba_xLa_{3-x}Nb_2O_{12}$. As for the study using water, the degree of protonation decreased with dopant concentration in the garnet-like structure. This clearly indicates that tetrahedral positions preferentially undergo protonation. The H^+/Li^+ exchange was shown to reach 100% using glacial CH_3COOH for undoped $Li_5La_3Nb_2O_{12}$ without any phase transformation.[35] Ma *et al*. investigated the influence of aqueous solutions on LLZO. In contrast to the previously mentioned garnets, the conductivity did not decrease. This was attributed to the preference for the octahedral 96*h* site over the tetrahedral site for hydrogen exchange. The 48*g* site

was occupied by hydrogen only to a small degree and the 24*d* site was left untouched. Even under an exchange rate of 63.6% the Ia3d structure was preserved. For protonated LLZO the reversed reaction was demonstrated using a 2 M LiOH solution. These findings reinforced the approach of using garnet-structured materials as solid separators protecting the anode in aqueous lithium ion batteries.[36] Another aspect to consider is the grain size of the garnet-samples. Smaller grain sizes of Al-LLZO show a better chemical stability in terms of Li_2CO_3 formation during air exposure at ambient conditions than larger grained ones. (LiOH formed during the H^+/Li^+ exchange with water reacts with CO_2 leading to the formation of Li_2CO_3 at the sample surface.) These findings were attributed to the difference in alumina distribution. In smaller grains the alumina stays within the bulk, whereas it is found in the grain boundaries of larger grains. Alumina seems to preserve the garnet from undergoing a reaction with water and the concurrent formation of LiOH. According to DFT calculations, smaller grains are less affected.[37] Parameters like the temperature during synthesis influence the density of the garnet materials. Protonation reactions of cubic $Li_{6.6}La_3Zr_{0.}6Ta_{0.4}O_{12}$ with a higher density take place to a smaller extent.[38] Focused ion beam secondary ion mass spectroscopy on $Li_{6.55}Ga_{0.15}La_3Zr_2O_{12}$ immersed in water (100 °C, 30 min) showed a proton exchanged region of up to 1.35 µm in depth.[39] Hofstetter *et al.* published an excellent overview of the stability of lithium-rich garnets in contact with humidity, carbon dioxide and metallic lithium.[40]

2.2.4.2 Argyrodites

The general formula of argyrodites is $A_{12-m-x}^{+}(M^{m+}\ Y_4^{\ 2-})Y_{2-x}^{2-}X_x^-$ with A = Li, Cu, Ag, M = Si, Ge, Sn, P, As, Y = O, S, Se, Te, X = Cl, Br, I and $0 \leq x \leq 2$.[41] The first known fast ionic conductor amongst the argyrodites was Ag_8GeS_6.[42] As for our studies halogenated thiophosphates were investigated, this group of materials will be discussed in more detail.

In general, Li_7PS_6 shows an enhanced ionic conductivity if it is halogen substituted. Such a partial substitution of sulfur can stabilize the high temperature cubic phase at ambient temperature. Otherwise Li_7PS_6 is found to crystallize in an orthorhombic phase at lower temperatures.[18] Those synthetic lithium containing argyrodites, proposed for the use as solid ionic conductors, crystallize in a cubic unit cell with the space group $F\bar{4}3m$, with the general formula Li_6PS_5X with X = Cl, Br or I.[4] This type of halide containing argyrodite was first synthesized and analyzed by Deiseroth *et al*. in 2008 and can reach ionic conductivities up to 10^{-3} to 10^{-2} S cm^{-1}.[42] PS_4^{3-} tetrahedra (with the sulfur position called "S1") are isolated at the 4*b* sites. The halogen atoms substitute the other sulfur positions ("S2" at 4*a* or 4*d*). Lithium ions can be found at tetrahedral interstitial sites (48*h* and 24*g*) formed by "S2" and halogen positions, which are only partially occupied.[4,18,42,43] The lithium ions diffuse via hexagonal cages built by those partially occupied interstitial sites.[4] Twelve 48*h* sites are located around one 4*c* site giving the impression of a cage.[18] For the X = Cl, those cages surround the halide ions and for the iodide analogue they surround the sulfur anions.[4] Lithium ion diffusion can take place via three possible jumping pathways, namely 48h-24g-48h called "doublet jump" and 48h-48h, which occur either within

(intra-cage jump) or between (inter-cage jump) the cages.[18] Li_6PS_5I suffers from a much lower conductivity than the chloride and bromide counterparts.[4] This might be attributed to the lithium distribution and disorder in the sublattices (S^{2-}/Cl^- and S^{2-}/Br^-) of Li_6PS_5Cl and Li_6PS_5Br. In Li_6PS_5I the iodide and sulfide atoms are on different positions due to the larger size of I^- leading to an ordered structure.[44] Contrarily in the other two halide thiophosphates, the chloride, bromide and sulfide atoms share three positions with each other.[42] The substitution of sulfur with halogen ions results in the formation of lithium vacancies as a consequence of charge compensation. While chloride and bromide are distributed over 4a and 4d sites, iodide is only found at 4a having an influence on the conductivity (see Figure 7 for Li_6PS_5).[18,43]

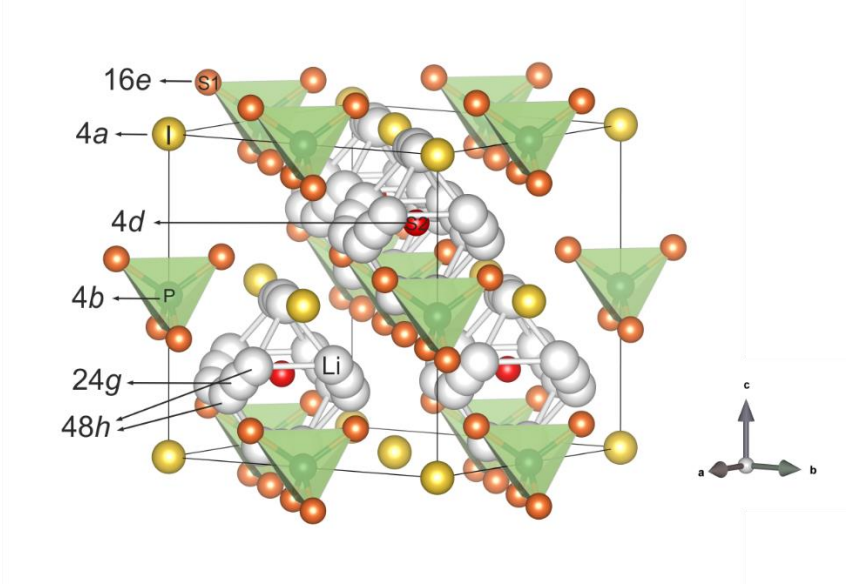

Figure 7: Crystallographic Structure of Li_6PS_5I ICSD no. 259212, adapted from Hanghofer *et al.* [43]

In the case of Li_6PS_5Br the greatest extent in this occupational mixing can be found at the crystallographic sites of S2 and X.[42] A study showed that inter-cage jump processes cannot take place in ordered Li_6PS_5I leading to a diminished long-range ionic conductivity.[45] ^{31}P NMR spectroscopy revealed the influence of rotational PS_4^{3-} jumps on lithium diffusion. The lattice constant of Li_6PS_5X is decreasing from I to Br to Cl. Therefore, Li_6PS_5I has a soft lattice, where those rotational jumps are not dependent on the lithium ion translation. In contrast, for Li_6PS_5Cl the rotational jumping of PS_4^{3-} is slower and might interact with the aforementioned inter-cage jumps of the lithium ions. Both processes take place on a similar time scale. Due to the high lithium ion conductivity, for the Br^--compound the ideal parameters regarding lattice parameters, site disorder and rotational jumping are met.[43] In order to optimize lithium ion conducting argyrodites it is crucial to understand those structure-transport relationships in detail. Kraft *et al*. investigated the influence of a soft-anion lattice on the ionic transport in Li_6PS_5X (X = Cl, Br, I). By changing the polarizability of the anion framework in this compound as a model system, they were successful in demonstrating that a softer lattice is not automatically leading to high ionic conductivities. Going from Cl to Br to I the lattice gets softer. For softer lattices the activation energy E_a as well as the Arrhenius pre-factor σ_0 drop. The latter one

though diminishes the conductivity. In the case of iodine containing Li_6PS_5X the activation energy starts to increase again because of the lack of site disorder leading to a decrease in ionic conductivity. The ideal composition amongst those halide ones was found to be $Li_6PS_5Cl_{0.5}Br_{0.5}$.[46] One way to increase lithium ion conduction in halide argyrodites is substitution. Aliovalent doping of Li_6PS_5I with germanium leads to very high conductivities in the mS cm^{-1} range. In $Li_{6+x}P_{1-x}Ge_xS_5I$ an increase in the dopant concentration causes anion site disorder.[47] Most likely the site disorder enables a flattening of the energy landscape.[48] Also other compositions of $Li_{6+x}M_xSb_{1-x}S_5I$ (M = Si, Ge, Sn) were analyzed already reaching ionic conductivities of up to 24 mS cm^{-1}. Besides the anion site disorder, a Li^+ cation site disorder is promoted leading to a reduced activation energy barrier and concerted ion migration.[49] This shows the need for a deep understanding of composition and structure relationships with ionic transport in those materials.

2.3 Theory of Diffusion in Solid State Matter

One of the prerequisites for a working lithium-ion battery is ionic transport. Without sufficient diffusion of charge carriers through the electrolyte and electrode materials, these battery components would not be suitable for the application in batteries.

Simplified, diffusion can be described as the process, where a species (e.g. atoms, ions, molecules) moves around in a medium. [50] The atomistic view is, that diffusion in crystalline materials is linked to defects, that allow for a higher mobility of the species.[51] It can be quantified by a diffusion coefficient via the determination of the concentration of the species at certain distances from its origin at a specific temperature.[50] The rate of bulk diffusion, which indicates diffusion through the volume of a sample, is isotropic for gases, liquids, amorphous as well as cubic solids but anisotropic for other crystalline materials. When talking about diffusion in solid matter, it is necessary to consider the structural aspects of the crystalline material as well as the types of defects present.[50] In the following chapter the basics of diffusion in solids, crystal defects and the mechanisms of diffusion in crystalline materials will be described. I recommend the books of Tilley[50] and Mehrer[52] for further reading.

2.3.1 Basic Principles

The fundamentals of diffusion can be explained by the so-called *continuum theory*, which is a phenomenological approach based on Fick´s laws, and by the *random walk theory*, which is based on the Brownian motion and describes diffusion from a macroscopic point of view.[52]

2.3.1.1 Continuum Theory

The diffusion processes in the *continuum theory* are described by *Fick´s laws*. The basis is the concentration gradient as a driving force for diffusion by equalizing the concentrations of the species present. *Fick´s first law* (represented in Figure 8) describes the diffusion flux J_x for isotropic media, therefore the problem can be reduced to one dimension:

$$J_x = -D\frac{\partial C}{\partial x}\ , \tag{2.11}$$

with D as the diffusion coefficient of the species of interest in [m^2s^{-1}] and C as the concentration. The negative sign shows that J_x and the concentration gradient point in opposite directions.[52]

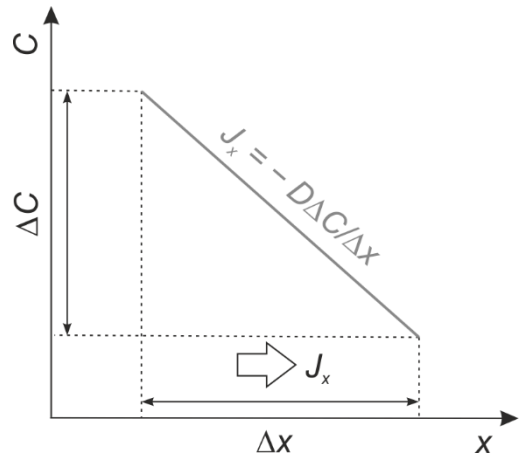

Figure 8: Fick´s first law. Representation of the concentration as function of distance with a diffusion flux in the direction of the lower concentration[52]

For three dimensions *Fick´s law* can be rewritten as follows:

$$\boldsymbol{J} = -D\boldsymbol{\nabla}C\,, \tag{2.12}$$

with $\boldsymbol{J}$ as the diffusion flux vector and $\boldsymbol{\nabla}C$ as the concentration gradient vector.[52] Under non-steady-state conditions the diffusion flux and concentration are generally dependent on time and position. For systems, that do not undergo any reactions, the total number of particles does not change. This results in the *continuity equation*[51,52]:

$$-\boldsymbol{\nabla}\cdot\boldsymbol{J} = \frac{\partial C}{\partial t}\,. \tag{2.13}$$

Combining *Fick´s first law* and the *continuity equation*, we get *Fick´s second law*, the so-called *diffusion equation*[52]:

$$\frac{\partial C}{\partial t} = \boldsymbol{\nabla}\cdot(D\boldsymbol{\nabla}C)\,. \tag{2.14}$$

If we assume D to be constant, we get:

$$\frac{\partial C}{\partial t} = D\Delta C\,, \tag{2.15}$$

with Δ**,** the the Laplace operator. This equation is also referred to as *linear diffusion equation* for systems, where the diffusivity is independent of concentration. It can be solved at defined boundary and initial conditions.[52]

2.3.1.2 Random Walk Theory

In contrast to gases and liquids, where the particles diffuse more or less along free paths, atomic jumping processes in crystalline lattices take place between (interstitial) lattice sites.[52] A simple model to describe bulk diffusion in solids is the *random walk the*ory relying on randomly jumping particles.[50] Only a series of successful jumps yields macroscopic diffusion. Via the *Einstein-Smoluchowski* relation the diffusion coefficient of Fick´s laws can be linked to the mean square displacement $\langle R^2 \rangle$ of particles performing a random walk (see Figure 9). For uncorrelated diffusion in a three dimensional crystalline media the following applies[52]:

$$D_r = \frac{\langle R^2 \rangle}{6\tau}, \tag{2.16}$$

with D_r as the diffusion coefficient of a random, uncorrelated walk and τ as the mean residence time of an atom at a specific location.

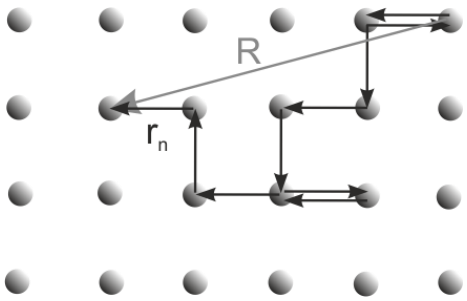

Figure 9: Several individual jumps leading to a total displacement *R*.[51]

Previously we assumed, that diffusion in solids occurs via independent jumps. This does not apply for all diffusion mechanisms. For example, in the case of vacancy diffusion a kind of "memory effect" comes into play leading to correlated behavior. This can be modeled by the so-called *correlation factor f*:[52]

$$f \equiv \frac{D^*}{D_r}. \tag{2.17}$$

D^* denotes the diffusion coefficient of a tracer atom, which performs a correlated motion.[50,52] Combining equation 2.16 and 2.17 leads us to:

$$D^* = f\frac{\langle R^2 \rangle}{6\tau}. \tag{2.18}$$

For true random walks without any correlation f equals 1. The diffusion coefficient D usually is dependent on the temperature T and the activation enthalpy of diffusion ΔH. It is described by the Arrhenius equation:

$$D = D_0 \exp\left(-\frac{\Delta H}{RT}\right), \tag{2.19}$$

with D_0 as the "frequency factor" determined by:

$$D_0 = D_0' \exp\left(-\frac{\Delta S}{R}\right). \tag{2.20}$$

The pre-exponential factor D_0' includes several parameters such as geometric factors, the correlation factor, the lattice parameter squared and the attempt frequency. ΔS denotes the diffusion entropy.[51]

Atomic Jumping

Atoms in crystal lattices vibrate approximately at the Debye frequency with values around 10^{12} to 10^{13} Hz. This can be regarded as the attempt frequency of an atom for a jump (10^{12} to 10^{13} attempts per second). The number of successful jumps Γ of an atom per second follows an Arrhenius behavior and can be written as:

$$\Gamma = \nu \exp\left(-\frac{\Delta G^M}{k_B T}\right), \tag{2.21}$$

with ν the attempt frequency of an atom at its equilibrium site and k_B the Boltzman constant (= $1{,}38 \cdot 10^{-23}$ JK^{-1}). In this context, a successful jump describes an atom having enough energy to overcome the barrier between its equilibrium position and neighboring sites. The atomic jumping process is thermally activated, which means the lattice vibrations increase with temperature. The *Gibbs free energy of migration* ΔG^M describes the magnitude of the energy barrier:

$$\Delta G^M = \Delta H^M - T\Delta S^M, \tag{2.22}$$

with H^M the enthalpy of migration and S^M the entropy of migration.[50,52] Fluctuations in the thermal energy enable diffusion by atoms that are otherwise not able to get past the energy barrier.[51] A visualization of the energy landscape within a crystal lattice is given in Figure 10.

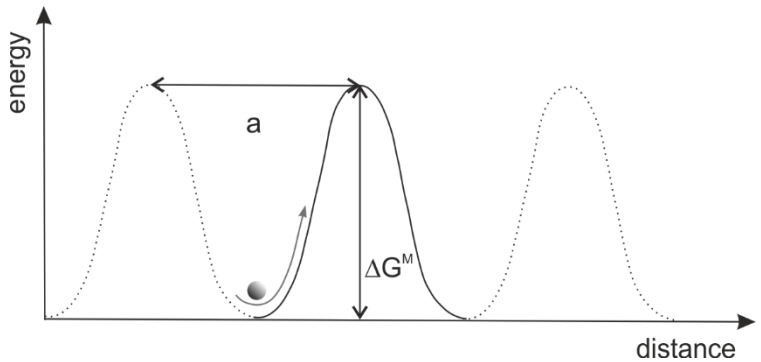

Figure 10: Example of an energy landscape during diffusion of an atom through a lattice with the atomic distance *a*; maxima reflecting "bottlenecks" between stationary atoms with ΔG^M, the Gibbs free energy of migration.[50]

2.3.2 Defects in Crystalline Materials

A perfect crystal without defects can only exist at zero Kelvin (state of zero entropy). At higher temperatures defects will form and the entropy increases.[53] The so-called defect hierarchy allows for a classification of defects in crystalline materials with respect to their dimensionality, it is shown in Table 1.[54] In crystalline materials the presence of defects is essential for the diffusion of atoms through the lattice. Higher dimensional diffusion along dislocations and grain boundaries is usually much faster than via point defects, which consist of one or a few atoms.[50,55] As most solid materials are polycrystalline, they contain grain boundaries within their structure. At grain boundaries, interfaces with different crystal orientations meet. Examples for one-dimensional defects are edge and screw dislocations. They arise from deformation or the crystal growth itself and - unlike point defects - they do not exist at the thermodynamic equilibrium.[53,54] Another type of defects are three-dimensional volume defects, e.g. pores.[54]

Table 1: Classification of defects[54]

Dimension	Type	Example
0	Point defect	Vacancy
1	Line defect	Dislocation
2	Planar defect	Grain boundary
3	Volume defect	Pore

Point Defects – Frenkel & Schottky

There are two common types of point defects in crystalline solids that preserve an overall charge neutrality in the volume of an ionic crystal, namely the *Frenkel* and *Schottky disorders*.[52]

In a thermodynamic equilibrium ionic defects are present in the pure crystal lattice. They are referred to as intrinsic defects. In contrast, extrinsic defects define impurity atoms at substitutional or interstitial sites at the host lattice.[53] The *Frenkel defect* describes an equal amount of vacancies and self-interstitials. For reasons of simplification we will now only consider binary ionic compounds (CA) consisting of a cation and anion species of equal charges of the opposite sign. In the case of a cation on site C_C a *Frenkel defect* yields a vacancy on the cation site V_C and a self-interstitial I_C. They are denoted as *Frenkel pair*[52]:

$$C_C \rightleftharpoons V_C + I_C \tag{2.23}$$

A *Schottky defect* indicates the same number of vacancies in the anion and cation sublattice. Analogous to the *Frenkel pair* a cation and anion vacancy are called *Schottky pair*[52]:

$$C_C + A_A + 2 \text{ new lattice sites} \rightleftharpoons V_C + V_A \tag{2.24}$$

Besides vacancies and interstitials other point defects such as misplaced atoms, interacting defects, called associated centers, substitutional atoms and electronic defects can be present in the crystal lattice.[54]

2.3.3 Diffusion Mechanisms

For atoms in a crystalline lattice, several mechanisms of diffusion exist. Knowing the mechanism present allows for a better control of the ionic transport properties via mechanochemical engineering of a potential solid electrolyte material. The crystal lattice predefines the possible diffusion pathways. Therefore, unlike in gases and liquids, the mechanisms of diffusion in crystalline solids can be described in a very simple way. There are several influencing factors for atomic jumping such as the crystal structure, the properties of the diffusing species and the presence of defects. In the following section the main diffusion mechanisms will be described.[52]

Interstitial mechanism

This mechanism is characterized by solute atoms (self-interstitials, impurities, dopants) that are much smaller than the host lattice atoms. Therefore, they can migrate through the system via the interstitial sites.[50,52] There is no permanent displacement of the host lattice after migration of a solute atom from its starting point to an adjacent interstitial site. In general, interstitials preferably occupy octahedral and tetrahedral lattice sites.[51] The interstitial mechanism is not defect mediated and its diffusion coefficient is generally very high.[52]

Interstitialcy mechanism

Another option for interstitials to move through a crystal lattice is the interstitialcy mechanism. If an interstitial atom has a similar size as the host atoms, the interstitial atom can move to replace a host atom at a regular site, which in turn jumps to an interstitial site. Therefore, this mechanism involves the simultaneous movement of two atoms.[50,52]

Collective mechanism

Here, the solute atoms are of quite the same size as the host atoms leading to a substitutional mechanism via a concurrent movement of several atoms. Defects do not play a role here either.[52]

Vacancy mechanism

This mechanism involves atoms of a lattice site that jump into adjacent vacancies. Because it looks like the vacancy diffuses through the lattice, it is called vacancy mechanism.[50,52] The actual pathway of the diffusing species is related to the crystal structure. Attractive as well as repulsive forces influence the probability to find an adjacent vacancy.[50,51] Another related type is the divacancy mechanism, where several vacancies can form agglomerates at thermal equilibrium and move concurrently. Mono- and divacancy concentrations are temperature dependent.[52]

Interstitial-substitutional mechanism

For this mechanism an atomic species B can be located on an interstitial site B_i or substitutional site B_s of a crystal lattice. The solubility of the atomic species is lower on the interstitial site than on the substitutional one, whereas the diffusion rate is higher on the interstitial site. Depending on the pathway involved there are two different types – the *dissociative mechanism* and the *kick-out mechanism*. The former one uses vacancies V[52]:

$$B_i + V \rightleftharpoons B_s \tag{2.25}$$

and the latter one uses self-interstitials A_i:

$$B_i \rightleftharpoons B_s + A_i \tag{2.26}$$

Linking ionic conductivity to the diffusion coefficient

Schottky defects enable the vacancy diffusion mechanism, and Frenkel defects allow for interstitial, interstitialcy and vacancy diffusion. In a crystalline sample more than one point defect species can contribute to the overall diffusion coefficient.[50] Ceramic materials used as solid-state ionic conductors need high rates of ionic movement yielding large conductivities. The ionic conductivity is defined by:

$$\sigma = \sum_i q_i N \mu_i \,, \tag{2.27}$$

with μ_i the mobility, N the number of mobile defects and q_i the effective ionic charge. The *Nernst-Einstein equation* links the ionic mobility μ and the ionic conductivity σ to the diffusion coefficient D:

$$\mu = \left(\frac{q}{k_\mathrm{B}T}\right) D \quad \text{and} \quad \sigma = \left(\frac{Nq^2}{k_\mathrm{B}T}\right) D \,. \tag{2.28}$$

This linkage is only possible if the ionic conductivity and the diffusion employ the same mechanism.[54]

2.4 Analytical Methods

2.4.1 Impedance Spectroscopy

Impedance Spectroscopy (IS) has become an essential non-invasive analytical technique in materials research due to its versatile nature. There is a large field of applications in semiconductor industry, for corrosion studies, battery and fuel cell development, and also for biological systems testing.[56] In solid state battery research, IS is mainly used to investigate the macroscopic ionic mobility of charge carriers. An IS experiment enables the operator to determine the ionic conductivity (σ) of the sample as well as complex parameters such as impedance (Z^*), permittivity (ε^*) and modulus (M^*) as function of frequency. The frequency range usually varies from 10^{-2} to 10^{7} Hz. In order to distinguish between different regions within ceramics (e.g. grain boundaries and bulk), one can take advantage of their different frequency dependencies by having a look at the magnitude of their capacitance values.[57] For a more in-depth look into the fundamentals of IS, please see references of Irvine[57] and Lvovich[58].

2.4.1.1 Measurement Setup and the Basics of Complex Impedance

For a typical impedance measurement, the sample is pelletized and equipped with a thin layer of blocking electrodes (usually made of Au) before being placed between two electrodes (see Figure 11). After applying a sinusoidal AC voltage signal U with a small amplitude U_0 at the frequency v, a phase (φ) shifted sinusoidal current response with a different amplitude I_0 can be measured (see Figure 12).[58] This can be repeated at a broad range of frequencies as well as at varying temperatures in order to derive other parameters, e.g. activation energies of different processes.

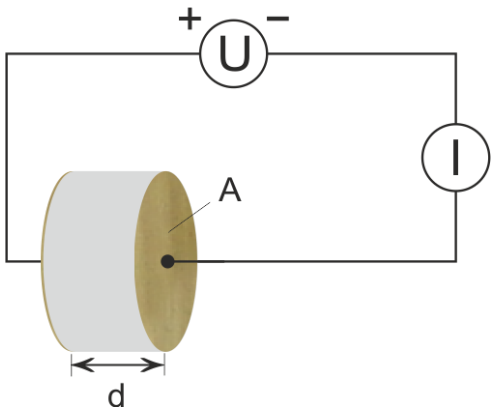

Figure 11: Simplified measurement setup of an impedance experiment. The sample is placed between two identical electrodes with an area *A* at a distance *d*. A sinusoidal AC voltage is applied to the sample resulting in a phase shifted current response, which is recorded.[58]

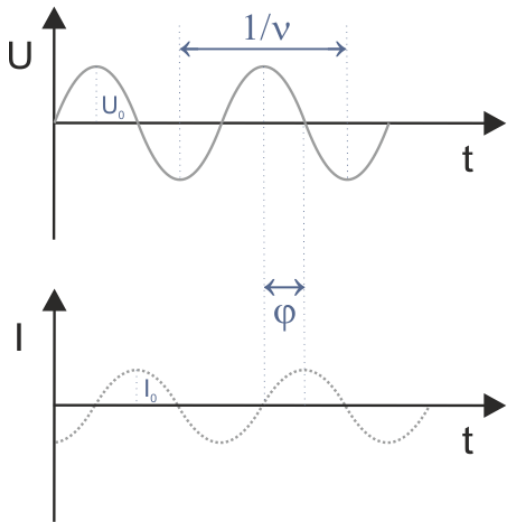

Figure 12: Schematic representation of a sinusoidal voltage input *U* and current response *I* at a certain frequency *ν* as functions of time *t*. *I(t)* has a phase shift of ϕ, U_0 and I_0 are the corresponding amplitudes of the signals.[58]

The general form of the voltage input as function of time is:

$$U(t) = U_0 \sin(\omega t)\,, \tag{2.29}$$

where ω is the radial frequency (ω = 2πν).

The current output as function of time follows:

$$I(t) = I_0 \sin(\omega t + \varphi)\,, \tag{2.30}$$

where φ denotes the phase shift.

The complex impedance can now be written as the ratio of voltage input and current output as it is known from *Ohm´s law*:

$$Z^* = \frac{U(t)}{I(t)} = \frac{U_0 \sin(\omega t)}{I_0 \sin(\omega t + \varphi)} = |Z| \frac{\sin(\omega t)}{\sin(\omega t + \varphi)}. \tag{2.31}$$

Euler´s relationship now allows to express the impedance as a complex function so it can be represented in the complex plane as shown Figure 13:

$$e^{j\varphi} = cos(\varphi) + jsin(\varphi)\,. \tag{2.32}$$

The voltage input and current output considering *Euler´s relationship* in a rewritten form:

$$U(t) = U_0 e^{j\omega t}\,, \tag{2.33}$$

$$I(t) = I_0 e^{j\omega t - j\varphi}\,. \tag{2.34}$$

This leads to a new expression for the complex impedance:

$$Z^* = \frac{U(t)}{I(t)} = |Z|e^{j\varphi} = |Z|(cos\varphi + jsin\varphi) = Z' + jZ'' \text{ and } tan\varphi = \frac{Z''}{Z'}, \qquad (2.35)$$

with φ as the phase angle at a certain radial frequency (ω), which is defined as the ratio of the imaginary (Z´´) and real part (Z´) of the impedance.

The real part of the impedance describes the capability of a material resisting the current flow, while the imaginary part describes the capability to store electrical energy. Complex impedance can describe both, the resistive and capacitive characteristics of a material.[58]

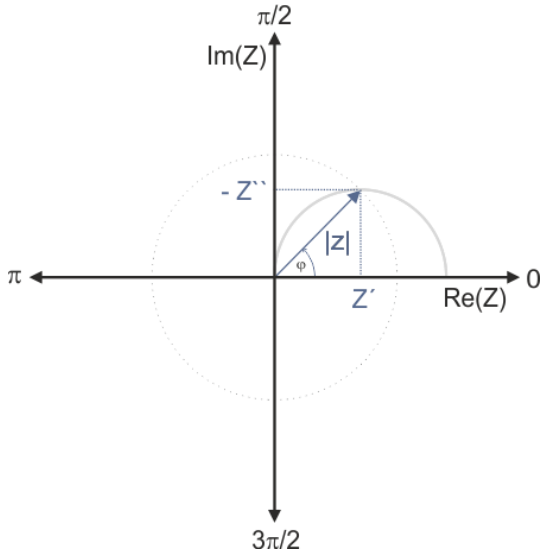

Figure 13: Argand diagram. Complex impedance *Z* plotted as a function of rectangular (*Z´, Z´´*) and polar (*|Z|, ϕ*) coordinates.[59,60]

2.4.1.2 Further important Quantities related to Impedance

There are further quantities related to impedance, which can be obtained via IS measurements. They are referred to collectively as "*immittances*". Those complex impedance-related properties are the admittance Y^*, the permittivity ε^* and the modulus function M^*.[59]

The complex admittance is in inverse proportion to the impedance:

$$Y^* = \frac{1}{Z^*} = Y' + jY'' . \qquad (2.36)$$

The relative permittivity can be related to the material polarization density P via the *Debye Equation*[58]:

$$P = (\varepsilon - 1)\varepsilon_0 V , \qquad (2.37)$$

where V denotes the applied electric field and ε_0 is the dielectric permittivity of the free space. Like the impedance and admittance, permittivity can be written as a complex quantity:

$$\varepsilon^* = \varepsilon' - j\varepsilon'' . \tag{2.38}$$

In dielectrics the real part ε' (= 1/Z''), also called "dielectric constant", displays the energy storage capacity. The imaginary part ε'' (= 1/Z'), referred to as "loss factor", displays the ionic conduction capability. Those two quantities can be derived from a dielectric measurement with a setup as it is shown in Figure 11, via the following equations[58]:

$$\varepsilon' = \frac{Cd}{\varepsilon_0 A}, \tag{2.39}$$

$$\varepsilon'' = \frac{d}{RA\omega\varepsilon_0} = \frac{\sigma}{\omega\varepsilon_0} = \frac{1}{\rho\omega\varepsilon_0}, \tag{2.40}$$

where *C* denotes the capacitance, *d* the distance between the two electrodes, *A* the electrode area, *σ* the conductivity, *ρ* the resistivity and *R* the sample resistance.

For the investigation of ionic conductors, the determination of the conductivity is most important. Like complex impedance, the complex conductivity can also be defined via a real (σ') and an imaginary part (σ'')[52]:

$$\sigma^* = \sigma' + j\sigma'' , \tag{2.41}$$

and can be related to the complex impedance as follows:

$$\sigma^* = \frac{1}{Z^*} \cdot \frac{d}{A}. \tag{2.42}$$

Finally, the complex modulus M*, which is the inverse of the complex permittivity, is[58]:

$$M^* = \frac{1}{\varepsilon^*} = M' - jM'' = j\omega\varepsilon_0 Z^* = -\omega\varepsilon_0 Z'' + j\omega\varepsilon_0 Z' . \tag{2.43}$$

2.4.1.3 Interpretation and Representation of Impedance Spectroscopy Data

Scientists and engineers can choose between different options for the representation of the data derived by impedance spectroscopy. By visualizing the data, different processes within the material can be distinguished, and data analysis is facilitated.

Nyquist Plot

The most common visual representation chosen for impedance data, are *Nyquist plots*. Here, the negative imaginary part of the impedance (- Z'') is plotted versus the real part of the impedance (Z') (see Figure 14). This results in a graph with a semicircle-like shape. Under ideal conditions, for a polycrystalline sample equipped with blocking electrodes and measured in a setup as it was discussed above (see Figure 11), the following *Nyquist plot* is obtained:

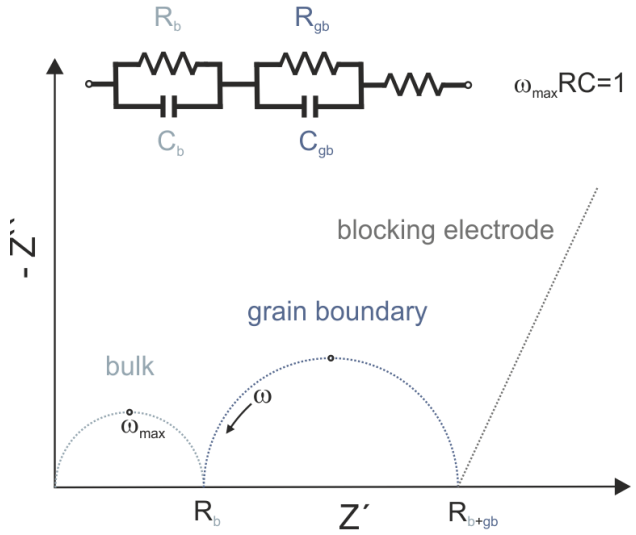

Figure 14: Nyquist plot; imaginary part of the impedance (*-Z´´*) versus the real part of the impedance (*Z´*); responses of bulk, grain boundary and blocking electrode visible; the angular frequency is increasing going from the right to the left; corresponding equivalent circuits at the top of the figure; see text for further explanation.[57,61]

An element in the *Nyquist plot* can be assigned to processes that occur in a certain region of the measurement cell. Bulk and grain boundary responses are usually represented as semicircles, whereas ion blocking electrodes appear as a spike at lower frequencies (see Figure 14).[52] The shape of the semicircle provides insight if only one or multiple activation-energy controlled processes are present. If only one process is present, the semicircle shows an "ideal" shape (= symmetrical).[60]

The elements displayed on a *Nyquist plot* can be described by equivalent circuits (see Figure 14). Complex impedances from diffusion processes in bulk and grain boundaries, that appear as semicircles in the plot, can be described by an ohmic resistance *R* and a capacitance *C* in parallel[52]:

$$Z^* = \frac{R}{1 + i\omega CR}. \tag{2.44}$$

Regional differences in the material can be seen by characteristic relaxation times. The relaxation time τ for a region can be derived by the product of its resistivity and capacitance:

$$\tau = RC\,. \tag{2.45}$$

By using the *Nyquist plot*, the DC resistance *R* can be deduced from the intersection of the semicircle with the abscissa. The capacitances *C* for each region can be calculated as follows:

$$\omega_{max} = (RC)^{-1}\,. \tag{2.46}$$

The angular frequency ω_{max}, called frequency of maximum loss, is shown in Figure 14 by black dots at the maximum of each arc. Knowing the magnitude of the capacitances *C* can help to identify different regions of a specimen as shown in Table 2.[57]

Table 2: Identification of phenomena in specimens via capacitance values.[57]

Capacitance [F]	Underlying Phenomenon
10^{-12}	bulk
10^{-11}	minor, second phase
$10^{-11} – 10^{-8}$	grain boundary
$10^{-10} – 10^{-9}$	bulk ferroelectric
$10^{-9} – 10^{-7}$	surface layer
$10^{-7} – 10^{-5}$	sample - electrode interface
10^{-4}	electrochemical reactions

Keeping Table 2 in mind, the thickness of grains is typically much larger than for grain boundaries. By looking at the equation for a parallel plate capacitor, the capacitance must be much smaller for the bulk of a specimen ($d_{bulk} > d_{gb}$)[57]:

$$C = \varepsilon_0 \varepsilon \frac{A}{d}\,. \tag{2.47}$$

In solid-state ionics there are two further parameters, namely the *charge diffusion coefficient* and the *Haven ratio*, that can be used for data assessment of materials. The *charge diffusion coefficient* can be linked to the DC conductivity from impedance spectroscopy via the *Nernst-Einstein relation*[52]:

$$D_\sigma = \frac{\sigma_{\mathrm{DC}} k_{\mathrm{B}} T}{N_{\mathrm{ion}} q^2}\,, \tag{2.48}$$

with the charge density N_{ion}, the electrical charge *q* and the Boltzmann constant k_B (= 1,38*10^{-23} JK^{-1}). The charge diffusion coefficient is no real diffusion coefficient in a Fickian meaning. It rather transforms the DC conductivity into a parameter with the dimensions of a diffusion coefficient. In that way the *Haven ratio* can be formed by the ratio of the tracer diffusion coefficient D^* and the charge diffusion coefficient[52]:

$$H_R = \frac{D^*}{D_\sigma}\,. \tag{2.49}$$

Conductivity Isotherms and Dielectric Representation

Besides the *Nyquist plot*, another option for data representation is plotting the real part of the conductivity versus the applied frequency at different temperatures. Such *conductivity isotherms* can help to identify different ion transport mechanisms in different regions of the specimen. Additionally, a so-called *dielectric representation*, where the real part of the permittivity is plotted versus the applied frequency can be chosen for data evaluation (see Figure 15)

At low frequencies there is a decrease in ionic conductivity and a steep increase in permittivity that originate from interfacial phenomena at the ion blocking electrodes. The accumulation of ions at the electrodes is also called *electrode polarization*. With increasing frequency, the conductivity reaches a frequency independent section caused by the random hopping motion of ions.[62] This part of the conductivity isotherm is also referred to as DC-plateau and represents long-range ion transport.[52] Via the relation $\sigma_{DC}T \propto \exp(-E_A/(k_B T))$ the activation Energy E_A of this process can be deduced.[63] At slightly higher frequencies also the permittivity reaches a plateau. This corresponds to changes in dipole moments.[64] After the DC-plateau the conductivity isotherm becomes frequency dependent again and follows *Jonscher´s power law*[65,66]*:*

$$\sigma' = \sigma_{DC} + A\nu^n \,. \tag{2.50}$$

In this equation A denotes a temperature-dependent parameter and n can vary between 0 and 1. The *dispersive region,* seen in Figure 15, depicts correlated ion motion at short times.[52,62] At the highest frequencies in the double-logarithmic plot the conductivity isotherm enters a linear regime. This section is called *nearly constant loss* (NCL) because of the nearly frequency-independent dielectric loss for this frequency range.[67] The permittivity values decrease due to faster polarization processes.[62]

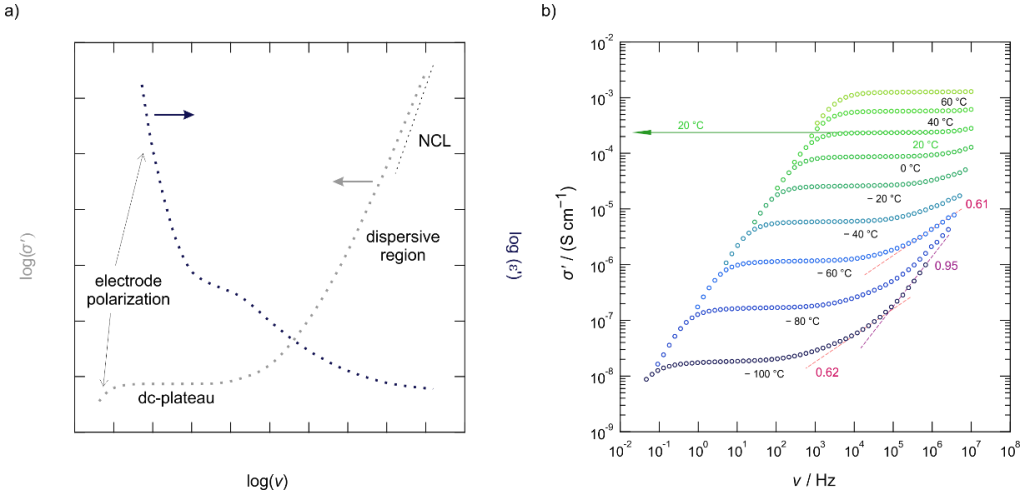

Figure 15: Data representation; **a)** conductivity isotherms and dielectric representation with their characteristic regions[64] **b)** conductivity isotherms at different temperatures of nanocrystalline Li_6PS_5I (from our publication[68], see chapter 3)

2.4.2 Solid-State Nuclear Magnetic Resonance Spectroscopy

Besides electric charge and mass, atomic nuclei have other essential physical properties, namely magnetism and its related property spin. They can be used to derive molecular information. The interaction of atomic nuclei with magnetic fields pave the way for a powerful spectroscopic method - Nuclear Magnetic Resonance (NMR) Spectroscopy.[69] Nuclear magnetic resonance methods are applicable in a wide field, e.g. in disciplines like medicine, chemistry and biochemistry.[70] Besides impedance spectroscopy, NMR spectroscopy can provide further insight into ion dynamics of materials for battery research. In contrast to x-ray diffraction, where only crystalline solids can be analyzed, solid-state NMR can also be used for the structural analysis of inhomogeneous and amorphous samples.[71] I recommend the books of Friebolin[70], Keeler[72] and Duer[71] for a more in-depth look into this topic.

2.4.2.1 Theoretical Basics of NMR Spectroscopy - The Vector Model

Before diving deeper into different measurement techniques and data interpretation, the vector model will be used to explain the theoretical basics of NMR spectroscopy. For a detailed look into the quantum mechanical formalisms of NMR, I recommend reading the book of A. Abragam.[73]

NMR spectroscopy relies on the interaction of an external magnetic field with the magnetic moments $\boldsymbol{\mu}$ of the atomic nuclei. The sum of all the magnetic moments of a probed nucleus in a specimen is called magnetization $\boldsymbol{M}$, which is determined during an NMR measurement.[71] In the following vectors are written in bold letters.

$$\boldsymbol{M} = \sum_i \boldsymbol{\mu_i} \tag{2.51}$$

Before an external magnetic field is applied, the individual magnetic moments are oriented randomly, which means that there is no net magnetization.[72] Nuclear magnetic moments can be linked to the nuclear spin angular momentum **I** via the following equation[71]:

$$\boldsymbol{\mu_i} = \gamma \boldsymbol{I_i}\,, \tag{2.52}$$

where γ is a constant [rad s^{-1} T^{-1}], called the *gyromagnetic ratio*, which differs for each type of nucleus. Its value can be positive or negative and it defines the nuclide´s detection sensitivity (large values indicate a good sensitivity).[69–71]

The spin of a particle is an intrinsic property.[69] The net nuclear spin angular momentum $\boldsymbol{I}$ can be calculated via:

$$|\boldsymbol{I}| = \sqrt{I(I+1)}\hbar\,, \tag{2.53}$$

where the nuclear spin quantum number I can take integer and half-integer values (0, 1/2, 1, 3/2,…6) and $\hbar$ is the reduced Planck´s constant (=$h/2\pi$).[69,70] If I is zero, the nucleus has no nuclear magnetic moment and can thus not be detected via means of NMR spectroscopy.[70]

If an external magnetic field $\boldsymbol{B_0}$ is applied, the magnetic moments align along this field due to an energetic preference over time. This process is called *relaxation*. Usually, $\boldsymbol{B_0}$ is oriented along the z-axis in the laboratory frame of reference. Therefore, at the equilibrium state, there is a net magnetization in the sample along this coordinate (see Figure 16). The magnetic moments rotate around the external field $\boldsymbol{B_0}$. The frequency of the precession of the magnetization around $\boldsymbol{B_0}$ at a constant angle is called the *Larmor frequency* ω_0[71,72]:

$$\omega_0 = -\gamma \boldsymbol{B_0} . \tag{2.54}$$

The sign of ω_0 can either be positive or negative depending on the gyromagnetic ratio, which leads to a clockwise (-) or anticlockwise (+) precession of μ.[69]

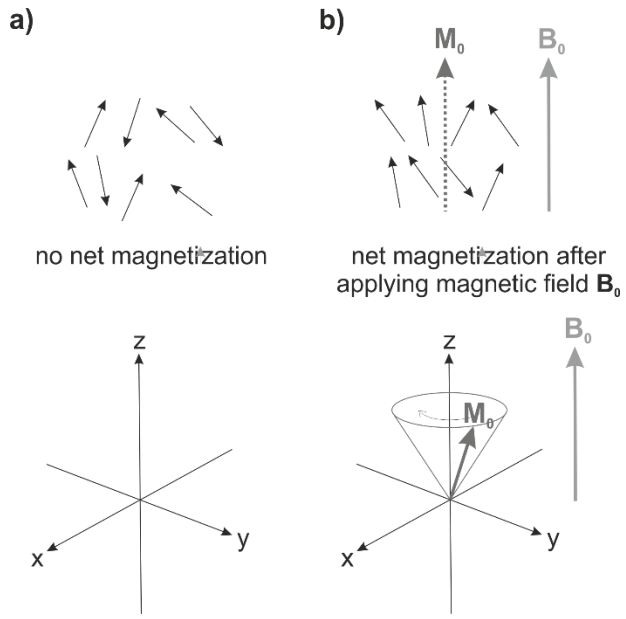

Figure 16: a) in the absence of an external magnetic field, there is no net magnetization. The individual spins are randomly oriented. **b)** If an external magnetic field $\boldsymbol{B_0}$ is applied, the spins try to align themselves along this field as it is energetically preferable. A net magnetization builds up and the net magnetization vector $\boldsymbol{M_0}$ precesses around the direction of $\boldsymbol{B_0}$ at the Larmor frequency.[71,72]

In an external magnetic field $\boldsymbol{B_0}$ the nuclear spin angular momentum $\boldsymbol{I}$ precesses around the z-axis. Due to the discrete number of allowed projections of $\boldsymbol{I}$ on z we derive:

$$I_z = m\,\hbar , \tag{2.55}$$

with the magnetic quantum number *m* (m = I, I-1, …-I), which can have (2I+1) different values. This means that I_z can have (2I+1) different orientations in the magnetic field, also referred to as “directional quantization”.

In turn, the nuclear magnetic moment can be rewritten as follows[70]:

$$\boldsymbol{\mu_z} = m\,\gamma\,\hbar\,. \tag{2.56}$$

Furthermore, the magnetic dipoles in a magnetic field can have (2I+1) possible energy states, namely the *nuclear Zeeman levels.*[70] Those usually degenerated sublevels are split in the presence of a magnetic field $\mathbf{B_0}$, leading to an energy separation (= *nuclear Zeeman splitting*, see Figure 17). The energy of each level can be calculated via[69]:

$$E = -\mu_z\,\boldsymbol{B_0} = -\boldsymbol{m}\,\gamma\,\hbar\,\boldsymbol{B_0}\,. \tag{2.57}$$

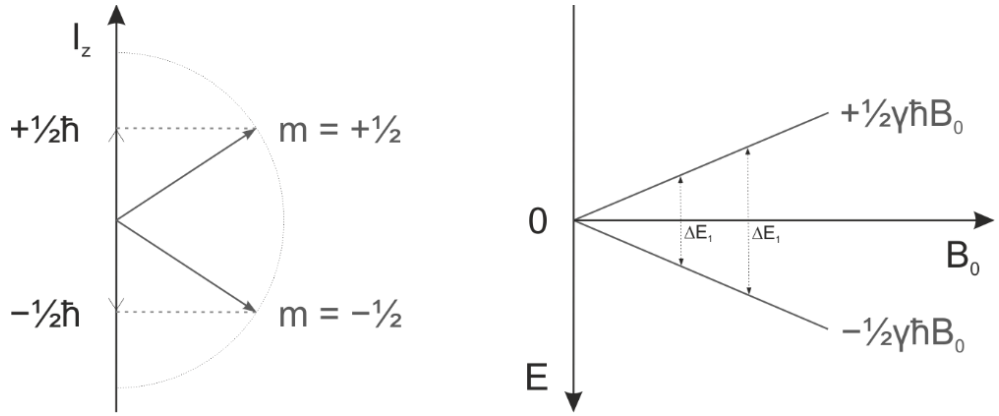

Figure 17: Zeeman splitting of a nucleus with *I* = ½ in the presence of an external magnetic field $\boldsymbol{B_0}$. The larger $\boldsymbol{B_0}$, the greater the energy difference between the energy levels[70].

To enable transitions between the energy levels during an NMR experiment, the electromagnetic waves need a specific irradiation frequency for each nucleus, namely the Larmor frequency ω_0. Only transitions between adjacent energy levels can occur ($\Delta m = \pm 1$).The energy difference ΔE is calculated according to[70]:

$$\Delta E = \gamma\,\hbar\,\boldsymbol{B_0} = \hbar\,\omega_0 = h\,\nu\,. \tag{2.58}$$

The distribution between different energy states can be described by Boltzmann statistics, according to[70]:

$$\frac{N_\beta}{N_\alpha} = e^{\frac{-\Delta E}{k_B T}} = e^{\frac{-\gamma\hbar B_0}{k_B T}}\,. \tag{2.59}$$

N_α and N_β represent the respective temperature dependent occupations for the nuclei with *I* = 1/2 of the lower and upper energy levels α and β.

2.4.2.2 Radio frequency pulses, effective magnetic field and pulse angle

In order to move the magnetization away from its precession direction around the z-axis, the so-called *resonance condition* has to be met. Since $\boldsymbol{B_0}$ is a very powerful magnetic field and cannot be switched off. Therefore, a second small magnetic field $\boldsymbol{B_1}$, that is resonant with the Larmor frequency ω_0, is applied along the x-axis during an NMR experiment. This radio frequency (RF) field originates from a coil wound around the sample in the xy-plane, which is also used to detect the precessing magnetization during NMR experiments. The magnetization induces a current in the coil which can be converted to a so-called free induction decay (FID) signal.[72]

In the stationary (laboratory) frame of reference, $\boldsymbol{B_1}$ consists of two components, that rotate around $\boldsymbol{B_0}$ with $\pm\omega_{rf}$ (= frequency of the RF-pulse). To be able to interact, it must rotate in the same direction, which only applies for one component, called $\boldsymbol{B_1}$(t). If we now switch to a rotating frame of reference, that rotates around the z-axis with ω_{rf}, its time-dependence can be eliminated and $\boldsymbol{B_1}$ seems to be static.[71] In the rotating frame of reference, $\boldsymbol{B_0}$ diminishes to a reduced field $\Delta\boldsymbol{B}$:

$$\Delta\boldsymbol{B} = -\frac{\omega_0 - \omega_{\mathrm{rf}}}{\gamma}. \tag{2.60}$$

Therefore, the much smaller RF-field $\boldsymbol{B_1}$ can influence the precessing magnetization. The reduced field and the static field $\boldsymbol{B_1}$ result in an effective field $\boldsymbol{B_{eff}}$ (see Figure 18)[72]:

$$\mathbf{B}_{\boldsymbol{eff}} = \sqrt{\boldsymbol{B_1^2} + (\Delta\boldsymbol{B})^2}\,. \tag{2.61}$$

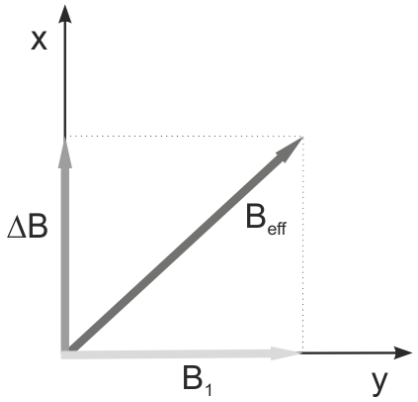

Figure 18: Effective magnetic field B_{eff}[72]

The magnetization now precesses around this field $\boldsymbol{B_{eff}}$.[72] During one pulse length τ_{rf}, $\boldsymbol{B_1}$ can change the angle of the nuclear magnetization (precessing with ω_1) by the so-called *flip angle* θ_{rf} [71]:

$$\theta_{\mathrm{rf}} = \omega_1\,\tau_{\mathrm{rf}} = \gamma\,\boldsymbol{B_1}\,\tau_{\mathrm{rf}}\,. \tag{2.62}$$

If ω_{rf} equals the Larmor frequency, the RF-pulse is “on-resonance”. In this case a 90 ° (π/2) RF-pulse along the x-axis of the rotating coordinate system leads to a tilt

of the precessing magnetization around the negative y-axis (M_z = 0). By varying the pulse length, the flip angle can be changed. Therefore, a 180 ° (π) RF-pulse results in an inversion of the magnetization around the negative z-axis.[71,72]

2.4.2.3 The Phenomenon of Relaxation

As already mentioned before, relaxation is the process of individual spins reaching an equilibrium state again, after a RF-pulse changed the occupancy of the energy levels. At the equilibrium state, the magnetization aligns with the external magnetic field $\boldsymbol{B_0}$ along the z-axis and therefore, can be written as follows: $M_z = M_0$ and $M_x = M_y = 0$.[74]

After a RF-pulse at the resonance frequency was applied to a sample, the time-dependent motion of the magnetization vector can be described by the *Bloch equations* in the rotating frame[70]:

$$\frac{d\boldsymbol{M_z}}{dt} = -\frac{\boldsymbol{M_z} - \boldsymbol{M_0}}{T_1}, \tag{2.63}$$

$$\frac{d\boldsymbol{M_x}}{dt} = -\frac{\boldsymbol{M_x}}{T_2} \quad and \quad \frac{d\boldsymbol{M_y}}{dt} = -\frac{\boldsymbol{M_y}}{T_2}, \tag{2.64}$$

where T_1 is the longitudinal or spin-lattice relaxation (SLR) time and T_2 is the transversal or spin-spin relaxation time. For the longitudinal relaxation, the absorbed energy of the RF-pulse is transferred to the lattice. The magnetization ($\boldsymbol{M_z}$(t) = 0 at t = 0) regrows along the z-axis after the RF-pulse according to[70,74]:

$$\boldsymbol{M_z}(t) = \boldsymbol{M_0}\left[1 - \exp\left(\frac{-t}{T_1}\right)\right]. \tag{2.65}$$

This also results in a change in energy. In contrast to this, the energy remains unchanged during transversal relaxation. For the transversal relaxation, the nuclear magnetic moments lose their phase coherence due to a difference in the effective magnetic field for nuclei at different positions. This is because the external magnetic field $\boldsymbol{B_0}$ is not fully homogenous. This yields deviations of the Larmor frequencies of chemically equivalent nuclei. Because $\boldsymbol{M_z}$ cannot regrow fully to $\boldsymbol{M_0}$ before the transverse magnetization vanishes, the following must apply: $T_1 \geq T_2$.[70]

Additionally, one can measure $T_{1\rho}$, the spin-lattice relaxation time constant in the rotating frame. It can provide insight into slow molecular dynamics (because $T_{1\rho} < T_1$). It can be derived via a spin-locking experiment, where a π/2 RF-pulse is applied, leading to a precession of the magnetization in the x-y plane. To lock the magnetization, a locking field $\boldsymbol{B_1}$ is used. After a certain time, this locking field $\boldsymbol{B_1}$ is turned off and the transverse magnetization decays to zero in an exponential order.[51,69] In figure 19 measurement techniques to derive T_1 and $T_{1\rho}$ are shown.

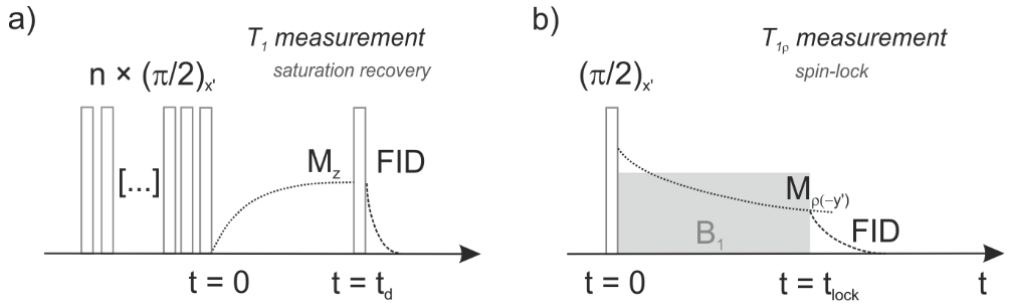

Figure 19: Techniques to measure T_1 and $T_{1\rho}$ **a)** "saturation recovery experiment"; several π/2-pulses are applied to destroy longitudinal magnetization, followed by a π/2-pulse after a time t_d to measure its recovery **b)** "spin-locking"; initial π/2-pulse followed by locking of $M_{-y'}$ via a small field B_1. Now the decay of the magnetization can be related to the locking pulse length t_{lock}.[75,76]

2.4.2.4 Data analysis

For uncorrelated, isotropic 3D diffusion processes, a model by Bloembergen, Purcell and Pound[77] ("*BPP-model*") can be used for data analysis of spin-lattice relaxation NMR spectroscopy with the correlation function *G*(t)[76]:

$$G(t) = G(0)e^{\left(-\frac{|t|}{\tau_c}\right)}, \tag{2.66}$$

with τ_c^{-1} as the correlation rate, which is related to the time between two jumps of a species[75]:

$$\tau_c^{-1} = \tau_{c,0}^{-1}\exp^{\left(-\frac{E_a}{k_B T}\right)}. \tag{2.67}$$

The Fourier transformation of the correlation function leads to the Lorentzian shaped spectral density function $J(\omega_0)$[76]:

$$\frac{1}{T_1} \equiv R_1 \propto J(\omega_0) \approx G(0)\frac{2\tau_c}{1+(\omega_0\tau_c)^2}. \tag{2.68}$$

This spectral density function $J(\omega_0)$ is directly proportional to the spin-lattice relaxation rate R_1. As the *BPP model* is only valid for uncorrelated processes, correlated diffusion needs an adaption for the single exponential correlation function. This can be accomplished by introducing a stretched exponential with the stretching component α leading to a spectral density function as follows[75]:

$$J(\omega_0) = G(0)\frac{2\tau_c}{1+(\omega_0\tau_c)^{1+\alpha}}. \tag{2.69}$$

The values for α can vary from 0 to 1 (α = 1 for uncorrelated motion). The reason for correlated diffusion processes and therefore, the need for an adaption of the *BPP model*, can be coulombic spin-spin interactions, vacancy diffusion or structural disorder in the material of interest. By looking at Figure 20, one can see that correlated processes only affect the low-temperature flank.[75] In Figure 20 the typical graphical data representation for relaxation rates, namely an Arrhenius diagram, shows the temperature dependencies by plotting the logarithm of the relaxation rate versus the inverse temperature.

At the diffusion-induced rate peak the condition $\omega_0\tau \approx 1$ is valid. From this maximum condition the jump rate τ^{-1} ($\approx \tau_c^{-1}$) can be deduced and used to determine the microscopic self-diffusion coefficient:

$$D_{\mathrm{NMR}} = \frac{a^2}{6\tau}, \tag{2.70}$$

where a is the average jump length. Via the correlation factor f the self-diffusion coefficient can be linked to the tracer diffusion coefficient ($D^* = f\,D_{\mathrm{NMR}}$) and therefore be compared with the diffusion coefficient of AC impedance spectroscopy measurements.[76]

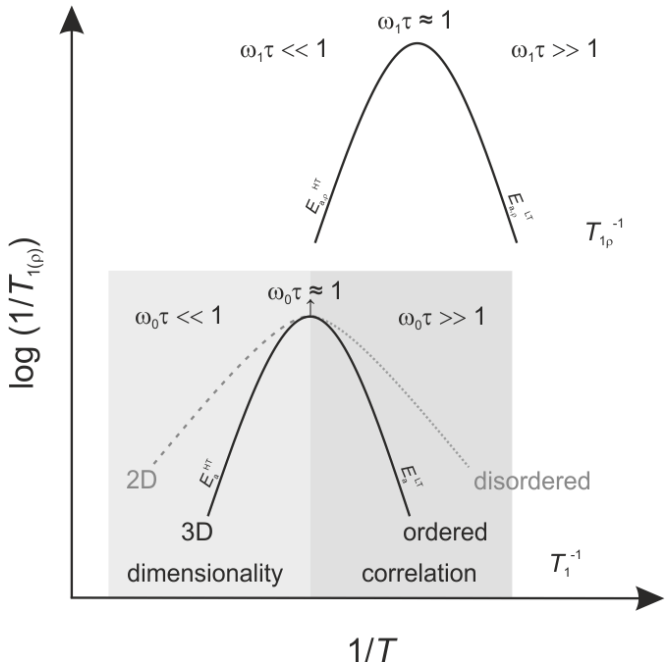

Figure 20: Arrhenius diagram showing the spin-lattice relaxation rates of T_1 and $T_{1\rho}$. The BPP model describes the rate peak of uncorrelated 3D diffusion processes (solid line). Dimensionality is reflected on the high temperature flank and correlation effects are shown on the low temperature flank. From the peak maximum the jump rate τ^{-1} can be derived via $\omega_0\tau \approx 1$. The $T_{1\rho}$ relaxation rate peak is shifted towards lower temperatures. For $T_{1\rho}$ the same effects of dimensionality and correlation as for T_1 can be seen if present.[61,78]

Uncorrelated 3D diffusion processes described by the *BPP model* show symmetric rate peaks (see Figure 20). From the slopes of the flanks the activation energy E_a can be derived. In general, lower dimensional diffusion leads to lower slopes in the high temperature regime ($\omega_0\tau_c \ll 1$), which is dependent on the Larmor frequency ω_0.[75,78] An example for a lower dimensional diffusion process is the 2D diffusion in layer structured materials like hectorites. This type of material was also analyzed in the course of this thesis. In the case of 3D diffusion, which shows steeper slopes, long-range ion transport properties can be investigated in this high temperature regime. Local hopping and correlation effects are reflected in the low temperature regime ($\omega_0\tau_c \gg 1$) of the SLR rates. Additionally, SLR rates in the rotating frame ($T_{1\rho}^{-1}$) can be measured by utilizing much lower effective frequencies (ω_1). Here, the diffusion-induced rate peak is shifted towards lower temperatures.[78]

2.4.2.5 Magic-Angle Spinning - NMR

In order to analyze structural properties, solid samples can deliver NMR spectra, that are similar to liquid ones, via the *magic-angle spinning* (MAS) technique. NMR spectra of solids are usually very broad, missing a resolved structure. This is caused by the random orientation of the crystallites in powder samples. These issues originate from chemical shift anisotropy, dipolar and quadrupolar coupling of solid matter, which are all anisotropic. Whereas in liquid samples, the fast motions of the individual molecules can eliminate those troublesome phenomena, for solid ones, we must make use of the so-called magic angle. This angle ϑ_R, that must be spanned between the sample´s rotation axis and the external magnetic field $\boldsymbol{B_0}$, equates to 54,74 ° (see Figure 21). If a sample is spun at a high frequency at this specific angle, an averaging effect can be achieved, and sharp signals can be obtained. Spinning with too low frequencies leads to spinning sidebands next to the isotropic chemical shift. To differentiate between those sidebands and the isotropic chemical shift, one can make use of the dependence of the position of the sidebands on the spinning rate.[70,71]

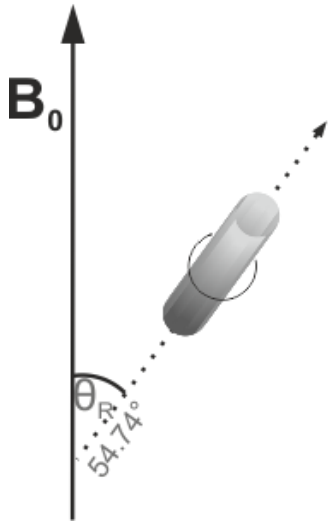

Figure 21: Magic angle spinning experiment. The sample rotates at an angle of 54.74° between its rotation axis and the external magnetic field $\boldsymbol{B_0}$.[71]

2.4.3 X-Ray Diffraction

2.4.3.1 Introduction

X-ray diffraction is a well-known, commonly used crystallographic characterization method. It is the method of choice for crystal structure determination.[79] In general, the wavelengths of x-rays vary between 0.1 and 100 Å. Those wavelengths used for crystallographic characterization lie between 0.5 and 2.5 Å, which matches interatomic distances. Monochromatic x-rays with a wavelength in the order of the distance between different lattice planes, lead to interference phenomena when hitting a crystal lattice. If a beam of x-rays is focused on a material, there are three possible processes that can be observed: coherent scattering, incoherent scattering, and absorption. Only the first one is important for x-ray diffraction measurements.[80]

The generation of x-rays usually takes place in high-vacuum tubes (see Figure 22). Generation via a synchrotron is neglected here. A high voltage is applied leading to the generation of electrons by a cathode (W-filament). The electrons are focused at an anodic metal target (Mo or Cu). The target is permanently cooled because of heat development during the deceleration of the electrons. The applied voltage ranges between 30 and 60 kV.[80,81] Usually, molybdenum anodes are used for single crystal experiments and copper ones in powder diffractometry. There are two classes – sealed and rotating anode tubes. The rotating anode tubes show increased thermal efficiency, and therefore beam brightness, in contrast to the sealed tube.[80]

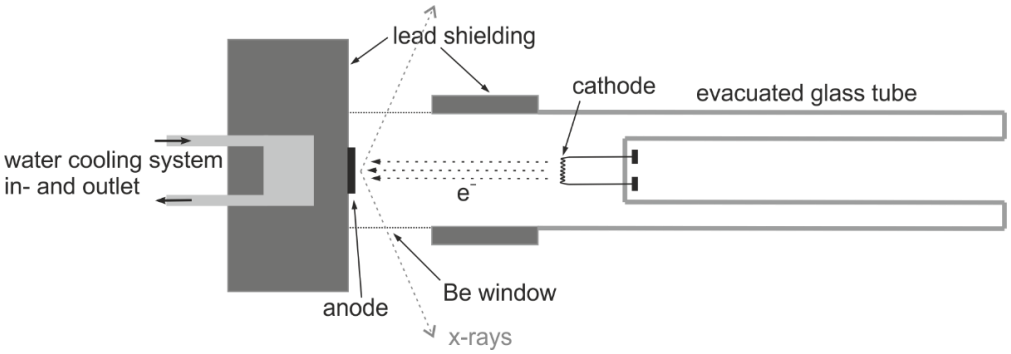

Figure 22: X-ray tube usually consisting of an evacuated glass tube, an anode and cathode material, some shielding as well as beryllium windows as x-ray outlets. Additionally, a cooling system is required.[81,82]

A x-ray spectrum is composed of a continuous “white radiation” (also called “bremsstrahlung”) and characteristic spectral lines. The bremsstrahlung originates from decelerating electrons.[80] The characteristic radiation is obtained by the emission of x-ray photons by electrons falling from higher L-shells into K-shell-vacancies. In this case, a doublet, called $K_{\alpha1}$ and $K_{\alpha2}$ is observed. In the same way a higher energy doublet $K_{\beta1}$/ $K_{\beta2}$ is formed by electrons transitioning from the M- to the K-shell.[81] As a result of energy differences between the levels, which vary depending on the element used, the distribution of wavelengths is characteristic.[80] The generated x-rays leave the tube via Be windows since they are permeable in the

relevant wavelength range. There is a set of four windows, two of each are either responsible for a point-focused beam, used for single-crystals, or for a line-focused beam, used for powder diffraction.[81]

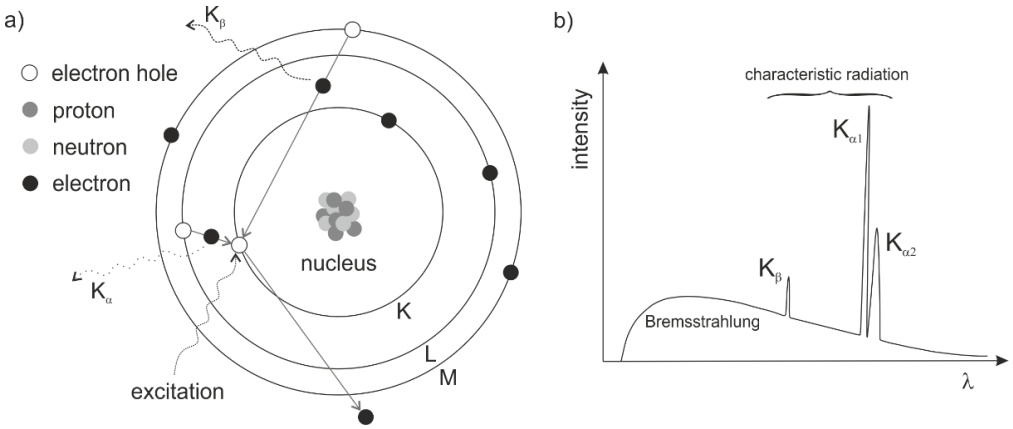

Figure 23: a) Schematic representation of an atom and its electron shells. Depending on the shells involved, one can differentiate between K_α and K_β radiation.[82] **b)** Simplified x-ray spectrum with the intensity plotted versus the wavelength λ; Bremsstrahlung and characteristic radiation[83]

As the x-ray beam obtained is polychromatic and would therefore lead to a high background and broad and asymmetric peaks, collimation and monochromatization are crucial. Collimation describes the selection of wavelengths with more or less parallel propagation vectors and can be performed by using slits. For monochromatization of the radiation we need to eliminate K_β radiation. The easiest way to do this is to use the absorption properties of β-filters.[80] To eliminate K_β radiation, a metal filter having an ionization energy of its K-shell slightly below that of K_β is needed. Another option is using a single-crystal monochromator, where only the K_α radiation leads to constructive interference.[81] Both methods, collimation and monochromatization, cause intensity losses. For the detection, a variety of devices is available. Their mechanisms are based on different effects, that occur upon contact with x-rays (incoming photons). It can be distinguished between area (e.g. charge coupled devices or image plates) and point detectors (e.g. gas proportional counters or solid-state detectors).[80]

Different structure factors enable the determination of the lattice structure via the measurement of reflection intensities. Scattering of x-rays takes place at the electron shell of an atom and solely those atoms lying on the lattice planes lead to in-phase scattered radiation. Because a radial dependence of the electron density exists and the atoms must not exactly lie in the lattice planes, those divergences in electron density yield in phase shifts. An *atom formfactor f*, which is a ϑ-dependent scattering amplitude, can take these deviations into account. Furthermore, the a*tom displacement factor* or "temperature factor" (because it increases with temperature) takes the thermal motion of the atoms around their mean position in the crystal lattice into account.[81]

2.4.3.2 Laue Equations and Miller Indices

X-rays are reflected by certain crystallographic planes. The so-called *Laue equations* describe the correlation between incident and diffracted beams. They are used for the representation of the diffraction geometry of single crystals[80]:

$$a(cos\psi_1 - cos\varphi_1) = h\lambda\,, \tag{2.71}$$

$$b(cos\psi_2 - cos\varphi_2) = k\lambda\,, \tag{2.72}$$

$$c(cos\psi_3 - cos\varphi_3) = l\lambda\,, \tag{2.73}$$

with the unit cell parameters, *a*, *b* and *c*, the incident and diffracted beam angles ψ_{1-3} and φ_{1-3} as well as the irradiation wavelength λ. All three must be concurrently satisfied in order to obtain sharp peaks in the diffractogram. The integer indices *h*, *k* and *l* are called *Miller indices* and define the position of the peaks in the reciprocal lattice. Crystallographic planes with identical *Miller indices* are parallel to each other and are separated by the same distance d_{hkl}.[80] *Miller indices* are used to describe the orientation of the lattice planes regarding the crystal lattice. In order to identify the *hkl* indices, the plane of a stack, that is located closest to the origin, is chosen. The intercepts of this plane with the unit cell axis are related to the indices as follows[81]:

$$h = \frac{1}{a}\quad,\quad k = \frac{1}{b}\quad,\quad l = \frac{1}{c}\,. \tag{2.74}$$

The *Miller indices* are written in parentheses (*hkl*) to denote a face or set of planes and without them, *hkl*, if one wants to refer to the reflection from these planes.[81]

2.4.3.3 Bragg´s Law

According to *Bragg´s law*, x-rays must be reflected from the lattice planes at the same angle θ as they hit the planes.[80] The path difference Δ after the reflection at the lattice planes accounts for $\Delta = 2d_{hkl}sin\vartheta$ with d_{hkl} as the spacing between the planes. Constructive interference can only take place if this difference is an integer *n* of the wavelength λ of the incident x-rays (see Figure 24 for visualization). *Bragg´s law* can be written as follows[80]:

$$2d_{hkl}sin\theta_{hkl} = n\lambda\,. \tag{2.75}$$

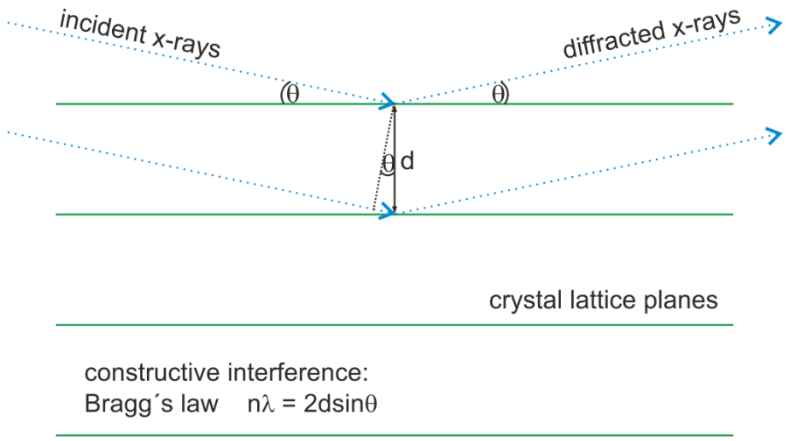

Figure 24: Crystal lattice plane with spacing *d* and angle of incidence/diffraction ϑ; Bragg´s law of constructive interference.[82]

2.4.3.4 Powder Diffraction: Debye-Scherrer Method

X-ray diffraction measurements of powder samples can be performed via the *Debye-Scherrer method*. The crystallites of powders are statistically distributed over the whole sample volume. Several crystallites amongst them will offer an arrangement of lattice planes (hkl) suitable for constructive interference with the incoming beam of x-rays. The lattice planes are tangent to a cone with an angle of aperture of 2ϑ and the reflected radiation is tangent to a cone with 4ϑ. A cylindrical camera is used for detection. The powder sample is placed in the cylinder axis. In the past, a photographic film was used to record the measurements. The cones of reflection caused so-called *Debye-Scherrer lines* on the film. Today the detection is done electronically. Via the Bragg equation one can determine the distance d_{hkl} between the lattice planes and assign those (hkl) responsible for the reflections. For a simple cubic crystal system (a = b = c) the following equation applies:

$$d_{hkl} = \frac{a}{\sqrt{h^2 + k^2 + l^2}}. \tag{2.76}$$

Using the *Bragg´s law* this leads to:

$$sin^2\theta = \frac{\lambda^2}{4a^2}(h^2 + k^2 + l^2)\,. \tag{2.77}$$

Because every type of crystal shows a characteristic diffraction pattern, powder diffraction is used for their identification. With the help of databases containing information of crystallographic data, a clear assignment is possible.[84]

Rietveld Refinement

The *Rietveld method* can be used for qualitative and quantitative crystal structure analysis.[83] For the refinement of a diffraction diagram, a structure model is needed.[83] Occupancies, model and thermal parameters, as well as atomic coordinates are fitted using the least-squares method, relying on a x-ray diffraction sample database.[79] The *Rietveld refinement* is especially useful if the investigated sample is isostructural with a material that has already been analyzed by single crystal x-ray diffraction. If x-ray diffraction is performed on a crystalline powder no information can be obtained from the spatial distribution of the reflections. This leads to difficulties regarding the assignment of the reflections (= indexing) as only the scattering angle is known.[81]

2.4.3.5 Single Crystal X-Ray Diffraction

Different techniques can be employed to analyze single crystals using x-rays. Two of them are the *Laue* and the *Oscillation method*. The *Laue method* uses continuous radiation and a stationary single crystal, which only lets through the appropriate wavelength for the reflections in terms of the *Bragg´s law*. The Laue method uses a photograph showing diffraction spots located on ellipses. For this type of technique, the crystal position is crucial for successful analysis. Another important technique is the *flat-plate oscillation* technique. This technique can be performed for a preliminary examination to check if a crystal is suitable for an x-ray diffraction experiment. In contrast to the former method, the single crystal is in movement. The detection is carried out using area detectors.[79]

3 Results

3.1 Understanding the Origin of Enhanced Li-Ion Transport in Nanocrystalline Argyrodite-Type Li_6PS_5I

Since the discovery of synthetic lithium containing argyrodite materials with the general formula Li_6PS_5X (X= Cl, Br, I) for the use as solid electrolytes, they have been studied extensively.[41,42,44,46,47] Among these halide argyrodites, only the bromide and chloride compounds reach ionic conductivities sufficiently high (in the mS cm^{-1} range) to be considered as candidates for lithium ionic conductors in batteries. The iodine analogue on the contrary, shows a high degree of structural order and only local lithium ion mobility. Therefore, it does not offer such high ionic conductivities.[85] The lack of the anion site disorder present in the iodine and bromide compound, impedes long-range lithium ion transport. In the following publication an approach to improve the ionic conductivity of Li_6PS_5I is shown. Anionic site disorder is introduced via high-energy mechanical ball milling. Changes in ionic conductivity and structure were investigated via broadband conductivity spectroscopy and ^{7}Li NMR, ^{6}Li and ^{31}P MAS NMR as well as x-ray powder diffraction. The experiments showed differences between the pristine sample and the one that was treated by a soft-mechanical approach verifying the prior assumptions. In pristine Li_6PS_5I intercage jumping processes of Li^+ are restricted.[43] After milling, charge carrier mobility and concentration increased. The DC conductivity improved from around 1 µS cm^{-1} to 0.2 mS cm^{-1} at ambient conditions. ^{31}P MAS NMR revealed, that the entire nanocrystalline material is affected by ball milling - not only its surface. Those findings demonstrate that the performance of ionic conductors can be greatly improved via a soft-mechanical treatment, which introduces disorder into the structure.

Understanding the Origin of Enhanced Li-Ion Transport in Nanocrystalline Argyrodite-Type Li_6PS_5I

M. Brinek, C. Hiebl, and H. M. R. Wilkening

Chemistry of Materials **2020** *32* (11), 4754-4766

CHEMISTRY OF MATERIALS

pubs.acs.org/cm

Article

Understanding the Origin of Enhanced Li-Ion Transport in Nanocrystalline Argyrodite-Type Li_6PS_5I

Marina Brinek,[†] Caroline Hiebl,[†] and H. Martin R. Wilkening*

Cite This: https://dx.doi.org/10.1021/acs.chemmater.0c01367

Read Online

ACCESS | Metrics & More | Article Recommendations

ABSTRACT: Argyrodite-type Li_6PS_5X (X = Cl, Br) compounds are considered to act as powerful ionic conductors in next-generation all-solid-state lithium batteries. In contrast to Li_6PS_5Br and Li_6PS_5Cl compounds showing ionic conductivities on the order of several mS cm^{-1}, the iodine compound Li_6PS_5I turned out to be a poor ionic conductor. This difference has been explained by anion site disorder in Li_6PS_5Br and Li_6PS_5Cl leading to facile through-going, that is, long-range ion transport. In the structurally ordered compound, Li_6PS_5I, long-range ion transport is, however, interrupted because the important intercage Li jump-diffusion pathway, enabling the ions to diffuse over long distances, is characterized by higher activation energy than that in the sibling compounds. Here, we introduced structural disorder in the iodide by soft mechanical treatment and took advantage of a high-energy planetary mill to prepare nanocrystalline Li_6PS_5I. A milling time of only 120 min turned out to be sufficient to boost ionic conductivity by 2 orders of magnitude, reaching $\sigma_{total} = 0.5 \times 10^{-3}$ S cm^{-1}. We followed this noticeable increase in ionic conductivity by broad-band conductivity spectroscopy and ^{7}Li nuclear magnetic relaxation. X-ray powder diffraction and high-resolution ^{6}Li, ^{31}P MAS NMR helped characterize structural changes and the extent of disorder introduced. Changes in attempt frequency, activation entropy, and charge carrier concentration seem to be responsible for this increase.

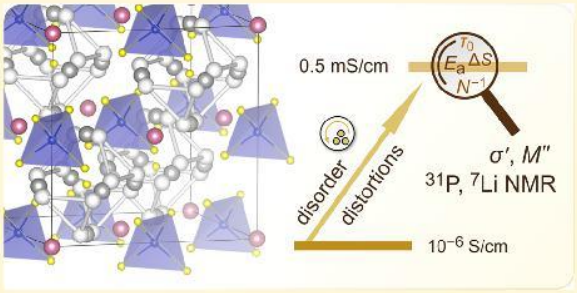

1. INTRODUCTION

Reducing human greenhouse gas emissions to lessen the increase of global temperature is one of the biggest challenges that industrial societies are facing. The development of highly efficient, but at the same time sustainable, electrochemical devices to store electricity generated from renewable "sources" is, thus, of primary importance in materials science and engineering.[1,2] This goal is expected to be achieved with the design of lithium all-solid-state batteries[3−5] with metallic Li as the anode material.[6−8] However, many hurdles, particularly related to interfaces[9−11] and (electro-)chemical stabilities,[12−16] have to be overcome to present market-ready solutions.

A key component in such systems is the solid electrolyte.[7,17−22] Suitable electrolytes should show ionic conductivities[23,24] comparable to those of aprotic liquid blends ordinarily used in lithium-ion batteries. Over the last decade, various oxides,[17] hydrides,[25] phosphates,[18,26] and thiophosphates,[23,27,28] including especially Li_3PS_4,[29] $Li_7P_3S_{11}$ as glass ceramics,[30−34] and argyrodite-type Li_6PS_5X (X = Cl, Br),[35−46] were extensively studied with regard to their applicability as ceramic electrolytes. Li_6PS_5I was first introduced by Deiseroth and co-workers;[47,48] the authors studied the structural details, ionic conductivity, and diffusion pathways in a sample prepared by a solid-state synthesis route. Later, mechanosynthesis was used to prepare Li_6PS_5I with a high ionic conductivity by Tarascon and co-workers[45] as well as by Rao and Adams.[49] It is also well known that ionic conductivities in glassy Li_2S-P_2S_5, Li_2S-P_2S_5-LiI glasses and glass ceramics show very high ionic conductivities.[50−54] As an example, also high conductivities in $Li_7P_2S_8I$-type compounds were reported.[55,56] Focusing, however, on highly crystalline argyrodite-type Li_6PS_5X, it turned out that under ambient conditions only Li_6PS_5Br and Li_6PS_5Cl,[35,57] and some variants,[41] including also compounds with higher contents of X,[58−61] are able to deliver ionic conductivities in the desired range of a few mS cm^{-1}.[46,62] Thus, also battery applications and electrochemical testing mainly concentrate on these compounds,[63] including glassy Li_2S-P_2S_5-LiI and glass ceramics, as mentioned above.[51] Importantly, S^{2-}/X anion site disorder, also introduced via substitution[41,64−66] or kinetic freezing,[43] ensures that the Li^+ ions can quickly jump from site to site within the complex crystal structure (see Figure 1). In Li_6PS_5X (X = Cl, Br), Li^+ is

Received: March 31, 2020
Revised: May 18, 2020
Published: May 19, 2020

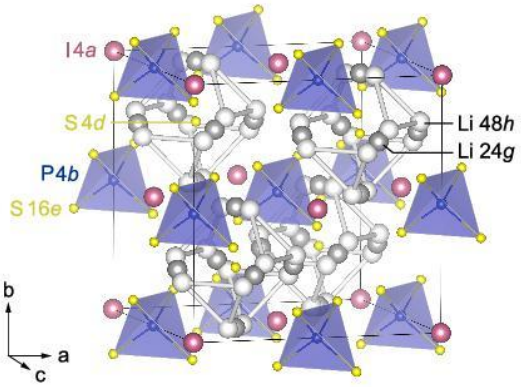

Figure 1. Crystal structure of face-centered cubic Li_6PS_5X with X = I. Iodine anions occupy the 4a sites. Sulfur anions reside on the 4d and 16e sites. Together with P^{3+} on 4b, the latter form PS_4^{3-} tetrahedra. Li ions are arranged such that they build cages consisting of six 48h−24g−48h' triplets. In general, the Li sites are only partially occupied; strong repulsive Coulomb interactions are expected for Li ions on neighboring sites 24g and 48h. Intracage jumps include hopping processes between 48h sites of two different triplets. The pathway 48h−24g−48h′ allows the Li ions to perform spatially highly restricted translational movements, which are expected to leave a characteristic fingerprint in conductivity isotherms. Long-range ion dynamics is possible either directly when jumping from cage to cage ($48h_1$-$48h_2$) or using the interstitial sites connecting the Li cages, as suggested by Deiseroth and co-workers (see below).[47]

subjected to facile exchange processes within and between the Li cages formed by the Li positions 48h and 24g. Such a cage is built by six 24g−48h−24g triplets, which are arranged such that intercage hopping processes can also occur.[67] Indeed, as shown by broad-band conductivity spectroscopy, the cages are connected by fast diffusion pathways in the case of X = Cl and X = Br.[46] For these two compounds, anion site disorder is seen, i.e., S^{2-} and X^- share positions 4d and 4a (Figure 1).[42]

For Li_6PS_5I, on the other hand, this anion site disorder is, however, absent.[42,46] The iodine anions solely occupy the 4a positions (Figure 1).[42] The sites 4d inside the cages are exclusively populated by the sulfur anions that also occupy the 16e sites forming the PS_4^{3-} tetrahedra (see also Figure 1). In contrast to anion-disordered Li_6PS_5X (X = Cl, Br), for the ordered counterpart with X = I, the important intercage diffusion step, being necessary to enable long-range ion transport rather than only local jump processes, is characterized by noticeably higher activation energy (see below).[46,67] Hence, despite its larger lattice constant and the presence of easily polarizable iodide anions, for the structurally ordered and unsubstituted iodine compound Li_6PS_5I, through-going Li^+ transport is rather poor.[46] The absence of a percolating network of fast diffusion pathways for Li_6PS_5I results in room-temperature ion conductivities σ with values as low as 1×10^{-6} S cm^{-1} associated with an activation energy E_a as high as 0.47 eV.[46] For comparison, for Li_6PS_5Cl, a value of $\sigma = 3.8 \times 10^{-3}$ S cm^{-1} has been reported.[46] In line with this increase in σ, the corresponding activation energies for X = Cl, Br are considerably lower and range from 0.25 to 0.4 eV, depending on the method applied to study ion dynamics.[46]

If structural disorder plays a major role in boosting the ionic conductivity of this class of thiophosphates, the successful conversion of structurally ordered Li_6PS_5I into a nanocrystalline, structurally disordered counterpart should result in a significant increase of σ. Here, we synthesized highly crystalline, i.e., well-ordered, Li_6PS_5I by a solid-state reaction with a sufficiently long sintering period. Afterward, we gently treated the material under an inert (Ar) gas atmosphere in a high-energy ball mill. Broad-band conductivity spectroscopy[68] revealed, indeed, an increase of ionic conductivity by a factor of 100. X-ray powder diffraction, ^{7}Li NMR relaxometry,[69] and high-resolution (magic angle spinning, MAS) ^{6}Li and ^{31}P NMR helped us to further characterize the microstructure of the nanocrystalline sample. Our investigation represents another application-oriented example where high-energy ball-milling was successfully applied to boost ion dynamics of an originally poor ionic conductor without changing its overall chemical composition. While for previous oxide examples[70−73] the final conductivities showed values in the μS range, mechanical treatment of Li_6PS_5I ensured that conductivities with values almost touching the mS regime were reached.

2. EXPERIMENTAL SECTION

The preparation of Li_6PS_5I is described elsewhere.[46] For the present study, we used the powder of the same synthesis batch, which was recently investigated[46] also by impedance measurements and NMR spectroscopy. To prepare nanocrystalline Li_6PS_5I, 0.5 g of the microcrystalline powder was filled in ZrO_2 milling vials (45 mL) inside an Ar-filled glovebox (H_2O < 1 ppm, O_2 < 1 ppm). The milling jars were filled with 60 milling balls (5 mm in diameter, ZrO_2). To prepare nanocrystalline Li_6PS_5I, we used a Premium line 7 planetary mill (Fritsch), which was operated at a rotation speed of 400 rpm. The milling time was set to 120 min. Compared to other ball-milling strategies,[74] these conditions represent a rather soft approach. Afterward, the powder was transferred back to the glovebox and pressed uniaxially (0.5 tons) into pellets with a diameter of 5 mm and thicknesses of 0.93 mm (micro-Li_6PS_5I) and 1.17 mm (nano-Li_6PS_5I), respectively. For NMR measurements, see below, the powder was sealed in Duran ampoules.

X-ray powder diffraction was carried out with a Bruker D8 Advance diffractometer (Bragg Brentano geometry, Cu Kα radiation). Patterns were recorded with a step size of 0.02° (measuring time 2 s) in the 2θ-range 10−100°. The acquisition of one-pulse ^{6}Li and ^{31}P MAS NMR spectra (25 kHz spinning speed, 2.5-mm rotors) with a Bruker 500-MHz NMR spectrometer is identical to the procedure described elsewhere.[46] The same holds for the measurement of variable-temperature ^{7}Li NMR spin-lattice relaxation rates in both the laboratory ($1/T_1$) and rotating frames of reference ($1/T_{1\rho}$), which was carried out with a Bruker 300-MHz NMR spectrometer. We refer to a recently published study that describes the spectrometer settings in detail.[46]

To measure the impedance responses of the pellets, we coated the pellets of nanocrystalline Li_6PS_5I with a thin Au layer (100 nm) using a Leica EM SCD 050 sputter coater. Impedance spectra were recorded with a Novocontrol Concept 80 broad-band dielectric spectrometer; we varied the frequency from ν = 10 mHz to 10 MHz and measured complex conductivities over a relatively large temperature range, viz. from T = 173 to 433 K in steps of 20 K. The temperature in the sample holder was controlled with a Quatro Cryosystem (Novocontrol) that uses freshly evaporated nitrogen and a heater to adjust the temperature with an accuracy of ±0.5 K. The measurements were carried out in a dry nitrogen atmosphere to avoid any contaminations with water and oxygen. In addition, for some measurement runs, we used an airtight, home-built sample holder, which was placed in the ZGS active cell of the Novocontrol spectrometer. The pellet was inserted into the sample holder in an Ar-filled glovebox to further eliminate any possible contact with the surrounding air.

https://dx.doi.org/10.1021/acs.chemmater.0c01367
Chem. Mater. XXXX, XXX, XXX−XXX

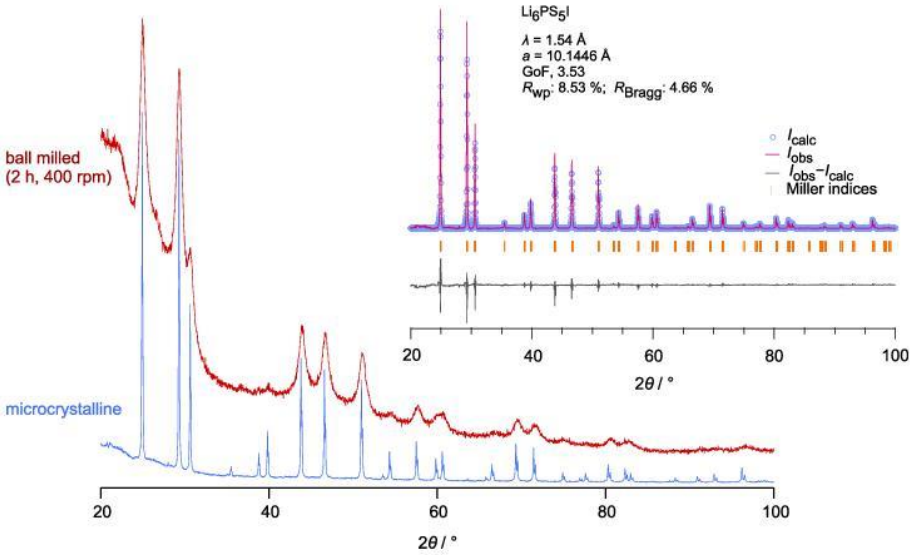

Figure 2. X-ray powder diffraction pattern of nanocrystalline Li_6PS_5I that was milled for 2 h in a planetary high-energy ball mill (400 rpm). Broad humps arise from the mercapto foil used to protect the material from moisture during the measurements. Partly, these humps overlap with those originating from some amorphous material produced by milling. In addition, significant broadening of the reflections points to a heavily disordered, nanocrystalline material. For comparison, the powder pattern of the starting material, named microcrystalline Li_6PS_5I, is shown at the bottom. The inset presents a background-correct version of the same pattern that has been analyzed with the method introduced by Rietveld. The latter was taken from a recently published study on ion dynamics in microcrystalline Li_6PS_5I.[46] It shows a phase-pure material with negligible amounts of impurities, e.g., LiI. See ref 46 for the abbreviations used.

3. RESULTS AND DISCUSSION

Pure Li_6PS_5I was prepared in a polycrystalline form with the help of a solid-state reaction.[46] In the inset of Figure 2, the background-corrected X-ray powder diffraction is shown together with the results from Rietveld refinement; data were taken from an earlier investigation published by some of us.[46] High-energy ball-milling of polycrystalline Li_6PS_5I under the conditions described above results in a drastic broadening of the reflections; see Figure 2. Most importantly, no further reflections of any decomposition products emerge. Li_6PS_5I remains stable under the milling conditions chosen; we do not observe any chemical degradation when milling the compound under an inert gas atmosphere. This view is supported by ^{6}Li MAS and ^{31}P MAS NMR; see below. In addition, the amount of abraded material also seems to be negligible; no reflections of abraded nano-ZrO_2 appear. Chemical analysis does not even reveal traces of Zr. For comparison, the noncorrected X-ray powder diffraction pattern of the coarse-grained starting material is also shown in Figure 2.

Strong broadening of the reflections shows that the mean crystallite size d_m was reduced from the μm range down to the nm regime.[75] Indeed, via the equation introduced by Scherrer,[76] we estimated that after the milling step d_m is given by approximately 15 nm. We anticipate that cluster-assembled agglomerates of smaller and larger crystallites exist, possibly embedded in an amorphous matrix. Indeed, an estimation yields that the X-ray powder diffractogram points to 10−15% of amorphous material. According to previous studies on nanocrystalline $LiNbO_3$ and $LiTaO_3$,[70,73] a high-energy ball is in general expected to generate amorphous material.[77] In the case of fluorides,[78−80] such as BaF_2 or $BaLiF_3$, this amount does, however, not dominate the overall morphology of the material. On the other hand, a powder consisting of nm-sized crystallites has a large volume fraction of interfacial regions,[77,81−86] which, in many cases, are assumed to be in a structurally disordered state, leading to a core−shell structure.[85] Ions residing in these surface-related areas are expected to have access to faster diffusion pathways than the ions located in the ordered bulk regions. This observation, which resembles that of a core−shell structure with distinct ion dynamics of the two regions, has been verified for several classes of nanocrystalline ceramics, such as single-phase (Li_2O,[87] Li_2O_2,[88] and $LiBH_4$[86]) and two-phase systems ($LiF:Al_2O_3$,[89] $Li_2O:X_2O_3$ (X = B, Al)).[84,87,90,91]

Apart from such surface-related effects, also space-charge zones might be responsible for fast ion transport in nanostructured solids.[92−96] The most prominent examples are epitaxially grown alternating layers of BaF_2 and CaF_2.[97] Facile fluorine conduction was not only observed along the interfaces between the two fluorides but also across as space-charge zones overlap if the individual thickness of the fluoride layers reaches the nm regime.[97] Despite such nontrivial size effects, nanocrystalline materials produced by high-energy ball-milling will also have a large number of defects introduced in the bulk regions.[73,77] For Li_6PS_5I, we expect that, besides the effect of interfacial regions, defect-rich bulk regions of the nm-sized crystallites will also substantially contribute to long-range ionic conduction. The latter effect has been observed for $LiTaO_3$,[73,98] whose ionic conductivity can be increased by 6 orders of magnitude if mechanically treated for several hours in planetary mills.

To shed light on the kind of disorder or distortions produced and to further characterize the degree of structural disorder of the ball-milled material, we carried out high-resolution ^{31}P MAS and ^{6}Li MAS NMR spectroscopy. While the ^{6}Li NMR signals of the two samples, the microcrystalline starting material and the nanocrystalline product, are identical, ^{31}P MAS NMR reveals a drastic change in line shape (see Figure 3). The ^{31}P MAS spectrum of coarse-grained and, thus,

https://dx.doi.org/10.1021/acs.chemmater.0c01367
Chem. Mater. XXXX, XXX, XXX−XXX

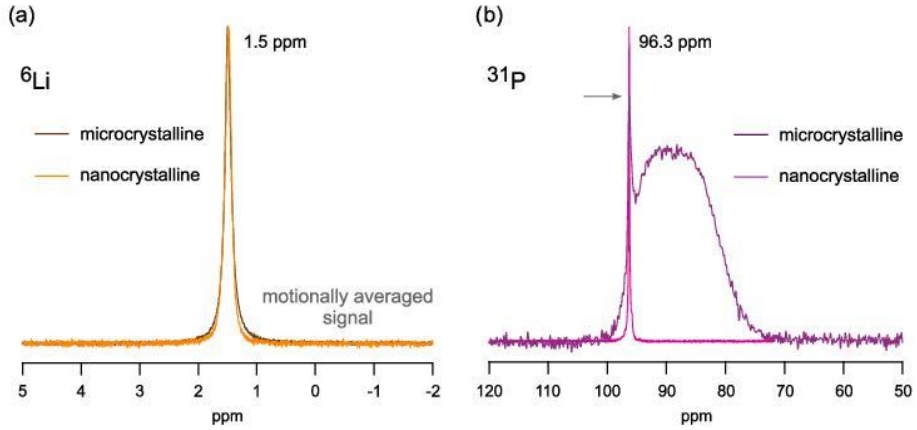

Figure 3. (a) ^{6}Li MAS NMR and (b) ^{31}P MAS NMR spectra of both microcrystalline and nanocrystalline (ball-milled) Li_6PS_5I. The spectra were recorded at 202.4 MHz (^{31}P) and 73.6 MHz (^{6}Li) at a spinning speed of 25 kHz (2.5-mm rotors). The spectra are referenced either to an aqueous LiCl solution or a solution of 85% H_3PO_4; see ref 46 for details.

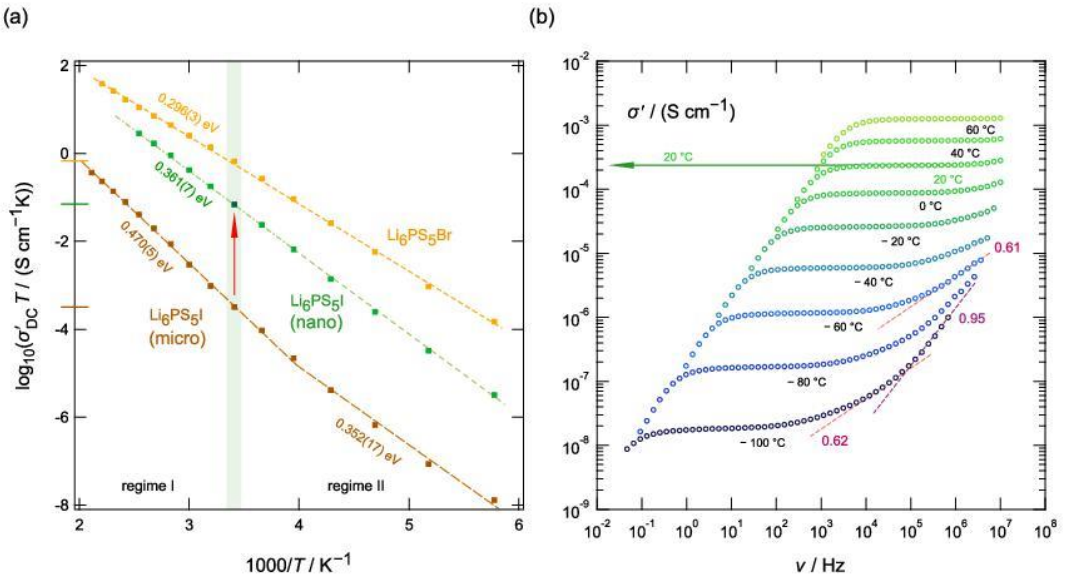

Figure 4. (a) Arrhenius representation of the temperature behavior of ionic DC conductivities plotted as $\log_{10}(\sigma_{DC}T)$ against the inverse temperature expressed as $1000/T$; T denotes the absolute temperature in K. When going from microcrystalline to nanocrystalline Li_6PS_5I, the ionic conductivity near room temperature (see the vertical bar) increases by 2 orders of magnitude. For comparison, data for Li_6PS_5Br are also shown. In agreement with this increase in ionic conductivity, the activation energy reduces from 0.47 to 0.36 eV for $T > 293$ K. (b) So-called conductivity isotherms of nanocrystalline Li_6PS_5I. The isotherms show the dependence of the real part, σ', of the complex conductivity as a function of frequency ν; altogether, we covered a frequency window spanning a range of almost eight decades. Distinct DC plateaus are visible from which σ_{DC} can directly be read off, as indicated for the isotherm referring to $\vartheta = 20$ °C. Dashed lines are used to analyze the frequency dependence in the dispersive regimes according to $\sigma' \propto \nu^p$. $p \rightarrow 1$ indicates the NCL behavior of the electric permittivity. See the text for further explanation.

highly crystalline Li_6PS_5I is composed of a sharp signal located at 96.3 ppm (an aqueous solution of 85% H_3PO_4 served as the primary reference). The line represents the P ions located at the Wyckoff position 4b. The ordered and regular arrangement of the tetrahedra gives rise to a single line; all PS_4^{3-} units are magnetically equivalent. This situation greatly changes after the material has been milled for 120 min. A broad Gaussian-shaped signal appears whose center shifts toward smaller ppm values. The broad signal resembles that of a glassy material with a wide distribution of magnetically inequivalent P sites; a range of different ^{31}P environments has also been observed for $Li_{6-x}PS_{5-x}Br_{1+x}$ quite recently by Wang et al.[61] We assume that defects, polyhedra distortions, and variations in P−S bond lengths are responsible for this drastic change, which is also seen for mechanosynthesized oxides[99] and fluorides.[100,101] The spectrum of nanocrystalline Li_6PS_5I also reveals a residual sharp line at the original position of micro-Li_6PS_5I. This line represents a tiny amount of highly crystalline Li_6PS_5I that survived the milling step as the ZrO_2 balls cannot reach all areas in the milling jars. The area fraction under the line shows that the milled sample consists of 2% of crystalline Li Li_6PS_5I. In conclusion, ^{31}P MAS NMR shows that all P sites experience the effect of ball-milling and not only those near the surface regions. Hence, from an atomic-scale point of view, mechanical treatment converts the entire material into a structurally distorted form. As mentioned above, local defects and severe

https://dx.doi.org/10.1021/acs.chemmater.0c01367
Chem. Mater. XXXX, XXX, XXX−XXX

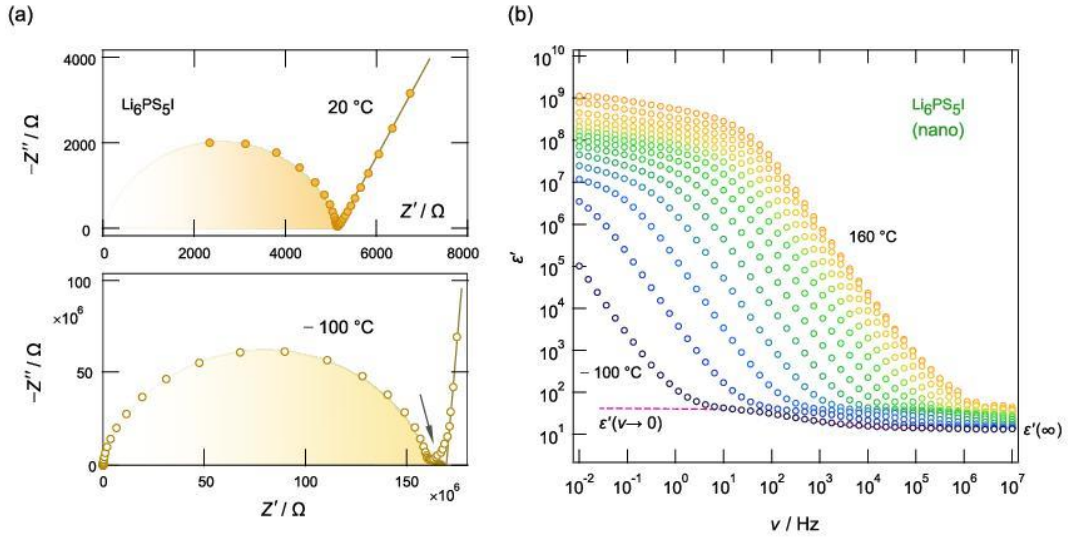

Figure 5. (a) Nyquist representation of the complex impedance response of nanocrystalline Li_6PS_5I measured at two different temperatures (20 and −100 °C). The plot shows the imaginary part, $-Z''$, of the complex impedance, Z, as a function of its real part, $-Z'$. The semicircle seen can be well parameterized with a single R-CPE, which is a resistor R connected in parallel to a constant phase element (CPE). The capacity C turned out to be on the order of a few pF (3.4 pF (20 °C); 4.0 pF (−100 °C)). The spikes seen at low frequencies indicate polarization effects at the ion-blocking electrodes. A tiny semicircle seen in the low-frequency region of the complex plane plot showing the response at −100 °C might indicate some blocking grain boundaries; see the arrow. (b) Permittivity isotherms showing the change of the real part of the complex permittivity, ε', as a function of frequency ν. The dashed line shows the permittivity plateau of the isotherm recorded at −100 °C, pointing to a bulk permittivity of $\varepsilon' = 40$. Isotherms were recorded from $\vartheta = -100$ to 160 °C in steps of 20 °C.

polyhedral distortions are responsible for the ^{31}P response. Such distortions would greatly affect the ^{31}P NMR line but would still produce broadened and clearly visible reflections in X-ray diffraction; see above. The latter fact points to a nanocrystalline material with lattice distortions.

The same structural effect should also be observed using ^6Li MAS NMR. As Li^+ is, however, highly mobile on a local scale also in Li_6PS_5I, the ^6Li MAS NMR line at room temperature already represents a so-called motionally narrowed signal at the temperature at which the spectrum was recorded. In addition, the chemical shift range of ^6Li is much smaller than that of phosphorus. Only low-temperature ^6Li MAS NMR may be able to resolve the magnetically inequivalent Li sites. It has to be noted that our recent ^7Li relaxometry NMR study[46] revealed fast intracage Li ion-exchange processes. These hopping processes, which are spatially confined, are sufficient to cause a coalesced NMR signal under ambient conditions. As mentioned above, the important intercage jump process is much less frequent in Li_6PS_5I as compared to Li_6PS_5X with X = Br, Cl.[67]

Now, we have to ask the question as to whether this important intercage process is switched on in structurally disordered Li_6PS_5I. Indeed, as seen from broad-band conductivity spectroscopy, and in line with similar approaches in the literature,[45] we observe an increase of the room-temperature direct current (DC) ionic conductivity by 2 orders of magnitude as compared to the starting material; see the Arrhenius plot of ionic conductivities shown in Figure 4.

In Figure 4b, the so-called conductivity isotherms of nanocrystalline Li_6PS_5I are shown that were constructed by plotting the real part, σ', of the complex conductivity, σ, as a function of frequency ν. The isotherms reveal a universal shape and indicate a homogeneous matrix with no possibilities to differentiate between amorphous regions and structurally distorted crystalline cores. Dispersive regimes, however, point to intrinsic heterogeneous ion dynamics. At low frequencies, the decrease of σ' for each isotherm reflects the piling up of the Li^+ ions in front of the blocking electrodes applied to the pellets.[68,102] At sufficiently high frequencies, σ' passes into the so-called frequency-independent plateau, which is determined by σ_{DC}. Further increase in ν causes σ' to enter the dispersive regime. While the DC regime reflects successful Li^+ displacements that lead to long-range ion transport,[103] the dispersive regimes give evidence for correlated (forward−backward) jump processes proceeding on a much shorter length scale.[68,103] The dispersive regime is best seen at low temperatures. By comparing the isotherms recorded at −60 °C and at −100 °C, we recognize that this regime is composed of two contributions. We analyzed the frequency dependence with the help of Jonscher's power law ansatz:[104] $\sigma' \propto \nu^p$. The dispersive regime that is directly connected to the DC transport process is given by $\sigma' \propto \nu^{0.61}$; $p \approx 0.6$ is expected for a 3D, correlated jump process.[105] The isotherm recorded at −100 °C reveals a change in exponent p for the high-frequency regime. $p = 0.95$ is a strong indication for a so-called nearly constant loss (NCL) behavior[106−109] meaning that the imaginary part, ε'', of the complex permittivity, ε, is independent of frequency. $p = 1$ is frequently found for materials that provide spatially restricted cation or anion movements. In Li_6PS_5I, we attribute this finding to the localized Li jump processes within the 24g−48h−24g triplet structure of the Li-rich cages. Such cagelike motions were found in materials with pocketlike structures such as $RbAg_4I_5$ being prone to show NCL behavior.[110,111]

The distinct DC plateaus shown in Figure 4b allowed us to easily determine σ_{DC} values with high precision. The associated capacitance values C of the DC conductivity plateau, with its dispersive regime, are in the pF range, i.e., unquestionably referring to a bulk process that is probed by σ_{DC}.[112] As an example, for the room-temperature isotherm, C turned out to

https://dx.doi.org/10.1021/acs.chemmater.0c01367
Chem. Mater. XXXX, XXX, XXX−XXX

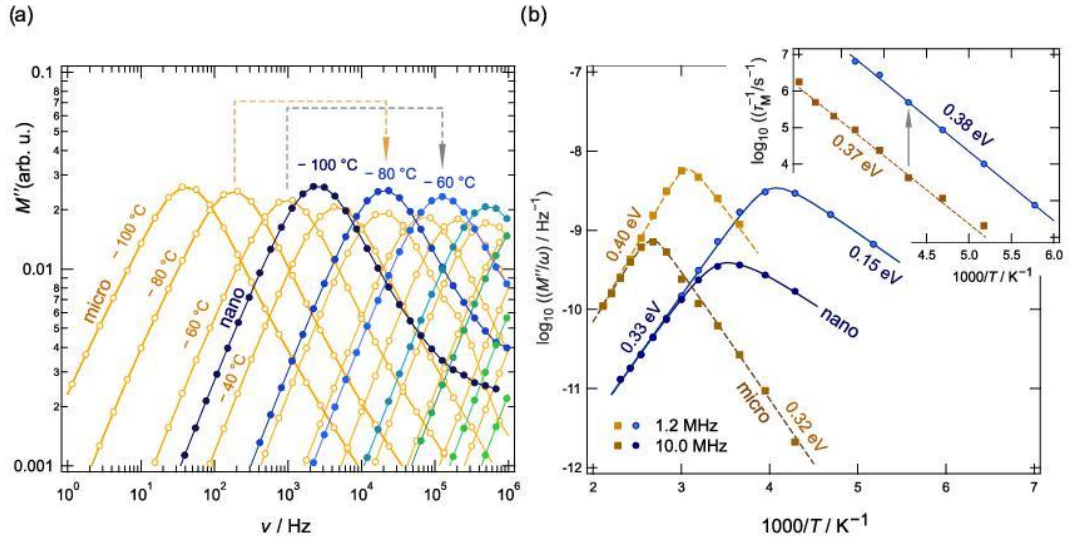

Figure 6. (a) Modulus spectra, $M''(\nu)$, of nanocrystalline Li_6PS_5I, clearly indicating a shift by 2 orders of magnitude when compared to those of polycrystalline, well-ordered Li_6PS_5I not subjected to intense ball-milling. To record the measurements, we used the airtight sample holder, as described in Section 2. (b) Change of the resistivity expressed as M''/ω as a function of the inverse temperature. If plotted in an Arrhenius diagram, $\log_{10}(M''/\omega)$ passes through distinct maxima; the lower the angular frequency ω, the larger the shift toward lower temperatures.

be 3.4 and 4.0 pF is obtained at −100 °C; the corresponding Nyquist plot is shown in Figure 5a. At −100 °C, the permittivities $\varepsilon'(0)$ and $\varepsilon'(\infty)$ take values of 38 and 13.8, respectively; see Figure 5b, which displays the ε'-isotherms of nano-Li_6PS_5I. Hence, there is no evidence for a strong influence of any ion-blocking grain boundary regions, although the volume fraction of such regions is certainly larger in nano-Li_6PS_5I than in its microcrystalline counterpart. This observation is also in agreement with the shape of the conductivity isotherms. At ϑ = 20 °C, σ_{DC} is given by 0.2 mS cm^{-1}, which is higher than the corresponding value of unmilled Li_6PS_5I by 2 orders of magnitude. In fact, the introduction of structural disorder greatly helped to enhance the dynamics. The change of σ_{DC} with temperature, as shown in Figure 4a, was analyzed in terms of an Arrhenius ansatz: $\sigma_{DC}T = \sigma_0 \exp(-E_a/(k_B T))$, where T denotes the absolute temperature, σ_0 is the pre-exponential factor, and k_B is Boltzmann's constant. As a result of high-energy ball-milling, the activation energy for ionic hopping reduces from 0.47 to 0.36 eV. For comparison, in Figure 4a, we included not only the behavior of σ_{DC} for microcrystalline Li_6PS_5I but also that of Li_6PS_5Br, showing an even higher ionic conductivity.[46]

As $\sigma_{DC}T$ also depends on σ_0, we also looked at the associated prefactors.[102] Interestingly, for temperatures above ambient (regime I), σ_0 does not change much when going from microcrystalline to nanocrystalline Li_6PS_5I; it increases only slightly from $\log_{10}(\sigma_0/(\text{S cm}^{-1}\text{ K}))$ = 4.61 (micro-Li_6PS_5I) to 5.05 (nano-Li_6PS_5I). Generally, σ_0 contains a range of parameters, such as the mean jump distance, the migration (and/or formation) entropy for ionic hopping $\Delta S_{m(f)}$, and the attempt frequency ω_a, which are expected to change upon mechanical treatment. Surprisingly, although the degree of structural disorder has largely been increased, the change in σ_0 turned out to be moderate. This finding is, however, only valid for temperatures above ambient. Below ϑ = −20 °C, we see that $\sigma_{DC}T$ of both samples follows Arrhenius lines with the same slope (ca. 0.35 eV; see regime II). The Arrhenius line in the low-T regime of microcrystalline Li_6PS_5I is, however, characterized by a much lower prefactor of only $\log_{10}(\sigma_0/(\text{S cm}^{-1}\text{ K}))$ = 2.25. Hence, ion dynamics in this temperature range is governed by a significant enhancement of σ_0, which turned out to be on the order of almost 3 orders of magnitude; see regime II.

In general, σ_{DC} itself does not only depend on the mobility μ of the charge carriers but also on the charge carrier density N^{-1}, $\sigma_{DC} \propto \mu N^{-1}$. To study any change of N^{-1}, also whether it is a function of temperature, we took advantage of the electric modulus representation to analyze ion dynamics in nanocrystalline Li_6PS_5I. The complex modulus M is given by the inverse of the complex permittivity $1/\varepsilon$.[78,113] In Figure 6, its imaginary part, M'', is plotted vs frequency ν. The peak frequency, $\nu_{max} = 1/\tau_M$, can be interpreted as a characteristic relaxation frequency that is proportional to the (mean) hopping rate of the Li^+ ions $1/\tau$. Each peak corresponds to the σ_{DC} plateau in Figure 4b.

First, we see that for each temperature a single $M''(\nu)$ peak appears; even in the half-logarithmic plot used to analyze the data, no shoulders or minor peaks with reduced amplitude appear. Again, electrical relaxation in nano-Li_6PS_5I appears homogeneously, with no distinct differences between amorphous and (distorted) crystalline regions. In general, as $M_{max} \propto 1/C$, peaks with reduced amplitude would be diagnostic for any relaxation processes that are being characterized by large capacitance values, e.g., expected for electrical relaxation processes influenced by thin grain boundary regions. Here, we do not find any hints that amorphous regions block ion dynamics; on the contrary, structural distortions enhance ionic transport. Other materials might behave differently; as an example, amorphous regions in Li_7SiPS_8, as shown by Lotsch and co-workers, limit intergrain ionic conductivity and have a detrimental effect on through-going ion transport.[114]

Second, we notice that the $M''(\nu)$ peaks for nanocrystalline Li_6PS_5I are shifted toward higher frequencies. Since Li^+ ion dynamics is fast in nanocrystalline Li_6PS_5I, the $M''(\nu)$ analysis covers only the low-temperature regime. The shift of the peak maxima by 2 orders of magnitude is similar to but not exactly

https://dx.doi.org/10.1021/acs.chemmater.0c01367
Chem. Mater. XXXX, XXX, XXX−XXX

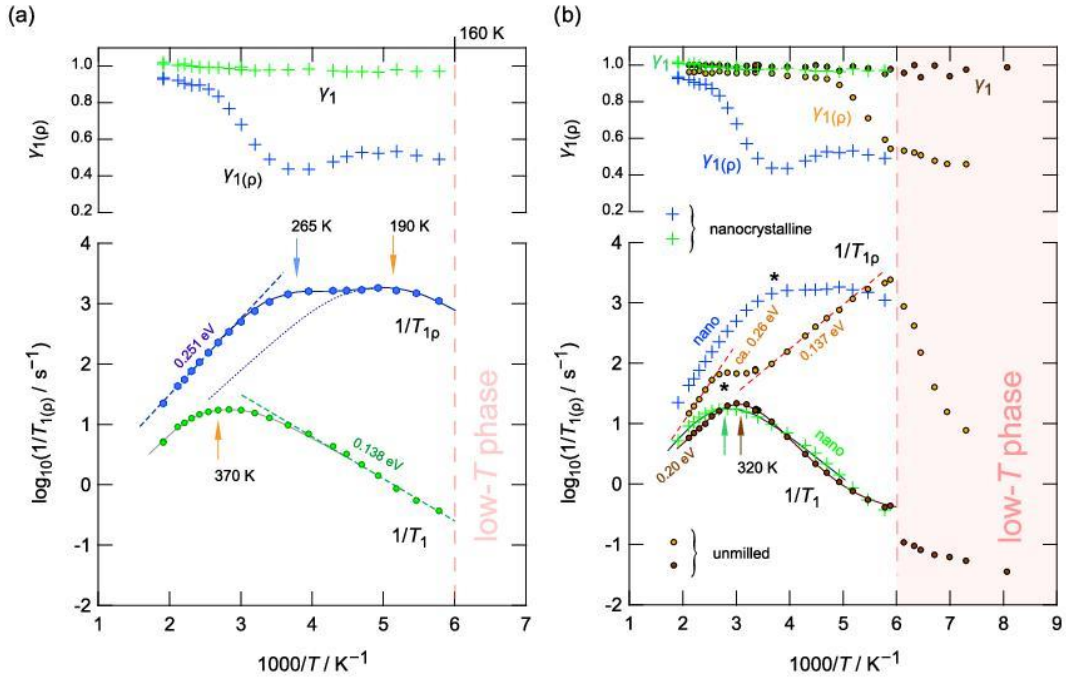

Figure 7. (a) Arrhenius plot showing the temperature behavior of the ^{7}Li NMR spin-lattice relaxation rates of nanocrystalline Li_6PS_5I measured in both the laboratory ($1/T_1$, 116 MHz) and the rotating frame of reference ($1/T_{1(\rho)}$). The lines show linear fits to extract the activation energies, E_a, indicated. Arrows point to the peak maxima. A reversible phase transition occurs at ca. 165 K. (b) The same figure as in (a) but with the inclusion of ^{7}Li NMR rates of microcrystalline Li_6PS_5I; the rates of nano-Li_6PS_5I are indicated by crosses (+). Whereas the $1/T_1$ peaks reflect fast intracage ion dynamics with almost the same jump rates in the two samples, $1/T_{1(\rho)}$ shows that upon ball-milling, the shallow peak seen at 360 K (0.26 eV) for micro-Li_6PS_5I gains in intensity and shifts by 100 K toward lower T; see the two asterisks (*). See the text for further explanation.

the same as that seen for $\sigma_{DC}T$ in this low-T regime (vide supra), as σ_0 increases by more than a factor of 100 below ambient temperature. This agreement in comparison tells us that the increase in σ_{DC} can be mainly attributed to an enhancement of μ but also to an enhancement of N^{-1}. As E_a remains almost unchanged, we suppose that the boost in the mobility of the Li^+ ions below ambient temperature has to be attributed to a change of either the attempt frequency ω_a or the activation entropy ΔS, assuming that the influence of other factors governing σ_0 cannot produce such a large increase.

By comparing E_a of microcrystalline Li_6PS_5I from both the $\sigma_{DC}T$ analysis and from $M''(\nu)$, we recognize that the two corresponding activation energies (0.47 eV, see Figure 4a; 0.37 eV, see Figure 6b) differ by approximately 0.1 eV. Provided both techniques sense the same electrical relaxation process, and only in this case, the steeper increase in σ_{DC} can be explained by a temperature-dependent charge carrier concentration $N^{-1} = f(1/T)$, which itself follows an Arrhenius-like behavior with an activation energy of ca. 0.1 eV. In such a case, $\sigma_{DC}T$ would increase faster with $1/T$ than $1/\tau_M$. This behavior contrasts with that seen for nanocrystalline Li_6PS_5I. For nano-Li_6PS_5I, we notice that the two activation energies (0.36 eV ($\sigma_{DC}T$); (0.38 eV (M'')) are very similar. In fact, the increase of $1/\tau_M$ is even slightly more pronounced than that seen for $\sigma_{DC}T$. Roughly speaking, for structurally disordered nano-Li_6PS_5I, having a large number of defect sites and locally distorted regions, we find evidence for a charge carrier concentration N^{-1} that is almost temperature independent but larger than that in the microcrystalline sample. This finding is in line with the general understanding of ion dynamics in the solid state: disorder, distortions, and a higher number fraction of (point) defects ensure a high, in many cases temperature independent, number density of charge carriers.

To conclude, at low T, the increase in σ_{DC} for the ball-milled sample is due to an enhanced Arrhenius prefactor and, to a lesser degree, also an enhanced number fraction of mobile charge carriers. At temperatures higher than ambient, the lower conductivity of the microcrystalline sample increases stronger than expected, as N^{-1} increases for this sample with temperature. Interpreting the higher activation energy (0.47 eV) of microcrystalline Li_6PS_5I in terms of $N^{-1} = f(1/T)$, we have to conclude that the activation energy for the intercage jump is comparable to that in compounds with X = Cl or Br; it is, however, governed by a much lower prefactor τ_0^{-1} in $\tau^{-1} = \tau_0^{-1}\exp(-E_a/(k_BT))$. This conclusion is in line with the soft lattice concept developed earlier for this class of materials.[42,65]

Finally, we used resistivity measurements, M''/ω,[115] to extract activation energies over a larger dynamic range; see Figure 6b. The above-mentioned analysis of modulus peaks was restricted to temperatures where the peaks $M''(\nu)$ appear at frequencies that correspond to the crossover from $\sigma' = \sigma_{DC}$ to $\sigma' \propto \nu^p$. Analyzing M''/ω at frequencies of 1.2 and 10 MHz allows, however, for the detection of both long-range ion dynamics and short-range ion-hopping processes, as it is also possible via ^{7}Li NMR relaxometry[116] (see Figure 7). For nanocrystalline Li_6PS_5I, a plot of $\log_{10}(M''/\omega)$ vs $1000/T$ reveals asymmetric peaks whose flanks characterize length-scale-dependent ion dynamics (Figure 6b). While E_a referring to the high-T flank is somehow comparable to E_a from $M''(\nu)$, particularly for microcrystalline Li_6PS_5I, we clearly see that for nano-Li_6PS_5I, an asymmetric peak appears, pointing to a large distribution of jump processes as a consequence of a highly

https://dx.doi.org/10.1021/acs.chemmater.0c01367
Chem. Mater. XXXX, XXX, XXX−XXX

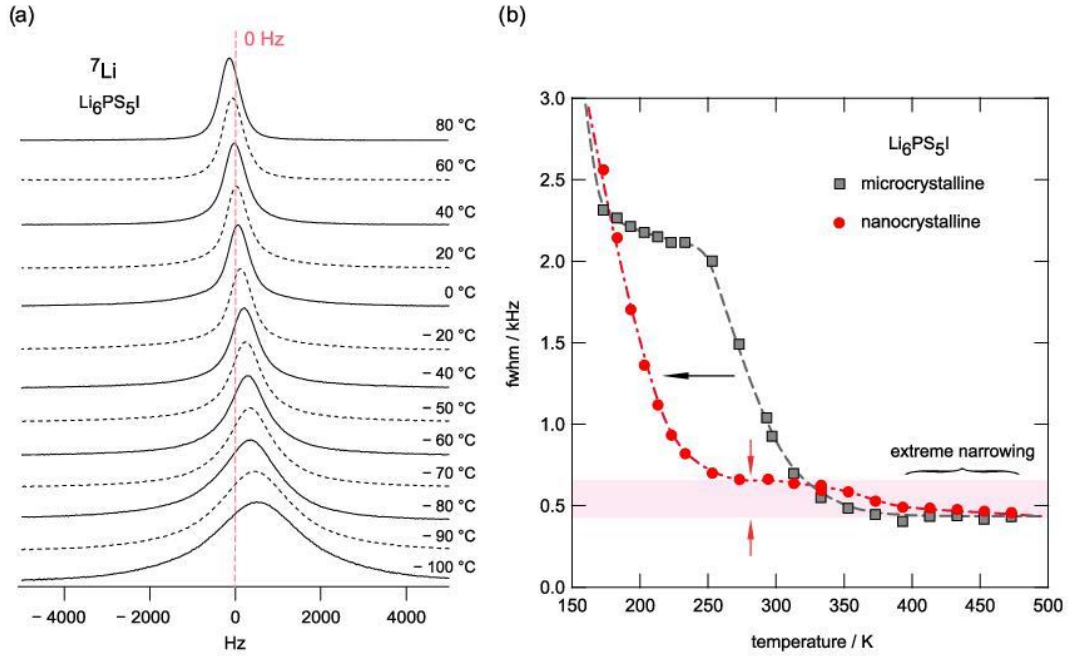

Figure 8. (a) ^{7}Li NMR line shapes of nanocrystalline Li_6PS_5I measured at the temperatures indicated. At low temperatures, the line shape resembles that of a Gaussian line, which, as a consequence of motional averaging of homonuclear dipole−dipole interactions, turned into a Lorentzian at elevated T. (b) Plot of the NMR line widths (fwhm = full width at half-maximum) directly read off from the lines shown in (a). For the nanocrystalline sample, the second decay step of the narrowing curve s shifted by approximately 100 K toward lower T, giving evidence that the boost in DC conductivity affects almost all Li ions in nanocrystalline Li_6PS_5I.

irregular energy landscape. The stronger this asymmetry, the more heterogeneous the Li^+ ion dynamics.

The activation energy of the low-T flank of the M''/ω peaks is given by 0.15 eV. Such a low value should also be detectable by ^{7}Li NMR spin-lattice relaxation measurements (see Figure 7).[69,88,116] Indeed, the diffusion-induced ^{7}Li NMR spin-lattice relaxation rates $1/T_1$ and $1/T_{1\rho}$, measured either in the laboratory frame or in the rotating frame of reference, yield lower E_a values than that seen by σ_{DC}, which is solely sensitive to successful ion jump processes. Localized processes, forward−backward jumps, and within-site movements are, on the other hand, detectable by nuclear spin relaxation in addition.[88]

The rates presented in Figure 7 were determined from diffusion-induced magnetization transients $M_{1(\rho)}(t_{(lock)})$ that were analyzed with stretched exponential functions. The stretching exponents $\gamma_{1(\rho)}$ are shown in the upper graphs of Figure 7. While $1/T_1$ relaxation follows almost mono-exponential time behavior ($\gamma_1 \approx 1$), the exponents characterizing the transients corresponding to spin-lock relaxation ($1/T_{1\rho}$) strongly depend on temperature and can only be parametrized by stretched functions: $M_{1\rho}(t_{lock}) \propto \exp(-(t/T_{1(\rho)})^{\gamma})$.[117] Note that $1/T_1$ senses ion dynamics on the MHz time scale ($\omega_0/2\pi$ = 116 MHz), while $1/T_{1\rho}$ probes magnetic fluctuations in the kHz regime; we used a spin-lock frequency of $\omega_1/2\pi$ = 20 kHz to record the $1/T_{1\rho}$ rates. We see that the $1/T_1(1/T)$ peak is asymmetric in shape, with the low-T side being characterized by 0.138 eV. This value is highly comparable to those deduced from the asymmetric M''/ω peaks (see Figure 6b) and represents short-range ion dynamics in the nanocrystalline sample. In general, a $1/T_1(1/T)$ NMR rate peak occurs when the mean Li^+ jump rate τ^{-1}, which is within a factor of two identical to the underlying motional correlation rate τ_c^{-1},[118,119] reaches the order of the Larmor (ω_0) or locking (ω_1) frequency. Thus, at the peak maximum, we have $\tau_c^{-1}\omega_{0(1)} \approx 1$.[69] The lower the $\omega_{0(1)}$, the more the peak shifts toward lower temperatures.

At first glance, the $1/T_1(1/T)$ peak observed for nanocrystalline Li_6PS_5I is almost identical to that measured for its microcrystalline counterpart; see Figure 7b. It is worth noting that both peaks are produced by extremely fast localized ion-exchange processes restricted to the Li cages in Li_6PS_5I (0.138 eV (nanocrystalline Li_6PS_5I), 0.20 eV (microcrystalline Li_6PS_5I); see Figure 7a,b). As has been discussed recently for microcrystalline Li_6PS_5X (X = Br, Cl, I),[46] these processes are sufficiently fast to generate a full relaxation rate peak, which is comparable to those seen for Li_6PS_5Br and Li_6PS_5Cl. Regardless of whether the intercage exchange process is fast or slow, this relaxation peak showing facile intracage ion dynamics is a universal feature[46] for all types of Li-bearing argyrodites with the structural motifs shown in Figure 1. It is also in line with the coalesced (motionally averaged) ^{6}Li MAS NMR signal seen at ambient bearing gas pressure (see Figure 3a).

Importantly, for microcrystalline Li_6PS_5I, a symmetric peak $1/T_1(1/T)$ is seen. Obviously, Li_6PS_5I seems to be a good model system to study the influence of structural disorder on the nuclear spin relaxation.[120] Our observation supports the general idea that structural disorder and Coulomb interactions produce this asymmetry in materials with strongly heterogeneous ion dynamics.[121−123]

We realize that the boost in σ_{DC} affecting long-range ion dynamics is hardly seen in $1/T_1$ relaxation. On the contrary, careful inspection reveals that the $1/T_1(1/T)$ peak of nano-Li_6PS_5I is even shifted by 50 K toward higher T; see below. Hence, the introduction of polyhedral distortions slows down

https://dx.doi.org/10.1021/acs.chemmater.0c01367
Chem. Mater. XXXX, XXX, XXX−XXX

local, intracage ion dynamics (vide infra). Simultaneously, long-range diffusion is, however, switched on for nano-Li_6PS_5I. The latter change in conduction properties clearly leaves its marks in spin-lock $1/T_{1\rho}$ NMR relaxation, being sensitive to ion dynamics on a longer length scale.

Starting with $1/T_{1\rho}(1/T)$ of micro-Li_6PS_5I, the peak corresponding to $1/T_1$ is expected to appear at temperatures near or below the temperature T_{tr} at which Li_6PS_5I reversibly transforms into a low-T modification; see Figure 7b. Above T_{tr}, we probe a high-T flank whose slope seems to be governed by the intracage jump processes. Near 360 K, a shallow $1/T_{1\rho}(1/T)$ peak is seen whose origin was unclear so far. Its high-T side is characterized by an activation energy of 0.26 eV. Most interestingly, $1/T_{1\rho}(1/T)$ of the nanocrystalline material helps identify this relaxation process. Again, the $1/T_{1\rho}(1/T)$ peaks associated with that seen in T_1 are expected at very low temperatures. Indeed, the rates pass through such a shallow peak at ca. 190 K. Surprisingly, another peak is seen at a higher temperature of 265 K (see Figure 7a). We anticipate that this peak corresponds to the one also seen for the microcrystalline sample but at much higher temperatures. Obviously, as this turned out to be the main difference in nuclear spin relaxation of the two samples, the peak might reflect additional diffusion processes taking place in nanocrystalline Li_6PS_5I. These additional processes might take advantage of interstitial Li positions connecting the Li cages; see Figure 1. Most likely, these sites become partly occupied by the Li^+ ions as a consequence of ball-milling. Such sites have been suggested on the basis of molecular dynamics simulations (500 K) by Pecher et al.,[47] who called them type 2, type 3, and type 4. The free enthalpies, when referenced to the site energies of the regularly occupied Li^+ sites (see Figure 1), turned out to be 0.27, 0.39, and 0.14 eV. These values agree with those probed by NMR and electrical spectroscopy; see Figures 4, 6, and 7.

Going back to spin-lattice relaxation NMR, we recognize that the additional spin-lock nuclear relaxation process cannot serve as the only explanation for the enhancement seen in σ_{DC}, as one would expect the corresponding $1/T_{1\rho}(1/T)$ to be shifted to even lower temperatures to explain values of 0.2 mS cm^{-1} at 20 °C. We assume that ball-milling also affects the direct intercage Li^+ hopping process as this is the process needed to enable the ions to move over long distances. Possibly, this process is also influenced by interstitial sites located between the Li cages. As mentioned above, we suppose that these are easily reachable for the Li ions in structurally distorted Li_6PS_5I. These intercage jump processes are, however, "switched off" for microcrystalline Li_6PS_5I as can be clearly probed by variable-temperature ^7Li NMR line-shape measurements (see Figure 8a).[46] Whereas for Li_6PS_5X, the static NMR line width reaches its limiting value well below room temperature, Li_6PS_5I shows a so-called two-step decay behavior.

With increasing temperature, the fast intracage hopping processes are able to considerably average dipole−dipole interactions mainly determining the broad NMR line in the so-called rigid lattice at low temperatures. This averaging remains, however, incomplete until 300 K as, up to this temperature, the intercage jump rate is lower than the spectral width of the NMR line. Above 300 K, the exchange rate reaches values finally affecting the line width, which results in full narrowing. For nanocrystalline Li_6PS_5I, averaging via intercage hopping is much more effective as shown in Figure 8b: at 300 K, the line width has almost reached its final value. Note that the nanocrystalline sample still resembles the behavior of the nonmilled sample as a shallow two-step behavior is still detectable. The regime of extreme narrowing is reached at a temperature above 400 K.

Before summarizing our results, we go back to the $1/T_1(1/T)$ peaks seen in Figure 7b. As mentioned above, by precisely comparing the position of the two $1/T_1(1/T)$ peaks, i.e., before and after mechanical treatment, we recognize that the peak for nano-Li_6PS_5I appears at somewhat higher T (370 K) than that for the microcrystalline counterpart (320 K). In agreement with this shift, which is indicated by the vertical two arrows in Figure 7b, also the corresponding $1/T_{1(\rho)}(1/T)$ of nano-Li_6PS_5I is shifted to higher T and becomes detectable for this sample at ca. 190 K (see Figure 7a). In contrast, for microcrystalline Li_6PS_5I, the spin-lock rates do not reach the peak maximum before T = 160 K. These consistent shifts indicate that the intracage process in disordered, nanocrystalline Li_6PS_5I slightly slowed down. Obviously, as concluded above, this decrease has no detrimental effect on long-range ion transport as ionic mobility is determined by the number of successful intercage jump events. The latter seems to greatly benefit from the structural distortions introduced.

To sum up, Li_6PS_5I served as an attractive and highly suitable model system to show how mechanical treatment, that is, the introduction of structural disorder, is able to convert poor ion conductors into highly conducting electrolytes. For the materials studied so far, e.g., $LiTaO_3$, $LiNbO_3$, and $LiAlO_2$, this concept resulted in conductivities of 10^{-6} S cm^{-1}. In the present case, high-energy ball-milling was successfully applied to reach DC conductivities almost approaching the mS regime. Changing the milling conditions and increasing the milling time might lead to materials showing even higher conductivities.

Preliminary experiments show that nano-Li_6PS_5I can completely be reconverted into its crystalline form. Reordering sets in at temperatures as high as 200 °C; a fully crystalline sample is reobtained after heat treatment at 500 °C already for 2 h. This sample shows the same conductivity isotherms (with regimes I and II) as that of the initial one. In addition, we saw that ^7Li NMR $1/T_1$ measurements carried out at constant temperatures of 200 and 160 °C for 2 h led to a continuous decrease of the rate. This decrease indicates that the original peak $1/T_1(1/T)$ is reobtained. Note that the difference in $1/T_1$ for nano-Li_6PS_5I and unmilled Li_6PS_5I is rather small due to the fast, localized motions governing spin-lattice relaxation in both forms. Importantly, when the sample was left inside the glovebox for 3 months (at 25 °C), we also observed reordering and a significant drop in ionic conductivity. The same change has been observed quite recently for mechanosynthesized $RbSn_2F_5$.[115] The latter, also showing high F anion conductivity, is metastable if present in a nanocrystalline, distorted form. We anticipated that fast ion dynamics triggers reordering of such samples. The same could be the case for nano-Li_6PS_5I. Thus, the structural stability of disordered samples has to be kept in mind if we think about the implementation of distorted fast ion conductors in batteries.

A systematic study on the influence of the milling conditions and subsequent thermal treatment is currently under way in our laboratory. Such a study is, however, beyond the scope of the present investigation. The initial results indicate that increasing the milling time to 4 h does not significantly change the room temperature of Li_6PS_5I. Hence, we conclude that a limiting value for σ_{DC} is already reached after 2 h. Also, for

https://dx.doi.org/10.1021/acs.chemmater.0c01367
Chem. Mater. XXXX, XXX, XXX−XXX

some oxides, a very similar dependence on milling time is seen: the main structural changes occur during the early steps of milling.[73,98] We assume that Li_6PS_5I might be converted into a fully amorphous phase if one doubles the number of milling balls. A total of 60 balls, as used here, is rather low for mechanochemical synthesis under dry conditions.

4. CONCLUSIONS

Li_6PS_5I, with its ordered anion sublattice, shows fast Li^+ jump processes on a local scale, most likely restricted to translational intracage ion dynamics. Unfortunately, the important intercage hopping processes occur less frequently, resulting in poor ionic DC conductivities with a value on the order of 1 μS cm^{-1} under ambient conditions. High-energy ball-milling was used to introduce structural disorder, such as point defects, polyhedra distortions, and strain, to boost ion dynamics up to DC conductivities of 0.2 mS cm^{-1} at 20 °C. X-ray diffraction and ^{31}P NMR helped us to characterize the extent of structural disorder. Broad-band conductivity spectroscopy and the analysis of electric modulus spectra show that both a change in charge carrier mobility, through enhanced Arrhenius prefactors, and an increase in charge carrier concentration seem to be responsible for this increase. Variable-temperature spin-lock ^{7}Li nuclear spin relaxation revealed that in nanocrystalline Li_6PS_5I one of the diffusion processes seen is clearly enhanced as compared to the unmilled starting material. We assume that structural distortions enhance the intercage jump rate, leading to through-going Li^+ diffusion. Most likely, interstitial sites assist in Li^+ diffusivity as they might be easily reachable for the Li ions in structurally distorted Li_6PS_5I. Thus, the iodide represents an attractive application-oriented model system to study the effect of structural disorder on the elementary steps of ion hopping. We showed that soft mechanical treatment is able to convert poor ionic conductors into highly conducting electrolytes, with DC conductivities almost reaching values in the mS cm^{-1} regime.

AUTHOR INFORMATION

Corresponding Author

H. Martin R. Wilkening − *Institute for Chemistry and Technology of Materials, Christian Doppler Laboratory for Lithium Batteries, Graz University of Technology (NAWI Graz), 8010 Graz, Austria;* orcid.org/0000-0001-9706-4892; Email: wilkening@tugraz.at

Authors

Marina Brinek − *Institute for Chemistry and Technology of Materials, Christian Doppler Laboratory for Lithium Batteries, Graz University of Technology (NAWI Graz), 8010 Graz, Austria*

Caroline Hiebl − *Institute for Chemistry and Technology of Materials, Christian Doppler Laboratory for Lithium Batteries, Graz University of Technology (NAWI Graz), 8010 Graz, Austria*

Complete contact information is available at: https://pubs.acs.org/10.1021/acs.chemmater.0c01367

Author Contributions

The authors declare no competing interests.

Author Contributions

†M.B. and C.H. contributed equally to this work.

Notes

The authors declare no competing financial interest.

ACKNOWLEDGMENTS

Financial support from the Austrian Federal Ministry of Science, Research and Economy (BMWFW) and the National Foundation for Research, Technology and Development is gratefully acknowledged. In addition, the study received considerable funding from the European Union's Horizon 2020 research and innovation program under the grant agreement no. 769929. Furthermore, we thank the DFG for financial support (WI3600 4-1, 2-1; research unit FOR 1277).

REFERENCES

(1) Dunn, B.; Kamath, H.; Tarascon, J. M. Electrical Energy Storage for the Grid: a Battery of Choices. *Science* **2011**, *334*, 928−935.

(2) Larcher, D.; Tarascon, J. M. Towards Greener and More Sustainable Batteries for Electrical Energy Storage. *Nat. Chem.* **2015**, *7*, 19−29.

(3) Wu, F.; Maier, J.; Yu, Y. Guidelines and trends for next-generation rechargeable lithium and lithium-ion batteries. *Chem. Soc. Rev.* **2020**, *49*, 1569−1614.

(4) Takada, K. Progress and prospective of solid-state lithium batteries. *Acta Mater.* **2013**, *61*, 759−770.

(5) Gao, Z.; Sun, H.; Fu, L.; Ye, F.; Zhang, Y.; Luo, W.; Huang, Y. Promises, Challenges, and Recent Progress of Inorganic Solid-State Electrolytes for All-Solid-State Lithium Batteries. *Adv. Mater.* **2018**, *30*, No. 1705702.

(6) Janek, J.; Zeier, W. G. A solid future for battery development. *Nat. Energy* **2016**, *1*, No. 16141.

(7) Zhang, Z. Z.; Shao, Y. J.; Lotsch, B.; Hu, Y. S.; Li, H.; Janek, J.; Nazar, L. F.; Nan, C. W.; Maier, J.; Armand, M.; Chen, L. Q. New Horizons for Inorganic Solid State Ion Conductors. *Energy Environ. Sci.* **2018**, *11*, 1945−1976.

(8) Hatzell, K. B.; Chen, X. C.; Cobb, C. L.; Dasgupta, N. P.; Dixit, M. B.; Marbella, L. E.; McDowell, M. T.; Mukherjee, P. P.; Verma, A.; Viswanathan, V.; Westover, A. S.; Zeier, W. G. Challenges in Lithium Metal Anodes for Solid-State Batteries. *ACS Energy Lett.* **2020**, *5*, 922−934.

(9) Xu, L.; Tang, S.; Cheng, Y.; Wang, K.; Liang, J.; Liu, C.; Cao, Y.-C.; Wei, F.; Mai, L. Interfaces in Solid-State Lithium Batteries. *Joule* **2018**, *2*, 1991−2015.

(10) Krauskopf, T.; Hartmann, H.; Zeier, W. G.; Janek, J. Toward a Fundamental Understanding of the Lithium Metal Anode in Solid-State Batteries — An Electrochemo-Mechanical Study on the Garnet-Type Solid Electrolyte $Li_{6.25}Al_{0.25}La_3Zr_{2O12}$. *ACS Appl. Mater. Interfaces* **2019**, *11*, 14463−14477.

(11) Richards, W. D.; Miara, L. J.; Wang, Y.; Kim, J. C.; Ceder, G. Interface Stability in Solid-State Batteries. *Chem. Mater.* **2016**, *28*, 266−273.

(12) Wenzel, S.; Randau, S.; Leichtweiss, T.; Weber, D. A.; Sann, J.; Zeier, W. G.; Janek, J. Direct observation of the interfacial instability of the fast ionic conductor $Li_{10}GeP_2S_{12}$ at the lithium metal anode. *Chem. Mater.* **2016**, *28*, 2400−2407.

(13) Dewald, G. F.; Ohno, S.; Kraft, M. A.; Koerver, R.; Till, P.; Vargas-Barbosa, N. M.; Janek, J.; Zeier, W. G. Experimental Assessment of the Practical Oxidative Stability of Lithium Thiophosphate Solid Electrolytes. *Chem. Mater.* **2019**, *31*, 8328−8337.

(14) Schwietert, T. K.; Arszelewska, V. A.; Wang, C.; Yu, C.; Vasileiadis, A.; de Klerk, N. J. J.; Hageman, J.; Hupfer, T.; Kerkamm, I.; Xu, Y.; van der Maas, E.; Kelder, E. M.; Ganapathy, S.; Wagemaker, M. Clarifying the relationship between redox activity and electrochemical stability in solid electrolytes. *Nat. Mater.* **2020**, *19*, 428−435.

(15) Chen, S.; Xie, D.; Liu, G.; Mwizerwa, J. P.; Zhang, Q.; Zhao, Y.; Xu, X.; Yao, X. Sulfide solid electrolytes for all-solid-state lithium

batteries: structure, conductivity, stability and application. *Energy Storage Mater.* **2018**, *14*, 58−74.
(16) Chen, H. M.; Maohua, C.; Adams, S. Stability and ionic mobility in argyrodite-related lithium-ion solid electrolytes. *Phys. Chem. Chem. Phys.* **2015**, *17*, 16494−16506.
(17) Thangadurai, V.; Narayanan, S.; Pinzaru, D. Garnet-type solid-state fast Li ion conductors for Li batteries: critical review. *Chem. Soc. Rev.* **2014**, *43*, 4714−4727.
(18) Bachman, J. C.; Muy, S.; Grimaud, A.; Chang, H. H.; Pour, N.; Lux, S. F.; Paschos, O.; Maglia, F.; Lupart, S.; Lamp, P.; Giordano, L.; Shao-Horn, Y. Inorganic Solid-State Electrolytes for Lithium Batteries: Mechanisms and Properties Governing Ion Conduction. *Chem. Rev.* **2016**, *116*, 140−162.
(19) Uitz, M.; Epp, V.; Bottke, P.; Wilkening, M. Ion Dynamics in Solid Electrolytes for Lithium Batteries. *J. Electroceram.* **2017**, *38*, 142−156.
(20) Ohno, S.; Banik, A.; Dewald, G. F.; Kraft, M. A.; Krauskopf, T.; Minafra, N.; Till, P.; Weiss, M.; Zeier, W. G. Materials design of ionic conductors for solid state batteries. *Prog. Energy* **2020**, *2*, No. 022001.
(21) Knauth, P. Inorganic Solid Li ion Conductors: An Overview. *Solid State Ionics* **2009**, *180*, 911−916.
(22) Wang, Y.; Richards, W. D.; Ong, S. P.; Miara, L. J.; Kim, J. C.; Mo, Y. F.; Ceder, G. Design Principles for Solid-State Lithium Superionic Conductors. *Nat. Mater.* **2015**, *14*, 1026−1031.
(23) Kamaya, N.; Homma, K.; Yamakawa, Y.; Hirayama, M.; Kanno, R.; Yonemura, M.; Kamiyama, T.; Kato, Y.; Hama, S.; Kawamoto, K.; Mitsui, A. A lithium superionic conductor. *Nat. Mater.* **2011**, *10*, 682−686.
(24) Kato, Y.; Hori, S.; Saito, T.; Suzuki, K.; Hirayama, M.; Mitsui, A.; Yonemura, M.; Iba, H.; Kanno, R. High-power all-solid-state batteries using sulfide superionic conductors. *Nat. Energy* **2016**, *1*, No. 16030.
(25) de Jongh, P. E.; Blanchard, D.; Matsuo, M.; Udovic, T. J.; Orimo, S. Complex hydrides as room-temperature solid electrolytes for rechargeable batteries. *Appl. Phys. A* **2016**, *122*, 251.
(26) Aono, H. Ionic Conductivity of Solid Electrolytes Based on Lithium Titanium Phosphate. *J. Electrochem. Soc.* **1990**, *137*, 1023.
(27) Kuhn, A.; Gerbig, O.; Zhu, C. B.; Falkenberg, F.; Maier, J.; Lotsch, B. V. A New Ultrafast Superionic Li-Conductor: Ion Dynamics in $Li_{11}Si_2PS_{12}$ and Comparison with other Tetragonal LGPS-Type Electrolytes. *Phys. Chem. Chem. Phys.* **2014**, *16*, 14669−14674.
(28) Kuhn, A.; Duppel, V.; Lotsch, B. V. Tetragonal $Li_{10}GeP_2S_{12}$ and Li_7GePS_8 - Exploring the Li Ion Dynamics in LGPS Li Electrolytes. *Energy Environ. Sci.* **2013**, *6*, 3548−3552.
(29) Liu, Z. C.; Fu, W. J.; Payzant, E. A.; Yu, X.; Wu, Z. L.; Dudney, N. J.; Kiggans, J.; Hong, K. L.; Rondinone, A. J.; Liang, C. D. Anomalous high ionic conductivity of nanoporous β-Li_3PS_4. *J. Am. Chem. Soc.* **2013**, *135*, 975−978.
(30) Tatsumisago, M.; Hayashi, A. Superionic glasses and glass-ceramics in the Li_2S-P_2S_5 system for all-solid-state lithium secondary batteries. *Solid State Ionics* **2012**, *225*, 342−345.
(31) Seino, Y.; Ota, T.; Takada, K.; Hayashi, A.; Tatsumisago, M. A sulphide lithium super ion conductor is superior to liquid ion conductors for use in rechargeable batteries. *Energy Environ. Sci.* **2014**, *7*, 627−631.
(32) Yamane, H.; Shibata, M.; Shimane, Y.; Junke, T.; Seino, Y.; Adams, S.; Minami, K.; Hayashi, A.; Tatsumisago, M. Crystal structure of a superionic conductor, $Li_7P_3S_{11}$. *Solid State Ionics* **2007**, *178*, 1163−1167.
(33) Yao, X. Y.; Liu, D.; Wang, C. S.; Long, P.; Peng, G.; Hu, Y. S.; Li, H.; Chen, L. Q.; Xu, X. X. High-Energy All-Solid-State Lithium Batteries with Ultralong Cycle Life. *Nano Lett.* **2016**, *16*, 7148−7154.
(34) Wang, Y.; Lu, D.; Bowden, M.; El Khoury, P. Z.; Han, K. S.; Deng, Z. D.; Xiao, J.; Zhang, J.-G.; Liu, J. Mechanism of Formation of $Li_7P_3S_{11}$ Solid Electrolytes through Liquid Phase Synthesis. *Chem. Mater.* **2018**, *30*, 990−997.
(35) Deiseroth, H. J.; Kong, S. T.; Eckert, H.; Vannahme, J.; Reiner, C.; Zaiss, T.; Schlosser, M. Li_6PS_5X: A Class of Crystalline Li-Rich Solids with an Unusually High Li^+ Mobility. *Angew. Chem., Int. Ed.* **2008**, *47*, 755−758.
(36) Zhou, L. D.; Assoud, A.; Zhang, Q.; Wu, X. H.; Nazar, L. F. New Family of Argyrodite Thioantimonate Lithium Superionic Conductors. *J. Am. Chem. Soc.* **2019**, *141*, 19002−19013.
(37) Zhou, L. D.; Park, K. H.; Sun, X. Q.; Lalere, F.; Adermann, T.; Hartmann, P.; Nazar, L. F. Solvent-Engineered Design of Argyrodite Li_6PS_5X (X = Cl, Br, I) Solid Electrolytes with High Ionic Conductivity. *ACS Energy Lett.* **2019**, *4*, 265−270.
(38) Wang, H.; Yu, C.; Ganapathy, S.; van Eck, E. R. H.; van Eijck, L.; Wagemaker, M. A Lithium Argyrodite $Li_6PS_5Cl_{0.5}Br_{0.5}$ Electrolyte with Improved Bulk and Interfacial Conductivity. *J. Power Sources* **2019**, *412*, 29−36.
(39) Yu, C.; Ganapathy, S.; van Eck, E. R. H.; van Eijck, L.; Basak, S.; Liu, Y. Y.; Zhang, L.; Zandbergen, H. W.; Wagemaker, M. Revealing the Relation between the Structure, Li-Ion Conductivity and Solid-State Battery Performance of the Argyrodite Li_6PS_5Br Solid Electrolyte. *J. Mater. Chem. A* **2017**, *5*, 21178−21188.
(40) Yu, C.; van Eijck, L.; Ganapathy, S.; Wagemaker, M. Synthesis, structure and electrochemical performance of the argyrodite Li_6PS_5Cl solid electrolyte for Li-ion solid state batteries. *Electrochim. Acta* **2016**, *215*, 93−99.
(41) Kraft, M. A.; Ohno, S.; Zinkevich, T.; Koerver, R.; Culver, S. P.; Fuchs, T.; Senyshyn, A.; Indris, S.; Morgan, B. J.; Zeier, W. G. Inducing High Ionic Conductivity in the Lithium Superionic Argyrodites $Li_{6+x}P_{1-x}Ge_xS_5I$ for All-Solid-State Batteries. *J. Am. Chem. Soc.* **2018**, *140*, 16330−16339.
(42) Kraft, M. A.; Culver, S. P.; Calderon, M.; Böcher, F.; Krauskopf, T.; Senyshyn, A.; Dietrich, C.; Zevalkink, A.; Janek, J.; Zeier, W. G. Influence of Lattice Polarizability on the Ionic Conductivity in the Lithium Superionic Argyrodites Li_6PS_5X (X = Cl, Br, I). *J. Am. Chem. Soc.* **2017**, *139*, 10909−10918.
(43) Gautam, A.; Sadowski, M.; Prinz, N.; Eickhoff, H.; Minafra, N.; Ghidiu, M.; Culver, S. P.; Albe, K.; Fässler, T. F.; Zobel, M.; Zeier, W. G. Rapid Crystallization and Kinetic Freezing of Site-Disorder in the Lithium Superionic Argyrodite Li_6PS_5Br. *Chem. Mater.* **2019**, *31*, 10178−10185.
(44) Hanghofer, I.; Gadermaier, B.; Wilkening, H. M. R. Fast Rotational Dynamics in Argyrodite-Type Li_6PS_5X (X: Cl, Br, I) as Seen by ^{31}P Nuclear Magnetic Relaxation — On Cation−Anion Coupled Transport in Thiophosphates. *Chem. Mater.* **2019**, *31*, 4591−4597.
(45) Boulineau, S.; Courty, M.; Tarascon, J. M.; Viallet, V. Mechanochemical synthesis of Li-argyrodite Li_6PS_5X (X = Cl, Br, I) as sulfur-based solid electrolytes for all solid state batteries application. *Solid State Ionics* **2012**, *221*, 1−5.
(46) Hanghofer, I.; Brinek, M.; Eisbacher, S.; Bitschnau, B.; Volck, M.; Hennige, V.; Hanzu, I.; Rettenwander, D.; Wilkening, M. Substitutional Disorder: Structure and Ion Dynamics of the Argyrodites Li_6PS_5Cl, Li_6PS_5Br and Li_6PS_5I. *Phys. Chem. Chem. Phys.* **2019**, *21*, 8489−8507.
(47) Pecher, O.; Kong, S. T.; Goebel, T.; Nickel, V.; Weichert, K.; Reiner, C.; Deiseroth, H. J.; Maier, J.; Haarmann, F.; Zahn, D. Atomistic Characterisation of Li^+ Mobility and Conductivity in $Li_{7-x}PS_{6-x}I_x$ Argyrodites from Molecular Dynamics Simulations, Solid-State NMR, and Impedance Spectroscopy. *Chem. Eur. J.* **2010**, *16*, 8347−8354.
(48) Deiseroth, H. J.; Maier, J.; Weichert, K.; Nickel, V.; Kong, S. T.; Reiner, C. Li_7PS_6 and Li_6PS_5X (X: Cl, Br, I): Possible Three-dimensional Diffusion Pathways for Lithium Ions and Temperature Dependence of the Ionic Conductivity by Impedance Measurements. *Z. Anorg. Allg. Chem.* **2011**, *637*, 1287−1294.
(49) Rao, R. P.; Adams, S. Studies of lithium argyrodite solid electrolytes for all-solid-state batteries. *Phys. Status Solidi A* **2011**, *208*, 1804−1807.
(50) Mercier, R.; Malugani, J. P.; Fahys, B.; Robert, G. Superionic Conduction in Li_2S-P_2S_5-LiI-Glasses. *Solid State Ionics* **1981**, *5*, 663−666.

https://dx.doi.org/10.1021/acs.chemmater.0c01367
Chem. Mater. XXXX, XXX, XXX−XXX

(51) Ujiie, S.; Hayashi, A.; Tatsumisago, M. Structure, ionic conductivity and electrochemical stability of Li_2S-P_2S_5-LiI glass and glass−ceramic electrolytes. *Solid State Ionics* **2012**, *211*, 42−45.
(52) Malugani, J. P.; Robert, G. Preparation and electrical properties of the $0.37Li_2S$-$0.18P_2S_5$-0.45LiI glass. *Solid State Ionics* **1980**, *1*, 519−523.
(53) Hayashi, A.; Hama, S.; Minami, T.; Tatsumisago, M. Formation of superionic crystals from mechanically milled Li_2S-P_2S_5 glasses. *Electrochem. Commun.* **2003**, *5*, 111−114.
(54) Hayashi, A.; Hama, S.; Morimoto, H.; Tatsumisago, M.; Minami, T. Preparation of Li_2S-P_2S_5 amorphous solid electrolytes by mechanical milling. *J. Am. Ceram. Soc.* **2001**, *84*, 477−479.
(55) Rangasamy, E.; Liu, Z. C.; Gobet, M.; Pilar, K.; Sahu, G.; Zhou, W.; Wu, H.; Greenbaum, S.; Liang, C. D. An Iodide-Based $Li_7P_2S_8I$ Superionic Conductor. *J. Am. Chem. Soc.* **2015**, *137*, 1384−1387.
(56) Phuc, N. H. H.; Yamamoto, T.; Muto, H.; Matsuda, A. Fast synthesis of Li_2S-P_2S_5-LiI solid electrolyte precursors. *Inorg. Chem. Front.* **2017**, *4*, 1660−1664.
(57) Epp, V.; Gün, O.; Deiseroth, H. J.; Wilkening, M. Highly Mobile Ions: Low-Temperature NMR Directly Probes Extremely Fast Li^+ Hopping in Argyrodite-Type Li_6PS_5Br. *J. Phys. Chem. Lett.* **2013**, *4*, 2118−2123.
(58) Adeli, P.; Bazak, J. D.; Park, K. H.; Kochetkov, I.; Huq, A.; Goward, G. R.; Nazar, L. F. Boosting Solid-State Diffusivity and Conductivity in Lithium Superionic Argyrodites by Halide Substitution. *Angew. Chem., Int. Ed.* **2019**, *58*, 8681−8686.
(59) Jung, W. D.; Kim, J. S.; Choi, S.; Kim, S.; Jeon, M.; Jung, H. G.; Chung, K. Y.; Lee, J. H.; Kim, B. K.; Lee, J. H.; Kim, H. Superionic Halogen-Rich Li-Argyrodites Using In Situ Nanocrystal Nucleation and Rapid Crystal Growth. *Nano Lett.* **2020**, *20*, 2303−2309.
(60) Yu, C.; Li, Y.; Willans, M.; Zhao, Y.; Adair, K. R.; Zhao, F.; Li, W.; Deng, S.; Liang, J.; Banis, M. N.; Li, R.; Huang, H.; Zhang, L.; Yang, R.; Lu, S.; Huang, Y.; Sun, X. Superionic conductivity in lithium argyrodite solid-state electrolyte by controlled Cl-doping. *Nano Energy* **2020**, *69*, No. 104396.
(61) Wang, P.; Liu, H.; Patel, S.; Feng, X.; Chien, P.-H.; Wang, Y.; Hu, Y.-Y. Fast Ion Conduction and Its Origin in $Li_{6-x}PS_{5-x}Br_{1+x}$. *Chem. Mater.* **2020**, *32*, 3833−3840.
(62) Ohno, S.; Bernges, T.; Buchheim, J.; Duchardt, M.; Hatz, A.-K.; Kraft, M. A.; Kwak, H.; Santhosha, A. L.; Liu, Z.; Minafra, N.; Tsuji, F.; Sakuda, A.; Schlem, R.; Xiong, S.; Zhang, Z.; Adelhelm, P.; Chen, H.; Hayashi, A.; Jung, Y. S.; Lotsch, B. V.; Roling, B.; Vargas-Barbosa, N. M.; Zeier, W. G. How Certain Are the Reported Ionic Conductivities of Thiophosphate-Based Solid Electrolytes? An Interlaboratory Study. *ACS Energy Lett.* **2020**, *5*, 910−915.
(63) Boulineau, S.; Tarascon, J. M.; Leriche, J. B.; Viallet, V. Electrochemical properties of all-solid-state lithium secondary batteries using Li-argyrodite Li_6PS_5Cl as solid electrolyte. *Solid State Ionics* **2013**, *242*, 45−48.
(64) Ohno, S.; Helm, B.; Fuchs, T.; Dewald, G.; Kraft, M. A.; Culver, S. P.; Senyshyn, A.; Zeier, W. G. Further Evidence for Energy Landscape Flattening in the Superionic Argyrodites $Li_{6+x}P_{1-x}M_xS_5I$ (M = Si, Ge, Sn). *Chem. Mater.* **2019**, *31*, 4936−4944.
(65) Schlem, R.; Ghidiu, M.; Culver, S. P.; Hansen, A.-L.; Zeier, W. G. Changing the Static and Dynamic Lattice Effects for the Improvement of the Ionic Transport Properties within the Argyrodite $Li_6PS_{5-x}Se_xI$. *ACS Appl. Energy Mater.* **2020**, *3*, 9−18.
(66) Song, Y. B.; Kim, D. H.; Kwak, H.; Han, D.; Kang, S.; Lee, J. H.; Bak, S.-M.; Nam, K.-W.; Lee, H.-W.; Jung, Y. S. Tailoring Solution-Processable Li Argyrodites $Li_{6+x}P_{1-x}M_xS5I$ (M = Ge, Sn) and Their Microstructural Evolution Revealed by Cryo-TEM for All-Solid-State Batteries. *Nano Lett.*2020, in press. DOI: 10.1021/acs.nanolett.0c01028.
(67) de Klerk, N. J. J.; Roslon, T.; Wagemaker, M. Diffusion Mechanism of Li Argyrodite Solid Electrolytes for Li-Ion Batteries and Prediction of Optimized Halogen Doping: The Effect of Li Vacancies, Halogens, and Halogen Disorder. *Chem. Mater.* **2016**, *28*, 7955−7963.
(68) Preishuber-Pflügl, F.; Bottke, P.; Pregartner, V.; Bitschnau, B.; Wilkening, M. Correlated fluorine diffusion and ionic conduction in the nanocrystalline F^- solid electrolyte $Ba_{0.6}La_{0.4}F_{2.4}$ - ^{19}F $T_{1\rho}$ NMR relaxation vs. conductivity measurements. *Phys. Chem. Chem. Phys.* **2014**, *16*, 9580−9590.
(69) Wilkening, M.; Heitjans, P. From Micro to Macro: Access to Long-Range Li^+ Diffusion Parameters in Solids via Microscopic ^6Li, ^7Li Spin-Alignment Echo NMR Spectroscopy. *Chem. Phys. Chem.* **2012**, *13*, 53−65.
(70) Heitjans, P.; Masoud, M.; Feldhoff, A.; Wilkening, M. NMR and Impedance Studies of Nanocrystalline and Amorphous Ion Conductors: Lithium Niobate as a Model System. *Faraday Discuss.* **2007**, *134*, 67−82.
(71) Wohlmuth, D.; Epp, V.; Stanje, B.; Welsch, A. M.; Behrens, H.; Wilkening, M. High-energy mechanical treatment boosts ion transport in nanocrystalline $Li_2B_4O_7$. *J. Am. Ceram. Soc.* **2016**, *99*, 1687−1693.
(72) Wohlmuth, D.; Epp, V.; Bottke, P.; Hanzu, I.; Bitschnau, B.; Letofsky-Papst, I.; Kriechbaum, M.; Amenitsch, H.; Hofer, F.; Wilkening, M. Order vs. Disorder − A Huge Increase in Ionic Conductivity of Nanocrystalline $LiAlO_2$ Embedded in an Amorphous-Like Matrix of Lithium Aluminate. *J. Mater. Chem. A* **2014**, *2*, 20295−20306.
(73) Wilkening, M.; Epp, V.; Feldhoff, A.; Heitjans, P. Tuning the Li Diffusivity of Poor Ionic Conductors by Mechanical Treatment: High Li Conductivity of Strongly Defective $LiTaO_3$ Nanoparticles. *J. Phys. Chem. C* **2008**, *112*, 9291−9300.
(74) Preishuber-Pflügl, F.; Wilkening, M. Evidence of low dimensional ion transport in mechanosynthesized nanocrystalline $BaMgF_4$. *Dalton. Trans.* **2014**, *43*, 9901−9908.
(75) Indris, S.; Bork, D.; Heitjans, P. Nanocrystalline Oxide Ceramics Prepared by High-Energy Ball Milling. *J. Mater. Synth. Process.* **2000**, *8*, 245−250.
(76) Patterson, A. L. The Scherrer Formula for X-Ray Particle Size Determination. *Phys. Rev.* **1939**, *56*, 978−982.
(77) Prutsch, D.; Breuer, S.; Uitz, M.; Bottke, P.; Langer, J.; Lunghammer, S.; Philipp, M.; Posch, P.; Pregartner, V.; Stanje, B.; Dunst, A.; Wohlmuth, D.; Brandstatter, H.; Schmidt, W.; Epp, V.; Chadwick, A.; Hanzu, I.; Wilkening, M. Nanostructured Ceramics: Ionic Transport and Electrochemical Activity A Short Journey Across Various Families of Materials. *Z. Phys. Chem.* **2017**, *231*, 1361−1405.
(78) Düvel, A.; Wilkening, M.; Uecker, R.; Wegner, S.; Šepelák, V.; Heitjans, P. Mechanosynthesized Nanocrystalline $BaLiF_3$: The Impact of Grain Boundaries and Structural Disorder on Ionic Transport. *Phys. Chem. Chem. Phys.* **2010**, *12*, 11251−11262.
(79) Ruprecht, B.; Wilkening, M.; Feldhoff, A.; Steuernagel, S.; Heitjans, P. High anion conductivity in a ternary non-equilibrium phase of BaF_2 and CaF_2 with mixed cations. *Phys. Chem. Chem. Phys.* **2009**, *11*, 3071−3081.
(80) Ruprecht, B.; Wilkening, M.; Steuernagel, S.; Heitjans, P. Anion diffusivity in highly conductive nanocrystalline BaF_2:CaF_2 composites prepared by high-energy ball milling. *J. Mater. Chem.* **2008**, *18*, 5412−5416.
(81) Heitjans, P.; Indris, S. Diffusion and Ionic Conduction in Nanocrystalline Ceramics. *J. Phys.: Condes. Matter* **2003**, *15*, R1257−R1289.
(82) Heitjans, P.; Wilkening, M. Ion dynamics at interfaces: nuclear magnetic resonance studies. *MRS Bull.* **2009**, *34*, 915−922.
(83) Heitjans, P.; Tobschall, E.; Wilkening, M. Ion Transport and Diffusion in Nanocrystalline and Glassy Ceramics. *Eur. Phys. J.: Spec. Top.* **2008**, *161*, 97−108.
(84) Wilkening, M.; Indris, S.; Heitjans, P. Heterogeneous Lithium Diffusion in Nanocrystalline Li_2O Al_2O_3 Composites. *Phys. Chem. Chem. Phys.* **2003**, *5*, 2225−2231.
(85) Wilkening, M.; Bork, D.; Indris, S.; Heitjans, P. Diffusion in Amorphous $LiNbO_3$ Studied by ^7Li NMR: Comparison with the Nano- and Microcrystalline Material. *Phys. Chem. Chem. Phys.* **2002**, *4*, 3246−3251.

https://dx.doi.org/10.1021/acs.chemmater.0c01367
Chem. Mater. XXXX, XXX, XXX−XXX

(86) Breuer, S.; Uitz, M.; Wilkening, H. M. R. Rapid Li Ion Dynamics in the Interfacial Regions of Nanocrystalline Solids. *J. Phys. Chem. Lett.* **2018**, *9*, 2093−2097.
(87) Indris, S.; Heitjans, P.; Roman, H. E.; Bunde, A. Nanocrystalline versus Microcrystalline $Li_2O:B_2O_3$ Composites: Anomalous Ionic Conductivities and Percolation Theory. *Phys. Rev. Lett.* **2000**, *84*, 2889−2892.
(88) Dunst, A.; Epp, V.; Hanzu, I.; Freunberger, S. A.; Wilkening, M. Short-Range Li Diffusion vs. Long-Range Ionic Conduction in Nanocrystalline Lithium Peroxide Li_2O_2 − the Discharge Product in Lithium-Air Batteries. *Energy. Environ. Sci.* **2014**, *7*, 2739−2752.
(89) Breuer, S.; Pregartner, V.; Lunghammer, S.; Wilkening, H. M. R. Dispersed Solid Conductors: Fast Interfacial Li-Ion Dynamics in Nanostructured LiF and LiF:γ-Al_2O_3 Composites. *J. Phys. Chem. C* **2019**, *123*, 5222−5230.
(90) Indris, S.; Heitjans, P.; Ulrich, M.; Bunde, A. AC and DC Conductivity in Nano- and Microcrystalline $Li_2O:B_2O_3$ Composites: Experimental Results and Theoretical Models. *Z. Phys. Chem.* **2005**, *219*, 89−103.
(91) Indris, S.; Heitjans, P. Heterogeneous ^{7}Li NMR Relaxation in Nanocrystalline $Li_2O:B_2O_3$ Composites. *J. Non-Cryst. Solids* **2002**, *307*−*310*, 555−564.
(92) Maier, J. Pushing Nanoionics to the Limits: Charge Carrier Chemistry in Extremely Small Systems. *Chem. Mater.* **2014**, *26*, 348−360.
(93) Maier, J. Nanoionics: Ionic Charge Carriers in Small Systems. *Phys. Chem. Chem. Phys.* **2009**, *11*, 3011−3022.
(94) Maier, J. Nano-Ionics: Trivial and Non-Trivial Size Effects on Ion Conduction in Solids. *Z. Phys. Chem.* **2003**, *217*, 415−436.
(95) Maier, J. Ionic Conduction in Space Charge Regions. *Prog. Solid State Chem.* **1995**, *23*, 171−263.
(96) Maier, J. Space-Charge Regions in Solid 2-Phase Systems and Their Conduction Contribution − Conductance Enhancement in the System Ionic Conductor-Inert Phase and Application on AgCl-Al_2O_3 and AgCl-SiO_2. *J. Phys. Chem. Solids* **1985**, *46*, 309−320.
(97) Sata, N.; Eberman, K.; Eberl, K.; Maier, J. Mesoscopic Fast Ion Conduction in Nanometre-Scale Planar Heterostructures. *Nature* **2000**, *408*, 946−949.
(98) Gadermaier, B.; Stanje, B.; Wilkening, A.; Hanzu, I.; Heitjans, P.; Wilkening, H. M. R. Glass in Two Forms: Heterogeneous Electrical Relaxation in Nanoglassy Petalite. *J. Phys. Chem. C* **2019**, *123*, 10153−10162.
(99) Šepelák, V.; Düvel, A.; Wilkening, M.; Becker, K. D.; Heitjans, P. Mechanochemical Reactions and Syntheses of Oxides. *Chem. Soc. Rev.* **2013**, *42*, 7507−7520.
(100) Wilkening, M.; Düvel, A.; Preishuber-Pflügl, F.; da Silva, K.; Breuer, S.; Šepelák, V.; Heitjans, P. Structure and Ion Dynamics of Mechanosynthesized Oxides and Fluorides. *Z. Kristallogr. - Cryst. Mater.* **2017**, *232*, 107−127.
(101) Preishuber-Pflügl, F.; Wilkening, M. Mechanochemically Synthesized Fluorides: Local Structures and Ion transport. *Dalton Trans.* **2016**, *45*, 8675−8687.
(102) Breuer, S.; Wilkening, M. Mismatch in Cation Size Causes Rapid Anion Dynamics in Solid Electrolytes: The Role of the Arrhenius Pre-Factor. *Dalton. Trans.* **2018**, *47*, 4105−4117.
(103) Funke, K. Jump relaxation in solid electrolytes. *Prog. Solid State Chem.* **1993**, *22*, 111−195.
(104) Jonscher, A. K. Universal dielectric response. *Nature* **1977**, *267*, 673−679.
(105) Sidebottom, D. L. Dimensionality dependence of the conductivity dispersion in ionic materials. *Phys. Rev. Lett.* **1999**, *83*, 983−986.
(106) Banhatti, R. D.; Laughman, D.; Badr, L.; Funke, K. Nearly Constant Loss Effect in Sodium Borate and Silver Meta-phosphate Glasses: New Insights. *Solid State Ionics* **2011**, *192*, 70−75.
(107) Laughman, D. M.; Banhatti, R. D.; Funke, K. New Nearly Constant Loss Feature Detected in Glass at Low Temperatures. *Phys. Chem. Chem. Phys.* **2010**, *12*, 14102−14108.
(108) Laughman, D. M.; Banhatti, R. D.; Funke, K. Nearly Constant Loss Effects in Borate Glasses. *Phys. Chem. Chem. Phys.* **2009**, *11*, 3158−3167.
(109) Macdonald, J. R. Nearly Constant Loss or Constant Loss in Ionically Conducting Glasses: A Physically Realizable Approach. *J. Chem. Phys.* **2001**, *115*, 6192−6199.
(110) Funke, K.; Ross, I.; Banhatti, R. D. Nearly constant loss behavior in γ-$RbAg_4I_5$: microwave conductivity plateau identified. *Solid State Ionics* **2004**, *175*, 819−822.
(111) Funke, K.; Kloidt, T.; Wilmer, D.; Carlile, C. J. Jump Relaxation in $RbAg_4I_5$ by Dynamic Conductivity and Quasi-Elastic Neutron-Scattering. *Solid State Ionics* **1992**, *53*−*56*, 947−954.
(112) Irvine, J. T. S.; Sinclair, D. C.; West, A. R. Electroceramics: Characterization by Impedance Spectroscopy. *Adv. Mater.* **1990**, *2*, 132−138.
(113) Ruprecht, B.; Billetter, H.; Ruschewitz, U.; Wilkening, M. Ultra-slow Li ion dynamics in Li_2C_2 − on the similarities of results from ^{7}Li spin-alignment echo NMR and impedance spectroscopy. *J. Phys.: Condes. Matter* **2010**, *22*, No. 245901.
(114) Harm, S.; Hatz, A. K.; Moudrakovski, I.; Eger, R.; Kuhn, A.; Hoch, C.; Lotsch, B. V. Lesson Learned from NMR: Characterization and Ionic Conductivity of LGPS-like Li_7SiPS_8. *Chem. Mater.* **2019**, *31*, 1280−1288.
(115) Gombotz, M.; Lunghammer, S.; Breuer, S.; Hanzu, I.; Preishuber-Pflugl, F.; Wilkening, H. M. R. Spatial confinement − rapid 2D F^- diffusion in micro- and nanocrystalline $RbSn_2F_5$. *Phys. Chem. Chem. Phys.* **2019**, *21*, 1872−1883.
(116) Wohlmuth, D.; Epp, V.; Wilkening, M. Fast Li ion dynamics in the solid electrolyte $Li_7P_3S_{11}$ as probed by ^{6,7}Li NMR spin-lattice relaxation. *Chem. Phys. Chem.* **2015**, *16*, 2582−2593.
(117) Epp, V.; Gün, O.; Deiseroth, H. J.; Wilkening, M. Long-Range Li^+ Dynamics in the Lithium Argyrodite Li_7PSe_6 as Probed by Rotating-Frame Spin-Lattice Relaxation NMR. *Phys. Chem. Chem. Phys.* **2013**, *15*, 7123−7132.
(118) Wilkening, M.; Heitjans, P. Li jump process in *h*-$Li_{0.7}TiS_2$ studied by two-time ^{7}Li spin-alignment echo NMR and comparison with results on two-dimensional diffusion from nuclear magnetic relaxation. *Phys. Rev. B* **2008**, *77*, No. 024311.
(119) Kuhn, A.; Narayanan, S.; Spencer, L.; Goward, G.; Thangadurai, V.; Wilkening, M. Li Self-Diffusion in Garnet-Type $Li_7La_3Zr_2O_{12}$ as Probed Directly by Diffusion-Induced ^{7}Li Spin-Lattice Relaxation NMR Spectroscopy. *Phys. Rev. B* **2011**, *83*, No. 094302.
(120) Bork, D.; Heitjans, P. NMR relaxation study of ion dynamics in nanocrystalline and polycrystalline $LiNbO_3$. *J. Phys. Chem. B* **1998**, *102*, 7303−7306.
(121) Meyer, M.; Maass, P.; Bunde, A. Spin-lattice relaxation - non-Bloembergen-Purcell-Pound behavior by structural disorder and Coulomb interactions. *Phys. Rev. Lett.* **1993**, *71*, 573−576.
(122) Maass, P.; Meyer, M.; Bunde, A. Non-standard relaxation behavior in ionically conducting materials. *Phys. Rev. B* **1995**, *51*, 8164−8177.
(123) Bunde, A.; Maass, P.; Meyer, M. NMR relaxation in disordered systems. *Phys. A* **1992**, *191*, 433−437.

https://dx.doi.org/10.1021/acs.chemmater.0c01367
Chem. Mater. XXXX, XXX, XXX−XXX

3.2 Structural Disorder in Li_6PS_5I Speeds ^7Li Nuclear Spin Recovery and Slows Down ^{31}P Relaxation – Implications for Translational and Rotational Jumps as Seen by Nuclear Magnetic Resonance

The experimental results summarized in the following publication involve high-energy ball milled Li_6PS_5I as used for the experiments in section 3.1. ^7Li and ^{31}P NMR were performed to probe ion dynamics in nanocrystalline Li_6PS_5I. Microcrystalline Li_6PS_5I is a poor ionic conductor lacking long-range Li^+ transport mechanisms. In contrast, nanocrystalline Li_6PS_5I shows enhanced ionic conductivity, which can presumably be attributed to the ionic site disorders and polyhedral distortions. The experimental results of the ^7Li spin-relaxation measurements support this theory, as extremely fast processes were detected, that were missing in the pristine samples. Hanghofer *et al.* already conducted ^{31}P nuclear magnetic relaxation measurements on chloride, bromide and iodide thiophosphates. They succeeded in showing that PS_4^{3-} rotational motions are much faster than Li^+-translation in Li_6PS_5I and therefore, uncoupled.[43] In the following publication ^{31}P NMR spin-lattice relaxation measurements were used to probe PS_4^{3-} rotational jump processes that may influence Li^+ translational dynamics. ^{31}P NMR revealed that those PS_4^{3-} rotations are to a great extent influenced by the structural changes introduced by the soft-mechanical treatment. Slowed down PS_4^{3-} rotations are in resonance with Li^+-translation. Thus, understanding the influence of disorder on ion dynamics is crucial for the successful mechanochemical synthesis of highly conducting electrolytes. Li_6PS_5I is a great model substance to demonstrate the value of such investigations.

Structural Disorder in Li_6PS_5I Speeds ^{7}Li Nuclear Spin Recovery and Slows Down ^{31}P Relaxation–Implications for Translational and Rotational Jumps as Seen by Nuclear Magnetic Resonance

M. Brinek, C. Hiebl, K. Hogrefe, I. Hanghofer, and H. M. R. Wilkening

The Journal of Physical Chemistry C **2020** *124* (42), 22934-22940

THE JOURNAL OF PHYSICAL CHEMISTRY C

pubs.acs.org/JPCC

Article

Structural Disorder in Li_6PS_5I Speeds ^7Li Nuclear Spin Recovery and Slows Down ^{31}P Relaxation—Implications for Translational and Rotational Jumps as Seen by Nuclear Magnetic Resonance

M. Brinek, C. Hiebl, K. Hogrefe, I. Hanghofer, and H. M. R. Wilkening*

Cite This: https://dx.doi.org/10.1021/acs.jpcc.0c06090

Read Online

ACCESS | Metrics & More | Article Recommendations | Supporting Information

ABSTRACT: Lithium-thiophosphates have attracted great attention as they offer a rich playground to develop tailor-made solid electrolytes for clean energy storage systems. Here, we used poorly conducting Li_6PS_5I, which can be converted into a fast ion conductor by high-energy ball-milling to understand the fundamental guidelines that enable the Li^+ ions to quickly diffuse through a polarizable but distorted matrix. In stark contrast to well-crystalline Li_6PS_5I (10^{-6} S cm^{-1}), the ionic conductivity of its defect-rich nanostructured analog touches almost the mS cm^{-1} regime. Most likely, this immense enhancement originates from site disorder and polyhedral distortions introduced during mechanical treatment. We used the spin probes ^7Li and ^{31}P to monitor nuclear spin relaxation that is directly induced by Li^+ translational and/or PS_4^{3-} rotational motions. Compared to the ordered form, ^7Li spin–lattice relaxation (SLR) in nano-Li_6PS_5I reveals an additional ultrafast process that is governed by activation energy as low as 160 meV. Presumably, this new relaxation peak, appearing at T_{max} = 281 K, reflects extremely rapid Li hopping processes with a jump rate in the order of 10^9 s^{-1} at T_{max}. Thus, the thiophosphate transforms from a poor electrolyte with island-like local diffusivity to a fast ion conductor with 3D cross-linked diffusion routes enabling long-range transport. On the other hand, the original ^{31}P nuclear magnetic resonance (NMR) SLR rate peak, pointing to an effective ^{31}P-^{31}P spin relaxation source in ordered Li_6PS_5I, is either absent for the distorted form or shifts toward much higher temperatures. Assuming the ^{31}P NMR peak as being a result of PS_4^{3-} rotational jump processes, NMR unveils that disorder significantly slows down anion dynamics. The latter finding might also have broader implications and sheds light on the vital question how rotational dynamics are to be manipulated to effectively enhance Li^+ cation transport.

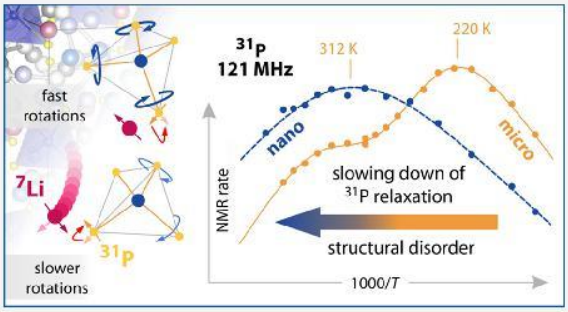

INTRODUCTION

The enigmatic interplay between cation translational processes and rotational dynamics of complex anions[1−3] propelled the (re-)investigation of a range of Li-containing and Na-bearing thiophosphates.[4−7] The interest in fast ionic conductors[8] is spurred by the demand to develop high-performance energy storage systems relying on ceramic electrolytes.[9] Early examples for which the so-called "paddlewheel"[1−3] (or "cogwheel" or "revolving door")[10] mechanism is used to describe the cation−anion coupled transport, include the rotator phases Li_2SO_4,[1−3,11−14] $LiMSO_4$ (M = Na and Ag),[3,15,16] Na_3PO_4,[1,14] and several borohydrides[17−21] and a range of *closo*-boranes,[22−28] including the dynamics of cluster ions in $Li_3S(BF_4)_{0.5}Cl_{0.5}$ and Na_3OBH_4.[29−31] As is impressively seen for the low-T modification orthorhombic $LiBH_4$, ^7Li and ^{11}B (and even ^1H) nuclear magnetic resonance (NMR) is suited to directly probe local BH_4^- rotational motions in the borohydride.[32−35]

In its narrower sense, the paddlewheel mechanism[1,8,36] explains rapid cation translational dynamics by opening (or even closing) low-energy passageways through rotational (or librational) jumps of the polyanions that form the polarizable matrix of the electrolyte.[1] The cog-wheel mechanism requires significant dynamic coupling of neighboring anions, whereas the revolving door mechanism suggests that the anion reacts with an evasive motion to let the cation pass by.[1] Hence, it is still unclear which of the teammates act as the driving force.[7] Also, uncoupled fast rotational motions have been proposed to increase cation mobility through the generation of Coulombic fluctuations to affect the cation attempt frequencies.[1] The validity of such mechanisms has also been questioned in the past as the larger free transport volume for the rotational phases might play a role too;[3,10] conversely, an increase in lattice volume, e.g., also by the introduction of larger lattice units, will facilitate anion rotation.

Received: July 3, 2020
Revised: September 18, 2020
Published: September 29, 2020

From an experimental point of view, it is striking that the onset of rotational disorder seen in the high-temperature modifications of the sulfate or phosphate compounds[1] is accompanied by an increase in cation diffusivity and a decrease in activation energy.[1,10] Such a relationship, which may be regarded as a design tool to develop tailor-made, fast Li^+ ion conductors, has also been proposed by Adams and Rao[37] to explain the overall dynamic situation in the famous ion conductor $Li_{10}GeP_2S_{11}$.[38] Quite recently, Nazar and co-workers have used the paddlewheel concept to explain enhanced Na^+-ion transport in $Na_{11}Sn_2PS_{12}$ and provided supporting evidence for this cooperative interplay in β-Li_3PS_4 as well as its Si-substituted analog $Li_{3.25}Si_{0.25}P_{0.75}S_4$.[5,39] As the latter materials are expected to play decisive roles in all-solid-state batteries equipped with polycrystalline electrolytes or glassy compounds,[9,40,41] a deeper understanding of the dynamic processes from an atomic-scale point of view is desirable. Quite recently, Smith and Siegel have used ab initio molecular dynamics simulations to characterize translational-rotational coupling in glassy $25Li_2S$-$75P_2S_5$.[4] Their recent study[4] and the timeless report of Jansen[1] include precise and very helpful introductions into the topic, we recommend reading.

In our own group, we interpreted the low-temperature ^{31}P NMR response in coarse-grained Li_6PS_5I as a signature of fast PS_4^{3-} rotational jump processes.[7] In contrast to site-disordered Li_6PS_5Br and Li_6PS_5Cl, in the iodine compound with its expanded volume and ordered sublattices,[42−45] containing also polarizable I anions, the PS_4^{3-} units seem to be able to freely perform rotational (and librational) dynamics. At least for Li_6PS_5I, this uncoupled rotational motion, even if generating periodically fluctuating electric potentials at the cation sites,[1] does not favor long-range Li^+ transport.[46] Interestingly, site disorder and lattice contraction clearly disturb the effectiveness of the underlying ^{31}P NMR spin−lattice relaxation processes and lead to a shift in the corresponding rate peaks toward higher temperatures when going from Li_6PS_5I to Li_6PS_5X (X = Br and Cl).[7] To underscore our hypothesis that structural disorder hampers rotational motions in Li_6PS_5X, we used Li_6PS_5I as a model substance[46] and introduced (site) disorder by *soft* high-energy ball-milling.[47] Soft milling takes advantage of a low sample-to-ball ratio in conjunction with low rotational speeds. This approach does not change the overall chemical composition of the nanocrystalline sample but leads to anion, and presumably, also to extensive cation disorder, polyhedral distortions, and strain. These structural changes were revealed by the broadening of the corresponding X-ray reflections and broadened ^{31}P (magic angle spinning, MAS) NMR spectra.[47] The dynamic features of the coarse-grained Li_6PS_5I were investigated in detail in three earlier studies[7,46,47] by our group; the present study is based on these results.

Here, we used ^{31}P NMR spin−lattice relaxation experiments to describe any possible influence of structural disorder on ^{31}P nuclear spin recovery in nanostructured Li_6PS_5I. The results were compared with those obtained for the ^7Li nucleus recently.[7,46,47] In general, the spin recovery is directly driven by the thermally activated jump processes taking place in the crystal structure of the thiophosphate. Most importantly, while Li^+ self-diffusivity is enhanced in disordered Li_6PS_5I,[47] the effective source governing ^{31}P nuclear spin relaxation in ordered Li_6PS_5I is indeed noticeably weakened in the ball-milled material. In nano-Li_6PS_5I, the distinct ^{31}P NMR spin−lattice relaxation peak is no longer seen as a separate signal; its disappearance indicates that the disorder has a drastic influence on the temporal ^{31}P-^{31}P(^7Li) magnetic interactions controlling nuclear spin recovery.

MATERIALS AND METHODS

The preparation of Li_6PS_5I is described elsewhere;[46] for the present study, we used the material of the same synthesis batch that has been recently investigated by X-ray diffraction, ^{31}P MAS NMR, and also by impedance measurements and NMR spectroscopy.[46] To prepare nanocrystalline Li_6PS_5I, 0.5 g of the starting powder was added to ZrO_2 milling vials (45 mL) under an Ar atmosphere (H_2O < 1 ppm, O_2 < 1 ppm). The milling jars were filled with 60 milling balls (5 mm in diameter). Nano-Li_6PS_5I was treated in a Premium line 7 planetary mill (Fritsch) that was operated at a rotation speed of 400 rpm.[47] The milling time was set to 120 min. For NMR measurements, the powder was sealed in Duran ampoules.

The acquisition of ^7Li (116 MHz Larmor frequency) and ^{31}P (121 MHz) NMR spin−lattice relaxation rates ($1/T_1$) was carried out using a Bruker 300-MHz NMR spectrometer; the procedures are identical to those described already elsewhere.[46] We used the well-known saturation recovery sequence to monitor the recovery of longitudinal magnetization after a comb of closely spaced 90° perturbation pulses. The curves were parametrized with appropriate exponential functions to extract the rate $1/T_1$ as a function of temperature, see the Supporting Information.

RESULTS AND DISCUSSION

Li_6PS_5I crystallizes with cubic symmetry (space group $F\bar{4}3m$, see Figure 1a).[42] The Li ions occupy various lattice sites within the structure forming Li-rich cages. While fast Li^+ exchange, with rates on the MHz rage, occurs within these cages for Li_6PS_5I, intercage jump processes are much less frequent, that is, reduced by 2−3 orders of magnitude.[48] As these processes are important to guarantee long-range ionic transport, highly crystalline Li_6PS_5I turned out to be a poor ionic conductor with an ionic conductivity in the order of 10^{-6} S cm^{-1} at room temperature.[46]

In contrast, the sibling compounds Li_6PS_5X (X = Br and Cl) benefit from both anion and cation site disorder resulting in ionic conductivities in the mS cm^{-1} range.[46,49] Hence, besides other effects such as the influence of anion polarizability, anion site disorder, i.e., the occupation of 4d sites within the Li-rich cages by X^-, and, as has been shown quite recently,[43] the partial filling of the originally empty Li^+ sites (see the 48 h and 16e voids shown in Figure 1b) guarantee rapid Li^+ exchange. In addition to strain and polyhedra distortions generated, high-energy ball-milling is, thus, also expected to sensitively affect both the I^-/S^{2-} and Li^+ site distribution in Li_6PS_5I. Indeed, as has been shown earlier, soft mechanical treatment can enhance ionic conductivity by several orders of magnitude.[47,50] The sample milled for 120 min in a planetary mill shows an ionic conductivity almost reaching the mS cm^{-1} regime at ambient conditions.[47]

To understand how mechanical treatment affects the various interactions of the ^7Li (spin quantum number I = 3/2) and ^{31}P (I = 1/2) spins, we recorded diffusion-induced $1/T_1$ NMR rates as a function of the inverse temperature. The change of variable-temperature ^7Li NMR lines, clearly pointing to faster Li^+ dynamics in nano-Li_6PS_5I, is discussed elsewhere.[47] In Figure 2, the ^{31}P (and ^7Li) NMR $1/T_1$ rates of unmilled

https://dx.doi.org/10.1021/acs.jpcc.0c06090
J. Phys. Chem. C XXXX, XXX, XXX−XXX

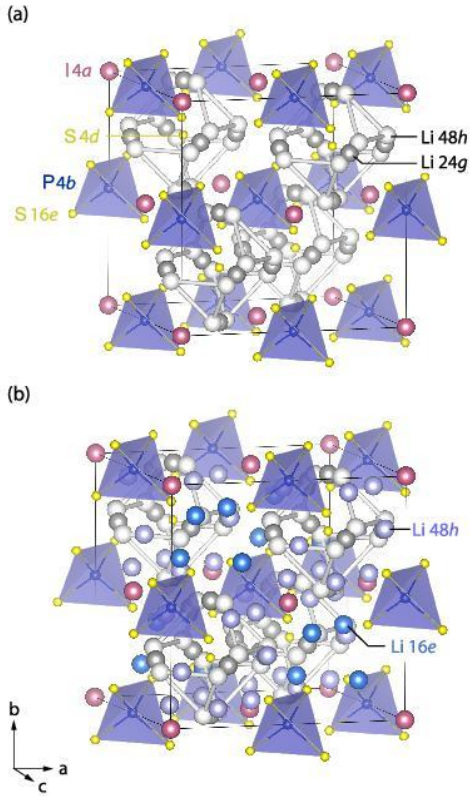

Figure 1. (a) Crystal structure of argyrodite-type Li_6PS_5I. While the I^- anions occupy the 4*a* sites, the S^{2-} anions reside on the 4*d* and 16*e* sites forming an ordered anion sublattice. PS_4^{3-} tetrahedra are shown in blue. Li^+ ions are arranged such that they build cages consisting of six 48 *h*-24 *g*-48*h*′ triplets. Intracage jumps include hopping processes between 48 *h* sites of two different triplets. Within the triplet 48 *h*-24 *g*-48*h*′, the Li ions perform highly restricted forward-backward hopping processes. (b) Long-range ion dynamics are possible either by direct jumps from cage to cage ($48h_1$-$48h_2$) or by using the interstitial sites that are illustrated by blue spheres (48 *h* and 16*e*).[43]

Li_6PS_5I are shown using an Arrhenius representation.[7] In particular, the present paper focusses on the ^{31}P NMR relaxation rates peaks (C) and (D) in Figure 2a and the corresponding one in Figure 2b. The values included correspond to the activation energies of either the low-T ($E_{a,\,high}$) and high-T flanks ($E_{a,\,high}$) of the peaks. The rates were extracted from the full magnetization transients shown in Figure S1. Here, we focus on data obtained for the cubic modification.[7] As indicated in Figure 2, below 160 K the iodide transforms into an orthorhombic phase.[46] Coming from low temperatures, the ^7Li NMR rates pass into a well-defined relaxation rate peak, which was attributed to intracage Li^+ jump processes.[46] We parameterized the peak with a modified Lorentzian-shaped spectral density function based on the relaxation model of Bloembergen, Purcell and Pound (BPP),[51,52] see the Supporting Information and Table S1 for further information. The peak turned out to be rather symmetric which is expected for 3D uncorrelated Li^+ motions.[53]

The same relaxation source, that is, the ^{31}P NMR relaxation due to the translational motion of the Li^+ ions is indirectly sensed by the ^{31}P nuclei; see peak (C) in Figure 2. In addition, the ^{31}P NMR data unveil a second, more prominent peak at T = 220 K (D), which we assume is mainly driven by the homonuclear ^{31}P-^{31}P dipole−dipole interactions. Presumably, this peak mirrors the fast PS_4^{3-} rotational motions.[7] Interestingly, both NMR peaks are governed by almost the same activation energy of $E_{a,\,high}$ = 0.20 eV (Figure 2a). The fact that the ^{31}P NMR peak (D) is not visible in ^7Li NMR could have various reasons. Heteronuclear ^{31}P-^7Li coupling, which is generally weaker than the homonuclear interactions, might be too low or the peak might be hidden in the low-temperature region shown as a dashed area in Figure 2a. In this region, the ^7Li NMR rates are increasingly dominated by the nondiffusive relaxation processes such as the coupling of the Li spins to lattice vibrations or paramagnetic impurities.

^7Li and ^{31}P NMR experiments on nano-Li_6PS_5I reveal two important differences compared to the unmilled sample. First, the prominent ^{31}P NMR rate peak seen at 220 K is absent for the nanocrystalline sample. Hence, the relaxation source is either switched off or the original peak (D) is shifted toward higher temperatures as indicated by the curved arrow in Figure 2b. This shift means that the PS_4^{3-} rotational motion is slowing down in nano-Li_6PS_5I. It also helps interpret the width of the ^{31}P NMR peak of nano-Li_6PS_5I, which now turned out to be a superposition of several rate peaks. The ^{31}P spins are sensing, including peaks (A) and (B) seen by ^7Li NMR, see below. The activation energies calculated from the flanks of the ^{31}P $1/T_1(1/T)$ peak are regarded as apparent values that do not represent a single, distinct motional process.

Second, the original ^7Li NMR response of coarse-grained, i.e., structurally ordered Li_6PS_5I, is split into two rate peaks labeled (A) and (B); these peaks appear at T_{max} = 373 K and 281 K, respectively. The shift is mainly due to a reduction in the activation energy from $E_{a,\,high}$ = 0.23 eV to $E_{a,\,high}$ = 0.16 eV. The corresponding prefactors τ_0^{-1} of the underlying Arrhenius relations, $\tau^{-1} = \tau_0^{-1} \exp(-E_{a,\,high}/k_BT)$, where k_B denotes Boltzmann's constant, turned out to be in the same order of magnitude (10^{12} s^{-1}, see Table S1); they simply differ by a factor of two. It is a fundamental question whether this "attempt frequency" τ_0^{-1} is related to a vibrational frequency experienced by the mobile ion residing in a potential well between the hops, as suggested by the simple, classical diffusion theory. Phonon frequencies usually take values from 10^{12} to 10^{14} s^{-1}; thus, the τ_0^{-1} values extracted from the NMR data lie at the lower limit of this range.

In the following, we discuss a possible scenario that explains the splitting of the ^7Li NMR peak, thereby also pointing out the differences between results from NMR relaxation and conductivity spectroscopy. In line with earlier studies,[46] we suppose that the original, almost symmetric BPP-type peak of microcrystalline Li_6PS_5I is mainly mirroring fast intracage jump processes involving the sites 24 *g* and 48 *h*. Because of its relatively larger peak amplitude compared to that of peak (B) that is determined by the underlying coupling constant, we suppose that peak (A) is also governed by stronger Li−Li interactions of the Li-rich cages. From the maximum condition, $\omega_0\tau = 1$,[54,55] with τ being the residence time and $\omega_0/2\pi$ = 116 MHz representing the Larmor frequency, we estimate that at T_{max} = 329 K, the average jump rate should be in the order of $\tau^{-1} = 7.3 \times 10^8$ s^{-1}. This value roughly translates into a self-diffusion coefficient of $D_{329\,K} = 4.86 \times 10^{-12}$ m^2s^{-1}, if we use the Einstein−Smoluchowski equation to relate τ with D according to $D = a^2/(6\tau)$.[56,57] Here, we used a jump distance of a = 2 Å as a good approximation of the average Li−Li distance. According to the Nernst−Einstein equation,[58] $D_{329\,K}$

https://dx.doi.org/10.1021/acs.jpcc.0c06090
J. Phys. Chem. C XXXX, XXX, XXX−XXX

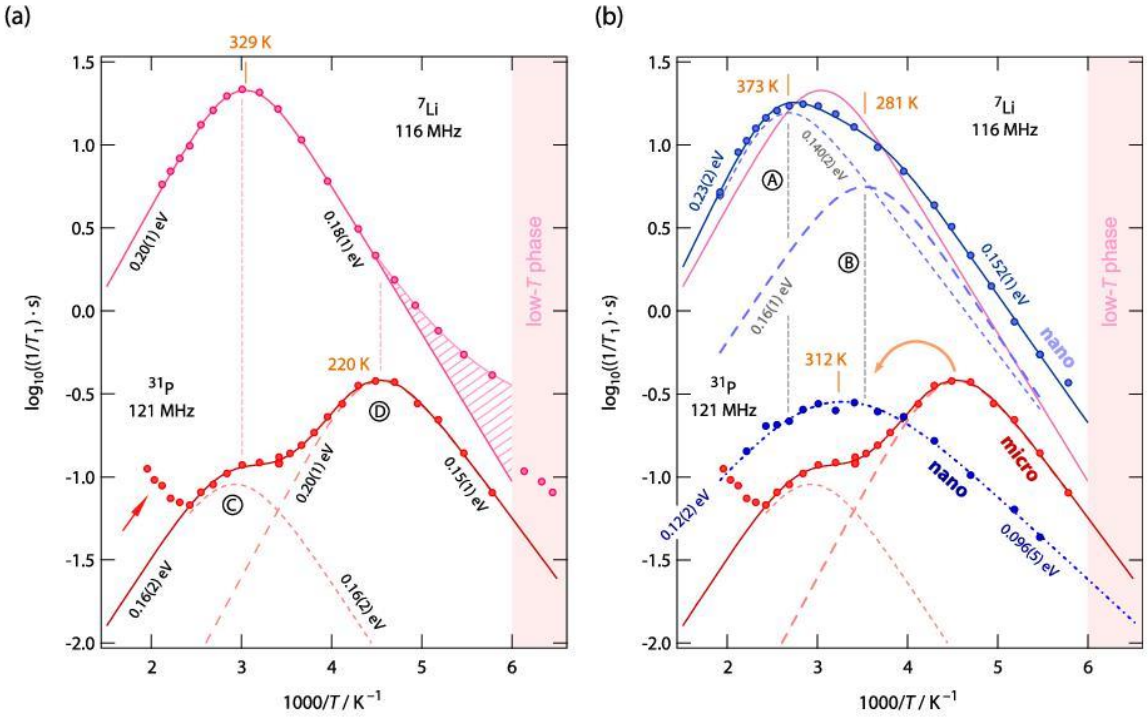

Figure 2. (a) Change of the diffusion-induced ^{7}Li (116 MHz) and ^{31}P (121 MHz) NMR spin−lattice relaxation rates $1/T_1$ of microcrystalline, that is, unmilled Li_6PS_5I. Solid lines show fits with appropriate Lorentzian-shaped BPP functions. The values indicate the activation energies of the high-temperature and low-temperature flanks, respectively. Dashed lines show individual ^{31}P NMR peaks $1/T_1(1/T)$ whose sum yield the overall ^{31}P NMR response comprising two peaks at $T > 400$ K. (b) Same data as in (a) but including the ^{7}Li and ^{31}P NMR responses of the nanocrystalline Li_6PS_5I. The ^{7}Li NMR $1/T_1(1/T)$ peak shifts toward a higher T and exhibits a shoulder located at 281 K representing extremely fast spin fluctuations sensed by the ^{7}Li nuclei. For comparison, the ^{31}P NMR rates pass through a broadened peak likely being the superposition of several relaxation processes. Most importantly, the prominent low-temperature peak seen in (a) that appeared at 220 K (peak (D)) is either absent for nanocrystalline Li_6PS_5I or has shifted toward higher T as indicated by the curved arrow. The increase in ^{31}P NMR rates at the highest temperatures, the arrow in (a), points to a third relaxation process with even longer motional residence times.

corresponds to conductivity σ in the order of 1.6 mS cm^{-1} at 329 K. This value is much too high to explain the experimental value of 10^{-6} S cm^{-1} observed at ambient conditions. Even if we take into account any deviations of the Haven ratio H_r and the correlation factor f from 1, as might be expected for correlated diffusion,[58] the difference between the solid-state diffusion coefficient D_σ, as extractable from conductivity measurements, and the self-diffusion coefficient $D = (H_r/f)\,D_\sigma$ as probed by NMR, is several orders of magnitude. Hence, we are confident that the symmetric rate peak seen at 329 K mirrors the rapid but spatially constrained ion dynamics that do not contribute to long-range ion transport that is probed by σ. This interpretation has also been underscored by ^{7}Li NMR line width measurements performed recently.[47] They reveal only a partial averaging of the Li−Li dipolar interactions[46] as the important intercage jump processes needed to fully average homonuclear broadening take place much less frequently. However, full averaging is seen at higher temperatures.[46,47]

For the ball-milled sample, this BPP-type peak that does not change much in shape ($E_{a,high}$ = 0.2 eV, see Figure 2) shifts by approximately 50 K toward higher temperatures, see peak (A). Obviously, the disorder perturbs the Li^+ dynamics associated with the Li-rich cages, as pointed out recently.[47] The Arrhenius laws belonging to the original and final peak differ in activation energy; however, the prefactors remain almost unaffected (Table S1). Hence, in contrast to macroscopic bulk electrical relaxation for which a significant change in prefactor was observed,[47] ^{7}Li NMR does not reveal a strong influence of the prefactor on this spatially restricted type of Li^+ motion.

Most importantly, a careful evaluation of the rates below 330 K reveals a second $1/T_1(1/T)$ peak, labeled (B) in Figure 2b, that is located at T_{max} = 281 K. For comparison, the corresponding and prominent ^{7}Li NMR rate peaks of the fast Li^+ ion conductor Li_6PS_5Br appear at almost the same temperature, T_{max} = 286 K. Hence, nanocrystalline Li_6PS_5I increasingly start to resemble the nuclear spin behavior of the site-disordered bromide analog. As mentioned above, neutron diffraction revealed that the Li^+ ions in Li_6PS_5Br do also populate the so far unexplored intercage voids (48 *h* sites)[43] that are empty in structurally ordered Li_6PS_5I. The interplay between the anion disorder and Li^+ charge distribution seems to play the decisive role in explaining the facile Li^+ transport observed. This finding can also be used to explain the highly asymmetric shape[46,59] of the $1/T_1$ peak of Li_6PS_5Br being produced by a superposition of elementary jump processes including localized ones and those enabling long-range ion transport. Frustration effects introduced by the anion disorder and concerted motions have been considered to explain the overall dynamic situation in Li_6PS_5X (X = Br and Cl), which also seems to be triggered by the Li-Li Coulombic interactions.[60]

Assuming that mechanical treatment forces the Li ions in Li_6PS_5I also to considerably occupy the additional sites outside the cages, we could interpret peak (B) as being controlled by

https://dx.doi.org/10.1021/acs.jpcc.0c06090
J. Phys. Chem. C XXXX, XXX, XXX−XXX

fast *inter*cage jump processes. Indeed, ^{7}Li NMR linewidth measurements unveiled that almost fully hopping-controlled dipole−dipole averaging takes place in nano-Li_6PS_5I.[47] In addition, to underpin this scenario from a quantitative point of view, we calculated the ionic conductivity expected for the T_{max} of peak (B). Anticipating that 10% of the total number of ions have access to the fast intercage jump processes yields σ_{calc} 0.19 mS cm^{-1}. This value is in good agreement with the experimental one (σ_{exp} = 0.14 mS cm^{-1}). Increasing the effective number density N^1 to 20% of the total number of available Li^+ ions per unit cell[43] increases σ_{calc} to 0.37 mS cm^{-1}. Again, the deviations of H_r and especially f from 1 will further influence σ_{calc}. In the latter case, a correlation factor of $f \approx 0.4$ will immediately result in $\sigma_{calc} = \sigma_{exp}$ at 281 K. Altogether, we found evidence that the boost in ionic conductivity seen for Li_6PS_5I is represented by the ^{7}Li NMR relaxation peak appearing at 281 K. Its presence helps explain the colossal increase in Li^+ ion dynamics when going from microcrystalline to nanocrystalline Li_6PS_5I. In addition, further dynamic processes were also probed by spin-lock ^{7}Li NMR, recently.[47] As an example, at locking frequencies in the kHz range, a spin-lock relaxation peak at a temperature as low as 190 K shows up for nano-Li_6PS_5I.[47]

In contrast to conductivity spectroscopy being sensitive to long-range ion transport, the flanks of ^{7}Li NMR relaxation rate peaks, unlike stimulated echo techniques,[61,62] capture the barriers of the elementary steps of ion hopping. In addition, in the low-T regime, the slopes of these flanks are influenced by correlation effects. Thus, the activation energies calculated from NMR, here ranging from 0.23 to 0.16 eV (Figure 2b), do not agree with the macroscopic activation energy seen by conductivity spectroscopy (0.36 eV) and electric modulus measurements (0.33 eV).[47] Such discrepancies are well known in the literature[63] and leave room for ideas that, for example, Li^+ ions have to surmount even larger barriers of a macroscopic length scale or the underlying motional correlation functions, probed by the different methods, simply differ.

Coming back to ^{31}P NMR relaxometry, we recognize that the T_{max} of the ^{7}Li $1/T_1(1/T)$ rate peak (B) agrees very well with the position of the ^{31}P NMR peak of nano-Li_6PS_5I (Figure 2b). If we assume that PS_4^{3-} rotational jumps contribute to the overall ^{31}P response, these processes take place on the same time scale as Li^+ hopping does, that is, on the ns scale (300 K). Thus, they are in resonance with Li^+ translational dynamics. This situation is in stark contrast to that discussed recently for ordered Li_6PS_5I.[7] In the structurally ordered counterpart, the translational and any rotational jump processes seem to be, at least, temporarily decoupled;[7] in unmilled Li_6PS_5I, the rotational motions are much faster than the long-range Li^+ ion dynamics. On the other hand, in disordered Li_6PS_5I, the matching characteristic motional correlation rates τ^{-1} point to dynamic cation−anion coupling that affects the overall Li^+ ion translational dynamics, possibly due to the paddle-wheel mechanism. This view is in line with that of Smith and Siegel who presented evidence that this mechanism is relevant for ion dynamics in glassy electrolytes such as $75Li_2S$-$25P_2S_5$.[4] Certainly, further spectroscopic studies in combination with calculations are needed to support our findings and to unravel the true nature of anion−cation coupling in thiophosphates. We are still at the beginning to understand this important interaction. Such a beginning resembles a dialog of Rowling: "Is this real? Or has this been happening in my head?" "Of course it is happening inside your head, Harry, but why on earth should that mean that it is not real." (J. K. Rowling, Harry Potter and the Deathly Hallows, 2007.)

CONCLUSIONS

Li_6PS_5I serves as a highly suitable model system to study the influence of the structural disorder on dynamic properties. Here, the disorder was introduced by a soft mechanical treatment. We assume that the distortions and (anion and cation) site disorders are responsible for the immense increase in the ionic conductivity of the nanocrystalline, ball-milled Li_6PS_5I. Such disorder is absent for the unmilled samples. Variable-temperature ^{31}P NMR reveals that an important source for spin−lattice relaxation is significantly changed after ball-milling. For ordered Li_6PS_5I, the prominent ^{31}P NMR relaxation peak attributed to the ultrarapid PS_4^{-3} rotational jumps either shifts toward higher T or is missing. We conclude that structural disorder in Li_6PS_5I sensitively affect such motions. Moreover, it does not only alter the ^{31}P NMR relaxation response but also reveals the subtle, but important, differences in ^{7}Li NMR relaxation. While structural disorder slow down the fast intracage Li^+ dynamics, a new rate peak emerges at 281 K pointing to the highly effective source inducing ^{7}Li NMR spin−lattice relaxation. We propose that this peak is responsible for the fast jump processes that enable the ions to diffuse over long distances. The mean activation energy for these elementary jump processes turned out to range between 150 and 160 meV. The associated translational jump rate is in the GHz range (τ^{-1}(281 K) = 7.3 × 10^8 s^{-1}) and would be *in resonance* with the mean rotational jump rate of the PS_4^{-3} polyanions.

ASSOCIATED CONTENT

Supporting Information

The Supporting Information is available free of charge at https://pubs.acs.org/doi/10.1021/acs.jpcc.0c06090.

Magnetization transients and results obtained from analyzing the relaxation rate peaks with modified BPP-type spectral density functions (PDF)

AUTHOR INFORMATION

Corresponding Author

H. M. R. Wilkening − *Institute for Chemistry and Technology of Materials, Christian Doppler Laboratory for Lithium Batteries, Graz University of Technology (NAWI Graz), 8010 Graz, Austria*; orcid.org/0000-0001-9706-4892; Email: wilkening@tugraz.at

Authors

M. Brinek − *Institute for Chemistry and Technology of Materials, Christian Doppler Laboratory for Lithium Batteries, Graz University of Technology (NAWI Graz), 8010 Graz, Austria*

C. Hiebl − *Institute for Chemistry and Technology of Materials, Christian Doppler Laboratory for Lithium Batteries, Graz University of Technology (NAWI Graz), 8010 Graz, Austria*

K. Hogrefe − *Institute for Chemistry and Technology of Materials, Christian Doppler Laboratory for Lithium Batteries, Graz University of Technology (NAWI Graz), 8010 Graz, Austria*

I. Hanghofer − *Institute for Chemistry and Technology of Materials, Christian Doppler Laboratory for Lithium Batteries,*

https://dx.doi.org/10.1021/acs.jpcc.0c06090
J. Phys. Chem. C XXXX, XXX, XXX−XXX

Graz University of Technology (NAWI Graz), 8010 Graz, Austria

Complete contact information is available at: https://pubs.acs.org/10.1021/acs.jpcc.0c06090

Author Contributions

M.B. and C.H. contributed equally to the work.

Notes

The authors declare no competing financial interest.

■ ACKNOWLEDGMENTS

Financial support by the Austrian Federal Ministry of Science, Research and Economy (BMWFW) and the National Foundation for Research, Technology and Development is gratefully acknowledged. In addition, the study received considerable funding from the European Union's Horizon 2020 research and innovation program under the grant agreement no. 769929.

■ REFERENCES

(1) Jansen, M. Volume Effect or Paddle-Wheel Mechanism - Fast Alkali-Metal Ionic-Conduction in Solids with Rotationally Disordered Complex Anions. *Angew. Chem., Inter. Ed.* **1991**, *30*, 1547−1558.

(2) Lunden, A. On the Paddle-Wheel Mechanism for Cation Conduction in Lithium Sulphate. *Z. Naturforsch. A* **1995**, *50*, 1067−1076.

(3) Karlsson, L.; Mcgreevy, R. L. Mechanisms of Ionic-Conduction in Li_2SO_4 and $LiNaSO_4$ - Paddle Wheel or Percolation. *Solid State Ionics* **1995**, *76*, 301−308.

(4) Smith, J. G.; Siegel, D. J. Low-Temperature Paddlewheel Effect in Glassy Solid Electrolytes. *Nat. Commun.* **2020**, *11*, 1483.

(5) Zhang, Z.; Roy, P.-N.; Li, H.; Avdeev, M.; Nazar, L. F. Coupled Cation−Anion Dynamics Enhances Cation Mobility in Room-Temperature Superionic Solid-State Electrolytes. *J. Am. Chem. Soc.* **2019**, *141*, 19360−19372.

(6) Famprikis, T.; et al. A New Superionic Plastic Polymorph of the Na^+ Conductor Na_3PS_4. *ACS Mater. Lett.* **2019**, *1*, 641−646.

(7) Hanghofer, I.; Gadermaier, B.; Wilkening, H. M. R. Fast Rotational Dynamics in Argyrodite-Type Li_6PS_5X (X: Cl, Br, I) as Seen by ^{31}P Nuclear Magnetic Relaxation — On Cation−Anion Coupled Transport in Thiophosphates. *Chem. Mater.* **2019**, *31*, 4591−4597.

(8) Famprikis, T.; Canepa, P.; Dawson, J. A.; Islam, M. S.; Masquelier, C. Fundamentals of Inorganic Solid-State Electrolytes for Batteries. *Nat. Mater.* **2019**, *18*, 1278−1291.

(9) Zhang, Z. Z.; et al. New Horizons for Inorganic Solid State Ion Conductors. *Energy Environ. Sci.* **2018**, *11*, 1945−1976.

(10) Lunden, A. Evidence for and Against the Paddle-Wheel Mechanism of Ion-Transport in Superionic Sulfate Phases. *Solid State Commun.* **1988**, *65*, 1237−1240.

(11) Forland, T.; Krogh-Moe, J.; Moutschen-Dahmen, M.; Noer, B.; Reio, L. The Structure of the High Temperature Modification of Lithium Sulfate. *Acta Chem. Scand.* **1957**, *11*, 565−567.

(12) Nilsson, L.; Thomas, J. O.; Tofield, B. C. The Structure of the High-Temperature Solid Electrolyte Lithium-Sulfate at 908-K. *J. Phys. C - Solid State Phys.* **1980**, *13*, 6441−6451.

(13) Mellander, B. E.; Nilsson, L. Thermal-Expansion of Lithium-Sulfate. *Z Naturforsch A* **1983**, *38*, 1396−1399.

(14) Witschas, M.; Eckert, H.; Freiheit, H.; Putnis, A.; Korus, G.; Jansen, M. Anion Rotation and Cation Diffusion in Low-Temperature Sodium Orthophosphate: Results from Solid-State NMR. *J. Phys. Chem. A* **2001**, *105*, 6808−6816.

(15) Borjesson, L.; Torell, L. M. Reorientational Motion in Superionic Sulfates - a Raman Linewidth Study. *Phys. Rev. B* **1985**, *32*, 2471−2477.

(16) Lunden, A. Enhancement of Cation Mobility in Some Sulfate Phases Due to a Paddle-Wheel Mechanism. *Solid State Ionics* **1988**, *28-30*, 163−167.

(17) Martelli, P.; et al. Rotational Motion in $LiBH_4$/LiI Solid Solutions. *J. Phys. Chem. A* **2011**, *115*, 5329−5334.

(18) Remhof, A.; Lodziana, Z.; Martelli, P.; Friedrichs, O.; Zuttel, A.; Skripov, A. V.; Embs, J. P.; Strassle, T. Rotational Motion of BH_4 Units in MBH_4 (M = Li,Na,K) from Quasielastic Neutron Scattering and Density Functional Calculations. *Phys. Rev. B* **2010**, *81*, 214304.

(19) Babanova, O. A.; Soloninin, A. V.; Stepanov, A. P.; Skripov, A. V.; Filinchuk, Y. Structural and Dynamical Properties of $NaBH_4$ and KBH_4: NMR and Synchrotron X-ray Diffraction Studies. *J. Phys. Chem. C* **2010**, *114*, 3712−3718.

(20) Ikeshoji, T.; Tsuchida, E.; Morishita, T.; Ikeda, K.; Matsuo, M.; Kawazoe, Y.; Orimo, S. Fast Ionic Conductivity of Li^+ in $LiBH_4$. *Phys. Rev. B* **2011**, *83*, 144301.

(21) Blanchard, D.; et al. Hindered Rotational Energy Barriers of BH_4^- Tetrahedra in β-$Mg(BH_4)_2$ from Quasielastic Neutron Scattering and DFT Calculations. *J. Phys. Chem. C* **2012**, *116*, 2013−2023.

(22) Dimitrievska, M.; et al. Carbon Incorporation and Anion Dynamics as Synergistic Drivers for Ultrafast Diffusion in Superionic $LiCB_{11}H_{12}$ and $NaCB_{11}H_{12}$. *Adv. Energy Mater.* **2018**, *8*, 1703422.

(23) Kweon, K. E.; Varley, J. B.; Shea, P.; Adelstein, N.; Mehta, P.; Heo, T. W.; Udovic, T. J.; Stavila, V.; Wood, B. C. Structural, Chemical, and Dynamical Frustration: Origins of Superionic Conductivity in closo-Borate Solid Electrolytes. *Chem. Mater.* **2017**, *29*, 9142−9153.

(24) Skripov, A. V.; Skoryunov, R. V.; Soloninin, A. V.; Babanova, O. A.; Tang, W. S.; Stavila, V.; Udovic, T. J. Anion Reorientations and Cation Diffusion in $LiCB_{11}H_{12}$ and $NaCB_{11}H_{12}$: ^1H, ^7Li, and ^{23}Na NMR Studies. *J. Phys. Chem. C* **2015**, *119*, 26912−26918.

(25) Tang, W. S.; Dimitrievska, M.; Stavila, V.; Zhou, W.; Wu, H.; Talin, A. A.; Udovic, T. J. Order-Disorder Transitions and Superionic Conductivity in the Sodium nido-Undeca(carba)borates. *Chem. Mater.* **2017**, *29*, 10496−10509.

(26) Tang, W. S.; et al. Liquid-like Ionic Conduction in Solid Lithium and Sodium Monocarba-closo-decaborates near or at Room Temperature. *Adv. Energy Mater.* **2016**, *6*, 1502237.

(27) Udovic, T. J.; et al. Exceptional Superionic Conductivity in Disordered Sodium Decahydro-closo-decaborate. *Adv. Mater.* **2014**, *26*, 7622−7626.

(28) Varley, J. B.; Kweon, K.; Mehta, P.; Shea, P.; Heo, T. W.; Udovic, T. J.; Stavila, V.; Wood, B. C. Understanding Ionic Conductivity Trends in Polyborane Solid Electrolytes from Ab Initio Molecular Dynamics. *ACS Energy Lett.* **2017**, *2*, 250−255.

(29) Fang, H.; Jena, P. Sodium Superionic Conductors Based on Clusters. *ACS Appl. Mater. Interfaces* **2019**, *11*, 963−972.

(30) Fang, H.; Jena, P. Li-Rich Antiperovskite Superionic Conductors Based on Cluster Ions. *Proc. Nat. Acad. Sci.* **2017**, *114*, 11046−11051.

(31) Sun, Y.; et al. Rotational Cluster Anion Enabling Superionic Conductivity in Sodium-Rich Antiperovskite Na_3OBH_4. *J. Am. Chem. Soc.* **2019**, *141*, 5640−5644.

(32) Skripov, A. V.; Soloninin, A. V.; Filinchuk, Y.; Chernyshov, D. Nuclear Magnetic Resonance Study of the Rotational Motion and the Phase Transition in $LiBH_4$. *J. Phys. Chem. C* **2008**, *112*, 18701−18705.

(33) Epp, V.; Wilkening, M. Fast Li Diffusion in Crystalline $LiBH_4$ due to Reduced Dimensionality: Frequency-Dependent NMR Spectroscopy. *Phys. Rev. B* **2010**, *82*, No. 020301.

(34) Skoryunov, R. V.; Babanova, O. A.; Soloninin, A. V.; Skripov, A. V.; Orimo, S. Nuclear Magnetic Resonance Study of Atomic Motion in the Mixed Borohydride-Amide $Li_2(BH_4)(NH_2)$. *J. Alloys Compd.* **2020**, *823*, 153821.

(35) Skripov, A. V.; Soloninin, A. V.; Babanova, O. A.; Skoryunov, R. V. Anion and Cation Dynamics in Polyhydroborate Salts: NMR Studies. *Molecules* **2020**, *25*, 2940.

(36) Gao, Y.; Nolan, A. M.; Du, P.; Wu, Y.; Yang, C.; Chen, Q.; Mo, Y.; Bo, S.-H. Classical and Emerging Characterization Techniques for Investigation of Ion Transport Mechanisms in Crystalline Fast Ionic Conductors. *Chem. Rev.* **2020**, *120*, 5954−6008.
(37) Adams, S.; Prasada Rao, R. Structural requirements for fast lithium ion migration in $Li_{10}GeP_2S_{12}$. *J. Mater. Chem.* **2012**, *22*, 7687−7691.
(38) Kamaya, N.; et al. A Lithium Superionic Conductor. *Nat. Mater.* **2011**, *10*, 682−686.
(39) Zhang, Z.; Li, H.; Kaup, K.; Zhou, L.; Roy, P.-N.; Nazar, L. F. Targeting Superionic Conductivity by Turning on Anion Rotation at Room Temperature in Fast Ion Conductors. *Matter* **2020**, *2*, 1667−1684.
(40) Bachman, J. C.; et al. Inorganic Solid-State Electrolytes for Lithium Batteries: Mechanisms and Properties Governing Ion Conduction. *Chem. Rev.* **2016**, *116*, 140−162.
(41) Ohno, S.; Banik, A.; Dewald, G. F.; Kraft, M. A.; Krauskopf, T.; Minafra, N.; Till, P.; Weiss, M.; Zeier, W. G. Materials Design of Ionic Conductors for Solid State Batteries. *Progr. Energy* **2020**, *2*, No. 022001.
(42) Kraft, M. A.; et al. Influence of Lattice Polarizability on the Ionic Conductivity in the Lithium Superionic Argyrodites Li_6PS_5X (X = Cl, Br, I). *J. Am. Chem. Soc.* **2017**, *139*, 10909−10918.
(43) Minafra, N.; Kraft, M. A.; Bernges, T.; Li, C.; Schlem, R.; Morgan, B. J.; Zeier, W. G. Local Charge Inhomogeneity and Lithium Distribution in the Superionic Argyrodites Li_6PS_5X (X = Cl, Br, I). *Inorg. Chem.* **2020**, *59*, 11009−11019.
(44) Pecher, O.; et al. Atomistic Characterisation of Li^+ Mobility and Conductivity in $Li_{7-x}PS_{6-x}I_x$ Argyrodites from Molecular Dynamics Simulations, Solid-State NMR, and Impedance Spectroscopy. *Chem. − Eur. J.* **2010**, *16*, 8347−8354.
(45) Deiseroth, H. J.; Maier, J.; Weichert, K.; Nickel, V.; Kong, S. T.; Reiner, C. Li_7PS_6 and Li_6PS_5X (X: Cl, Br, I): Possible Three-dimensional Diffusion Pathways for Lithium Ions and Temperature Dependence of the Ionic Conductivity by Impedance Measurements. *Z. Anorg. Allg. Chem.* **2011**, *637*, 1287−1294.
(46) Hanghofer, I.; Brinek, M.; Eisbacher, S.; Bitschnau, B.; Volck, M.; Hennige, V.; Hanzu, I.; Rettenwander, D.; Wilkening, M. Substitutional Disorder: Structure and Ion Dynamics of the Argyrodites Li_6PS_5Cl, Li_6PS_5Br and Li_6PS_5I. *Phys. Chem. Chem. Phys.* **2019**, *21*, 8489−8507.
(47) Brinek, M.; Hiebl, C.; Wilkening, H. M. R. Understanding the Origin of Enhanced Li-Ion Transport in Nanocrystalline Argyrodite-Type Li_6PS_5I. *Chem. Mater.* **2020**, *32*, 4754−4766.
(48) de Klerk, N. J. J.; Roslon, T.; Wagemaker, M. Diffusion Mechanism of Li Argyrodite Solid Electrolytes for Li-Ion Batteries and Prediction of Optimized Halogen Doping: The Effect of Li Vacancies, Halogens, and Halogen Disorder. *Chem. Mater.* **2016**, *28*, 7955−7963.
(49) Ohno, S.; et al. How Certain Are the Reported Ionic Conductivities of Thiophosphate-Based Solid Electrolytes? *An Interlaboratory Study. ACS Energy Lett.* **2020**, *5*, 910−915.
(50) Boulineau, S.; Courty, M.; Tarascon, J. M.; Viallet, V. Mechanochemical Synthesis of Li-Argyrodite Li_6PS_5X (X = Cl, Br, I) as Sulfur-Based Solid Electrolytes for All-Solid-State Batteries Application. *Solid State Ionics* **2012**, *221*, 1−5.
(51) Bloembergen, N.; Purcell, E. M.; Pound, R. V. Nuclear Magnetic Relaxation. *Nature* **1947**, *160*, 475−476.
(52) Bloembergen, N.; Purcell, E. M.; Pound, R. V. Relaxation Effects in Nuclear Magnetic Resonance Absorption. *Phys. Rev.* **1948**, *73*, 679−712.
(53) Wilkening, M.; Heitjans, P. From Micro to Macro: Access to Long-Range Li^+ Diffusion Parameters in Solids via Microscopic ^6Li, ^7Li Spin-Alignment Echo NMR Spectroscopy. *Chem. Phys. Chem.* **2012**, *13*, 53−65.
(54) Kuhn, A.; Kunze, M.; Sreeraj, P.; Wiemhöfer, H. D.; Thangadurai, V.; Wilkening, M.; Heitjans, P. NMR Relaxometry as a Versatile Tool to Study Li Ion Dynamics in Potential Battery Materials. *Solid State Nucl. Magn. Reson.* **2012**, *42*, 2−8.
(55) Schmidt, W.; Wilkening, M. Diffusion-Induced ^7Li NMR Spin-Lattice Relaxation of Fully Lithiated, Mixed-Conducting $Li_7Ti_5O_{12}$. *Solid State Ionics* **2016**, *287*, 77−82.
(56) Uitz, M.; Epp, V.; Bottke, P.; Wilkening, M. Ion Dynamics in Solid Electrolytes for Lithium Batteries. *J. Electroceram.* **2017**, *38*, 142−156.
(57) Heitjans, P.; Schirmer, A.; Indris, S., *In Diffusion in Condensed Matter − Methods, Materials, Models*, Heitjans, P.; Kärger, J.. Springer: Berlin, 2005; 367−415.
(58) Mehrer, H., *Diffusion in Solids - Fundamentals, Methods, Materials, Diffusion-Controlled Processes*. Springer: Berlin, Heidelberg, 2007.
(59) Epp, V.; Gün, O.; Deiseroth, H. J.; Wilkening, M. Highly Mobile Ions: Low-Temperature NMR Directly Probes Extremely Fast Li^+ Hopping in Argyrodite-Type Li_6PS_5Br. *J. Phys. Chem. Lett.* **2013**, *4*, 2118−2123.
(60) Morgan, B. Mechanistic Origin of Superionic Lithium Diffusion in Anion-Disordered Li_6PS_5X Argyrodites. *chemrxiv* **2020**, 12349703.
(61) Wilkening, M.; Mühle, C.; Jansen, M.; Heitjans, P. Microscopic Access to Long-Range Diffusion Parameters of the Fast Lithium ion Conductor Li_7BiO_6 by Solid State ^7Li Stimulated Echo NMR. *J. Phys. Chem. B* **2007**, *111*, 8691−8694.
(62) Wilkening, M.; Heitjans, P. Extremely Slow Cation Exchange Processes in Li_4SiO_4 Probed Directly by Two-Time ^7Li Stimulated-Echo Nuclear Magnetic Resonance Spectroscopy. *J. Phys.: Condes. Matter* **2006**, *18*, 9849−9862.
(63) Ngai, K. L. Difference Between Nuclear Spin Relaxation and Ionic Conductivity Relaxation in Superionic Glasses. *J. Chem. Phys.* **1993**, *98*, 6424−6430.

https://dx.doi.org/10.1021/acs.jpcc.0c06090
J. Phys. Chem. C XXXX, XXX, XXX−XXX

3.3 Rapid Low-Dimensional Li^+ Ion Hopping Processes in Synthetic Hectorite-Type $Li_{0.5}[Mg_{2.5}Li_{0.5}]Si_4O_{10}F_2$

In search of new electrolytes for lithium-ion batteries, in-depth understanding of ionic transport in a variety of materials is essential. In the following article the synthetic hectorite-type $Li_{0.5}[Mg_{2.5}Li_{0.5}]Si_4O_{10}F_2$ was chosen as model material. Fluorohectorites are phyllosilicates (layered silicates) serving as a two-dimensional host material. It is assumed that lithium ions can move fast along the interlayers. Via the help of broadband conductivity spectroscopy, modulus analysis as well as ^7Li NMR spin-lattice relaxation measurements two-dimensional Li^+ hopping was studied in this synthetic clay material. The strength of the latter method lies in the capability to differentiate between high- and low-dimensional ion transport. The measurements showed that fast two-dimensional Li^+ diffusion indeed takes place with an overall activation energy of 0.35 eV and an ionic bulk conductivity of 0.14 mS cm^{-1} at room temperature. Further development of synthetic phyllosilicates may result in very high lithium ionic conductivities making them highly promising electrolyte candidates for the use in batteries. Finding inspiration in naturally occurring materials can lead to new classes of ionic conductors with remarkable conduction mechanisms and high ionic conductivities.

Rapid Low-Dimensional Li^+ Ion Hopping Processes in Synthetic Hectorite-Type $Li_{0.5}[Mg_{2.5}Li_{0.5}]Si_4O_{10}F_2$

C. Hiebl, P. Loch, M. Brinek, M. Gombotz, B. Gadermaier, P. Heitjans, J. Breu, and H. M. R. Wilkening

Chemistry of Materials **2020** *32* (17), 7445-7457

CHEMISTRY OF MATERIALS

pubs.acs.org/cm

Article

Rapid Low-Dimensional Li^+ Ion Hopping Processes in Synthetic Hectorite-Type $Li_{0.5}[Mg_{2.5}Li_{0.5}]Si_4O_{10}F_2$

Caroline Hiebl,[#] Patrick Loch, Marina Brinek,[#] Maria Gombotz, Bernhard Gadermaier, Paul Heitjans,* Josef Breu, and H. Martin. R. Wilkening*

Cite This: *Chem. Mater.* 2020, 32, 7445−7457

Read Online

ACCESS | Metrics & More | Article Recommendations | Supporting Information

ABSTRACT: Understanding the origins of fast ion transport in solids is important to develop new ionic conductors for batteries and sensors. Nature offers a rich assortment of rather inspiring structures to elucidate these origins. In particular, layer-structured materials are prone to show facile Li^+ transport along their inner surfaces. Here, synthetic hectorite-type $Li_{0.5}[Mg_{2.5}Li_{0.5}]Si_4O_{10}F_2$, being a phyllosilicate, served as a model substance to investigate Li^+ translational ion dynamics by both broadband conductivity spectroscopy and diffusion-induced ^7Li nuclear magnetic resonance (NMR) spin−lattice relaxation experiments. It turned out that conductivity spectroscopy, electric modulus data, and NMR are indeed able to detect a rapid 2D Li^+ exchange process governed by an activation energy as low as 0.35 eV. At room temperature, the bulk conductivity turned out to be in the order of 0.1 mS cm^{-1}. Thus, the silicate represents a promising starting point for further improvements by crystal chemical engineering. To the best of our knowledge, such a high Li^+ ionic conductivity has not been observed for any silicate yet.

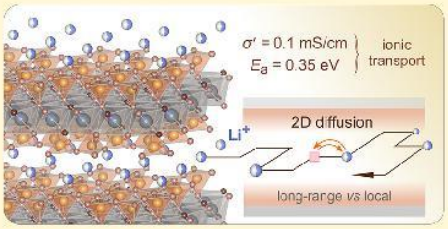

1. INTRODUCTION

The diffusion of small cations and anions plays an important role in many devices such as sensors[1−3] and batteries.[4−11] Although for some applications, e.g., in the semiconductor industry[12] or in the development of breeding materials[13−15] for fusion reactor blankets, diffusion is unwanted, in other branches, materials with extremely high diffusion coefficients are desired.[16−21] Finding the right material and tailoring its dynamic properties further requires an in-depth understanding of the origins that determine fast ion dynamics.[22−26]

In many cases, layer-structured materials[27−30] are known to offer fast diffusion pathways along the buried interfaces or between larger gaps inside the crystal structure.[31] Commonly, powder samples are synthesized and investigated; however, polycrystalline samples do not allow orientation-dependent measurements of ionic conductivity. Fortunately, anisotropic properties of ionic transport in polycrystalline samples can be probed by nuclear magnetic resonance (NMR) spin−lattice relaxation experiments.[5,30,32−35] The most prominent examples, whose Li^+ diffusion properties were studied in this way,[36] include graphite[37,38] or transition metal chalcogenides such as TiS_2,[39−43] NbS_2,[44,45] and SnS_2.[46] Recently, two-dimensional (2D) Li^+ diffusion has also been determined in hexagonal $LiBH_4$.[29,47] Fast fluoride, F^-, diffusion is observed in $MeSnF_4$ (Me = Pb, Ba) and, as has been shown quite recently, also in layer-structured $RbSn_2F_5$.[48] In these materials, spatial constraints guide the ions over long distances. The principle of guided ions has also been found in $Li_{12}Si_7$.[49,50] In binary silicide, the Li^+ ions are subjected to a fast one-dimensional diffusion process along the surface of a virtual pipe formed by the stacked Si_5 rings.[49] In channel-structured materials with the ions diffusing *inside* the channels, their diffusion pathways may, however, easily be blocked by foreign, immobile ions.[51] The same effect might, of course, also influence 2D translational ion dynamics but to a lesser degree.

To understand Li^+ diffusion in structures offering 2D diffusion pathways, we chose hectorite-type $Li_{0.5}[Mg_{2.5}Li_{0.5}]Si_4O_{10}F_2$ as a model system, see Figure 1, and studied the Li^+ self-diffusion properties and electrical ionic transport. While the latter is investigated by broadband conductivity spectroscopy,[52] we took advantage of ^7Li NMR spin−lattice relaxation measurements[32,53] to shed light on Li^+ translational dynamics.

Hectorite is, as montmorillonite, a clay mineral of the smectite group (gr. *σμηκτις*, soil with the ability to clean, to soak something up, e.g., swelling through water uptake). Such silicates belong to the family of phyllosilicates (gr. *φυλλο*, leaf). Fluorohectorite is a 2D host material with a rigid 2:1 sandwich-like structure;[54] each lamella is composed of two silicate and one Mg^{2+} rich layer where the earth alkaline cations are octahedrally coordinated by oxygen and fluorine anions. An idealized structure of synthetic (turbostratic) Li-bearing

Received: June 12, 2020
Revised: August 5, 2020
Published: August 5, 2020

https://dx.doi.org/10.1021/acs.chemmater.0c02460
Chem. Mater. 2020, 32, 7445−7457

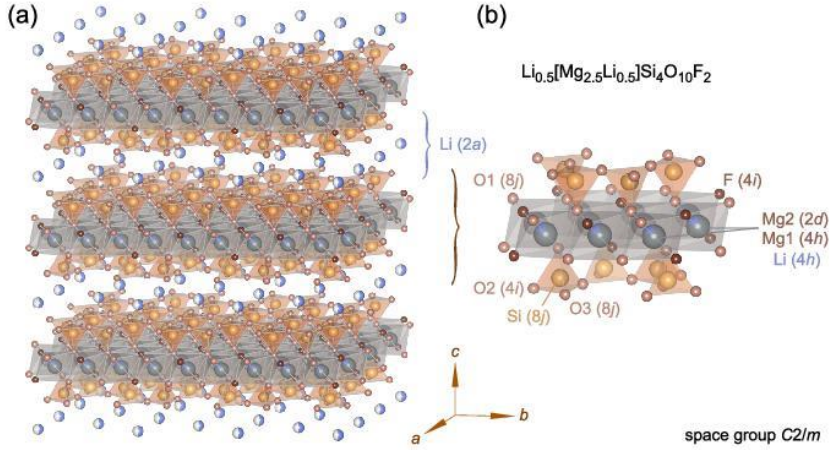

Figure 1. (a) Idealized crystal structure of hectorite-type $Li_{0.5}[Mg_{2.5}Li_{0.5}]Si_4O_{10}F_2$ (drawn according to the space group $C2/m$, the real structure is clearly turbostratic) with two distinct crystallographic sites occupied by the Li ions. Those between the Mg-rich layers (see (b)), which are here shown following a homogenous charge distribution, are expected to have access to fast 2D diffusion pathways.

fluorohectorite $[Li_{0.5}]^{inter}[Mg_{2.5}Li_{0.5}]^{octa}[Si_4]^{tetra}O_{10}F_2$ is shown in Figure 1. Natural hectorite of the composition $Na_{0.3}(Mg, Li)_3Si_4O_{10}(OH)_2$, including also minor amounts of Ca^{2+}, K^+, and Al^{3+}, was named for its occurrence 5 km south of Hector (San Bernardino County, California, USA).[55] It was first described in 1941 and found in a bentonite deposit, altered from clinoptilolite, a natural zeolite, derived from volcanic tuff and ash with a high glass content.[55] Cation exchange strategies allow one to effectively replace the Na ions in hectorite by Li ions; also larger inorganic or organic molecules (pillars) can be introduced, resulting in porous so-called pillared clays.[54] Exemplarily, the Khan group successfully used hectorite-based materials as passive and active filler materials to prepare nanocomposite polymer-based (gel) electrolytes as well as to develop composite $LiCoO_2$-based cathode materials.[56−59] Here, our hypothesis is that the interlayer gap in such host structures, particularly that of hectorite, offers indeed fast diffusion pathways for small charge carriers such as Li^+ and Na^+ ions.

Verifying the hypothesis of 2D transport is, however, challenging if only powder samples are available at hand. Fortunately, ^{7}Li NMR spin−lattice relaxation measurements,[49,53] also successfully used to characterize electrolytes for batteries,[60,61] represent a unique tool to study such anisotropic properties even for powdered samples, since the spectral density functions J governing the NMR spin−lattice relaxation rates $1/T_1$ ($\propto J$) possess specific features for 1, 2, and 3D ion transport.[30,62] As intimated above, low-dimensional ionic transport has, so far, been probed only for a limited number of materials by NMR relaxation techniques.[36] The present study contributes to this research field and is aimed at answering the question whether 2D silicate structures offer an assortment of materials with enhanced ion diffusion properties.

2. EXPERIMENTAL SECTION

2.1. Preparation and Characterization of $Li_{0.5}[Mg_{2.5}Li_{0.5}]Si_4O_{10}F_2$. Lithium fluorohectorite with the nominal composition of $Li_{0.5}[Mg_{2.5}Li_{0.5}]<Si_4 > O_{10}F_2$ was prepared by a two-step ion exchange procedure starting from melt synthesized Na-fluorohectorite ($Na_{0.5}[Mg_{2.5}Li_{0.5}]<Si_4 > O_{10}F_2$). The Na-fluorohectorite was synthesized according to a preparation route published earlier.[54,63] To ensure the complete exchange of Na^+ by Li^+, Na-fluorohectorite was first treated with n-butylammonium chloride ($C_4H_{12}ClN$ (C4), 2 M) using a 100-fold excess of its cation exchange capacity (CEC) to obtain the so-called C4-fluorohectorite. Typically, 500 mg of Na-fluorohectorite was exchanged overnight five times with 40 mL of C4 solution at 80 °C. The resulting product was washed five times with an ethanol−water mixture (1:1) and once more with pure ethanol. Atomic absorption spectroscopy (AAS), see below, was used to check the completeness of the ion exchange reaction. After this, the dried C4-fluorohectorite was treated with a 100-fold excess of the CEC of LiOH (2 M, 4 times 40 mL, 6 h, room temperature). While removing excessive LiOH by washing 6 times with 40 mL of deionized water, the ionic strength decreased to a value lower than 0.02 M; furthermore, complete delamination by repulsive osmotic swelling was observed.[63−66] Finally, the gel of delaminated Li-fluorohectorite was freeze-dried followed by vacuum drying at 160 °C.

2.1.1. AAS. To verify complete Na^+-exchange, AAS was used. For this purpose, approximately 20 mg of the samples were weighed into clean Teflon-flasks of 15 mL volume. After the addition of 1.5 mL of 30 wt % HCl (Merck), 0.5 mL of 85 wt % H_3PO_4 (Merck), 0.5 mL of 65% HNO_3 (Merck), and 1 mL of 48 %HBF_4 (Merck), the samples were digested in a 1200 Mega microwave digestion apparatus (MLS, Mikrowellen-Labor-Systeme) for 6.5 min and heated at 600 W. Afterward, the closed sample container was cooled to room temperature; the clear solution was diluted to 100 mL in a volumetric flask and analyzed with a Varian AA100-spectrometer. To determine the Na^+-content by AAS, a five-point calibration curve (0.0 to 0.2 mg/100 mL) was measured by diluting a Na^+ standard AAS-solution (1000 mg/mL) in nitric acid.

2.1.2. CHN-Analysis. A Elementar Unicode equipped with a combustion tube filled with tungsten(VI)-oxide-granules was used to analyze the elements C, H, and N at a combustion temperature of 1050 °C. Samples were dried at 120 °C prior to the measurement.

2.1.3. Physisorption Measurements. Argon adsorption measurements were performed using a Quantachrome Autosorb at 87.35 K using samples that were dried at 120 °C for 24 h in a high vacuum. The pore sizes and volumes were calculated using a nonlocal DFT model (software version 2.11, Ar on zeolite/silica, cylindrical pores, equilibrium model).

2.2. Conductivity Spectroscopy. To perform broadband conductivity measurements, the hectorite sample was first ground in a mortar before the sample was uniaxially pressed (0.5 tons) into a cylindrical pellet with a diameter of 5 mm and a thickness of approximately 1 mm; the exact thickness was determined with a vernier calliper. The pellet was equipped on both sides with Au electrodes that blocked Li^+ ion transport. For this purpose, we used an EM SCD 050 sputter coater from LEICA. The thickness (100 nm) was controlled with a quartz thickness monitoring system. The pellet was then placed inside an active ZGS cell (Novocontrol), which was

https://dx.doi.org/10.1021/acs.chemmater.0c02460
Chem. Mater. 2020, 32, 7445−7457

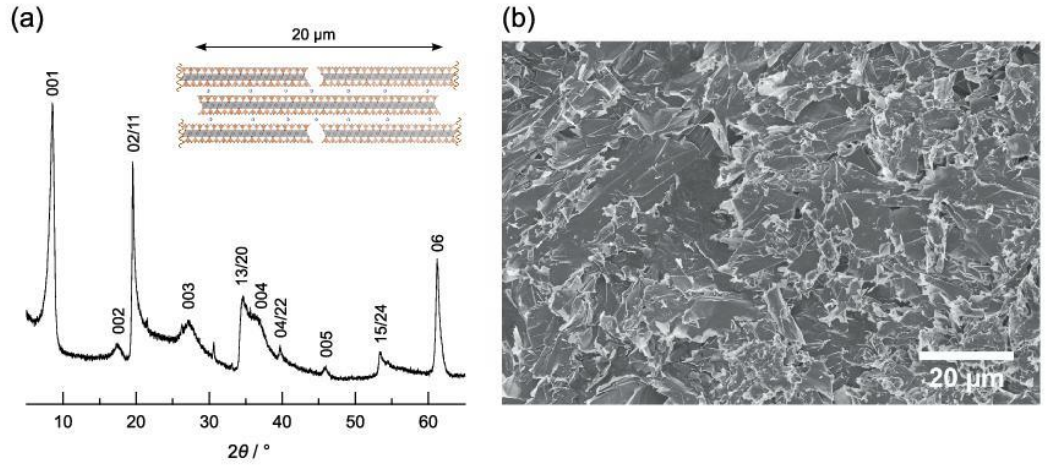

Figure 2. (a) Powder X-ray diffraction pattern of dry Li-fluorohectorite $Li_{0.5}[Mg_{2.5}Li_{0.5}]Si_4O_{10}F_2$ with marked reflections of the 00 L series and the *hk* bands; the inset shows the representative bandlike structure of the hectorite. (b) Scanning electron micrograph of freeze-dried and partially restacked Li-fluorohectorite.

connected to a Novocontrol Concept 80 broadband dielectric spectrometer. We measured the complex impedance, conductivity, and permittivity as a function of temperature and in a frequency range of 0.01 Hz to 10 MHz. The ZGS sample holder was placed in a cryostat, allowing us to measure conductivity isotherms from 133 to 433 K in steps of 20 K. Temperature regulation and monitoring was carried out with a QUATRO controller (Novocontrol). In order to eliminate residual moisture, the pellet was pre-dried in the impedance cell at 433 K (160 °C) for 4 h. During the entire measurement, the impedance cell was permanently flushed with dry, freshly evaporated nitrogen gas.

2.3. Magic Angle Spinning (MAS) NMR. ^{6}Li (73.6 MHz, 120 W power amplifier, 1024 scans, recycle delay $5T_1$ (see below), pulse length 3 μs) and ^{19}F (470.6 MHz, 50 W, 32 scans, recycle delay 1 s, pulse length 2.1 μs) MAS one-pulse NMR spectra were recorded with a 500-MHz Avance spectrometer (Bruker). The measurements were carried out at a rotation speed of 25 kHz using 2.5 mm rotors. The spectra were recorded using one-pulse sequences with ambient bearing gas. Crystalline $LiCH_3COO$ and liquid $CFCl_3$ served as reference materials to determine the isotropic chemical shifts δ_{iso}.

2.4. Time-Domain ^{7}Li NMR Measurements. To prepare the sample for NMR measurements, the hectorite powder sample was ground using a mortar and pestle under an Ar atmosphere in a glove box. After this, it was dried in a vacuum at 160 °C before being fire-sealed in Duran ampoules under vacuum. We recorded both ^{7}Li NMR spectra and ^{7}Li NMR spin−lattice relaxation rates as a function of temperature (173 to 433 K). For this purpose, we used a Bruker 300-MHz spectrometer that was connected to a Bruker cryomagnet with a nominal magnetic field of 7 T. This field corresponds to a nominal ^{7}Li Larmor frequency of $\omega_0/2\pi$ = 116 MHz. While laboratory frame spin−lattice relaxation rates ($1/T_1$) were recorded with the saturation recovery pulse sequence,[67] the spin-lock technique[67,68] was applied to measure transversal magnetization transients leading to the rate $1/T_{1\rho}$, which characterizes spin−lattice relaxation in the so-called rotating frame of reference. The 90° pulse length (t_p) was 2 μs (200 W broadband amplifier) and showed only a slight dependence on temperature. To measure $1/T_1$, we used a comb of 10 closely spaced (80 μs) radio frequency pulses to destroy any longitudinal magnetization M. The subsequent recovery of M as a function of the delay time t_d (4 scans) was followed with a 90° detection pulse; the delay between each scan, although not needed, was set to 1 s. In general, $M(t_d)$ follows a stretched exponential behavior according to $M(t_d) = M_0(1 - \exp[-(t_d/T_1)^{\gamma'}])$, $0<\gamma'\leq 1$. M_0 denotes the equilibrium magnetization that is reached at $t_d \rightarrow \infty$. Here, $M(t_d)$ follows a bi-exponential behavior if the full area under the free induction decays (FIDs) is used to construct $M(t_d)$, see the Supporting Information, Figure S2. In this case, we used a sum of stretched exponentials to parameterize the transient.[31,69,70] Alternatively, the two components of the FIDs were separately analyzed, as explained below. For the corresponding spin-lock $M_\rho(t_d)$ transients (see also Figure S2), we used a single, stretched exponential function to analyze the decay functions: $M_\rho(t_{lock}) \propto \exp[-(t_{lock}/T_{1\rho})^\gamma])$, t_{lock} denotes the duration of the locking pulse. We varied t_{lock} from 30 μs to 30 ms (8 scans per locking time) and used a power level that results in a locking frequency $\omega_1/2\pi$ of ca. 20 kHz. The recycle delay between each scan was at least $5T_1$. This value is orders of magnitude lower than $\omega_0/2\pi$ used for the laboratory-frame measurements; hence, spin-lock NMR is sensitive to much slower Li ion dynamics compared to probing via T_1 measurements.

3. RESULTS AND DISCUSSION

3.1. Synthesis of the Li-Fluorohectorites. Direct melt synthesis of Li-fluorohectorites is troublesome. In general, melt-synthesized Li-fluorohectorites may contain a range of impurities and could suffer from isomorphous substitution effects. Thus, the charge density of the silicate layers turned out to be heterogeneous as described earlier.[71] In contrast to the Li-bearing compound, melt synthesis of Na-fluorohectorite followed by long-term annealing yields phase pure materials with a homogenous charge density and, thus, a uniform intracrystalline reactivity.[54,63] This uniform intracrystalline reactivity is especially important for a uniform cation distribution in the interlayer space, which in turn is expected to have a considerably high impact on cation transport properties. Therefore, the Li-fluorohectorite used for the present study was prepared by taking advantage of a complete ion exchange of Na-fluorohectorite. Unfortunately, the affinity of Li^+ for the interlayer space of hectorites is lower than that of Na^+.[72] Consequently, complete ion exchange could not be accomplished directly, even at very high incoming Li^+-concentrations. Therefore, Na^+ was fully exchanged with C4 taking advantage of the much higher selectivity of organic cations for the interlayer space.[73] The completeness of ion exchange at this stage was verified by AAS.

In the next step, Li exchange to Li-fluorohectorite could be driven by deprotonation of the intercalated C4. Elemental analysis proved complete replacement of C4 within experimental errors. At low ionic strength, i.e., at values being smaller than 0.02 M as achieved during the washing

https://dx.doi.org/10.1021/acs.chemmater.0c02460
Chem. Mater. 2020, 32, 7445−7457

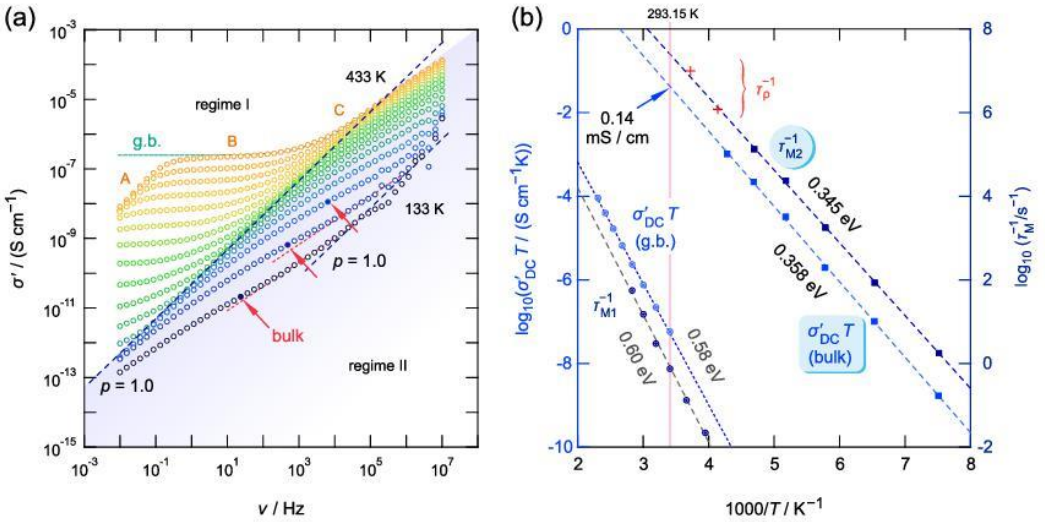

Figure 3. (a) Conductivity isotherms of layer-structured, hectorite-type $Li_{0.5}[Mg_{2.5}Li_{0.5}]Si_4O_{10}F_2$ recorded from T = 133 K to T = 433 K; the measurements span a frequency range of 9 decades. In regime I, the isotherms are governed by the grain boundary (g.b.) response, while in regime II, bulk properties dominate the shape of the curves. See text for further details. (b) Arrhenius plot showing both $\log_{10}(\sigma'_{DC}T/(S\ cm^{-1}\ K))$ and $\log_{10}(1/\tau_M\ /\ s^{-1})$ vs. the inverse temperature $1000/T$. The left axis refers to σ'_{DC} showing either the temperature behavior of the bulk ion conductivity or that governed by the highly resistive g.b. regions. The latter denotes the total conductivity seen in regime I of the isotherms shown in (a). $1/\tau_{Mi}$ refers to the two maxima (i = 1, 2) seen in the electric modulus curves $M''(\nu)$, see Figure 4b, whereas $1/\tau_{M1}$ refers to the g. b. response and $1/\tau_{M1}$ denotes the characteristic electrical relaxation rates of the $M''(\nu)$-peak representing the bulk response. Lines, either dashed or dotted, show Arrhenius fits with the activation energies indicated. At room temperature, $\sigma'_{DC,\ bulk} \approx 0.14$ mS cm^{-1} is expected through extrapolation of the Arrhenius line shown. For comparison, the rates $1/\tau_\rho$ from electrical resistivity measurements carried out at a fixed frequency (1.2 MHz, 10 MHz, see Figure 5b) are included as well.

procedure,[63] Li-hectorite delaminates spontaneously in aqueous suspension by repulsive osmotic swelling whereupon a liquid crystalline gel is obtained. Freeze drying of this gel leads to a voluminous, spongelike, and hierarchically porous material (Figure 2b).

The powder X-ray diffraction pattern of dry Li-fluorohectorite is shown in Figure 2a and shows the characteristic reflections of the *00 L*-series with a basal spacing of 10.2 Å. Missing *hkl* reflections and occurrence of the λ-shape of *02/11-*, *13/20-*, *04/22-*, *15/24-*, and *06*-bands indicated a turbostratic type of stacking of adjacent silicate layers. Upon drying, partial restacking is forced with large overlapping areas between adjacent individual layers (20 μm diameter) and leads to bandlike aggregate structures (Figure 1b). Consequently, Li^+ cations are residing at external basal planes and in the interlayer space. The ratio of the two Li sites can only be estimated. The thickness of the restacked tactoids cannot be determined by analyzing the full width at half maximum (fwhm) of basal reflections via the Scherrer equation because the broadening is largely determined by random interstratification of the slightly varying stacking vector. Because of turbostratic disorder, the PXRD pattern contains little structural information beyond basal spacing, which is obvious when comparing a simulated XRD pattern (see Figure S1) for a hypothetical, fully 3D ordered Li-hectorite structure ($C2/m$ (no. 12), a = 5.25(2) Å, b = 9.08(3) Å, c = 10.37(4) Å, β = 96.51(8)°). Since the *hk*-bands are located approximately at the position of *hk0* reflections, this unit cell could be refined by applying the experimental turbostratic pattern, although with some uncertainty in the *ab*-dimensions. As ion exchange is a topotactic reaction, the structure of the silicate layers is fully preserved as indicated by *ab*-dimensions being similar to dimensions found for a 3D ordered member of the hectorite family (a = 5.2434(10) Å; b = 9.0891(18) Å).[74] The latter, refined structure of the silicate layer could, therefore, be safely applied to obtain Figure 1 and to draw the scheme shown in the inset of Figure 2a.

As the interlayer surface area in the collapsed dry state is not accessible to probe gas molecules, the degree of restacking can, however, be deduced from the specific surface area determined by physisorption. Given the large diameter, the contribution of edges to the total surface area can be safely neglected. The specific surface area per gram for an individual delaminated silicate layer was calculated from the known *ab* dimension and the formula weight. The ratio of this calculated surface area (759.368 m^2/g) and the surface area measured by Brunauer–Emmett–Teller analysis (5.174 m^2/g) yields the average number n_l of layers in the stack, n_l = 147. This estimation indicates that most of the Li^+ ions are indeed located in the interlayer space.

3.2. Ionic Transport and Li^+ Diffusivity. In Figure 3a, the broadband conductivity isotherms of layer-structured $Li_{0.5}[Mg_{2.5}Li_{0.5}]Si_4O_{10}F_2$ are shown. The isotherms, which show the real part of the complex conductivity σ' as a function of frequency ν, were recorded over a dynamic range of 9 decades.

The conductivity curves can be subdivided into several parts, labelled A, B, and C (Figure 3a). To explain these features, we first consider the isotherm recorded at the highest temperature, that is, at T = 433 K (regime I). At low frequencies ν, electrode polarization appears, which manifests itself as a drop in conductivity (A). With increasing frequency, σ' enters the so-called direct current (DC) plateau that corresponds to long-range ion transport in $Li_{0.5}[Mg_{2.5}Li_{0.5}]Si_4O_{10}F_2$ (B). The associated capacitance C of this distinct plateau is in the order of 300 pF ($= C_{gb}$). Without any doubt, such a high value

https://dx.doi.org/10.1021/acs.chemmater.0c02460
Chem. Mater. 2020, 32, 7445−7457

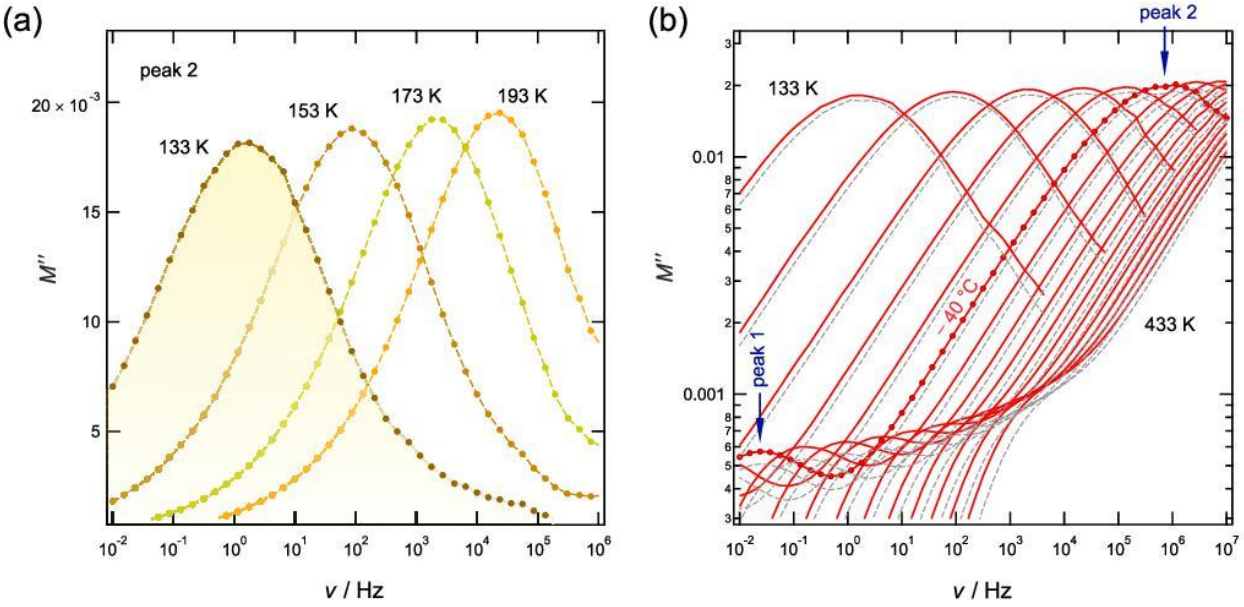

Figure 4. (a) Electrical modulus curves $M''(\nu)$ of hectorite-type $Li_{0.5}[Mg_{2.5}Li_{0.5}]Si_4O_{10}F_2$, which were recorded at the temperatures indicated. (b) Same curves as in (a) but using a double logarithmic plot to visualize also those peaks that are governed by a higher permittivity (and capacitance), see arrow pointing at the peak that appears at 0.03 Hz (233 K). The latter reflects g.b. responses, while the main modulus peaks are produced by bulk electrical relaxation processes characterized by a much lower permittivity, see the arrow pointing at the peak at $\nu = 8 \times 10^5$ Hz. The dashed lines show the response of a measurement on a second pellet prepared, indicating the good reproducibility of the analysis.

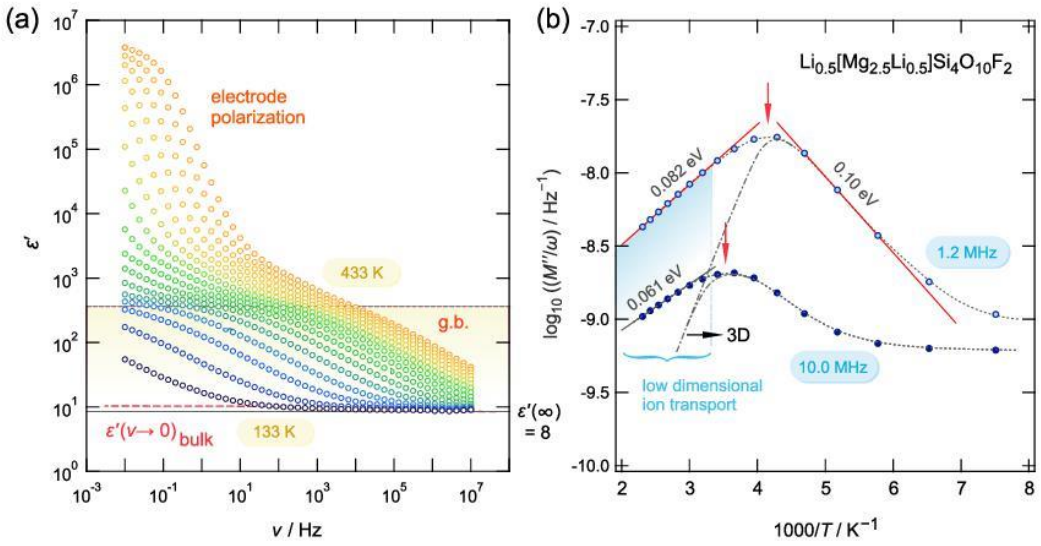

Figure 5. (a) Change of the electrical permittivity of layer-structured $Li_{0.5}[Mg_{2.5}Li_{0.5}]Si_4O_{10}F_2$ as a function of frequency and temperature. While the bulk region ($\varepsilon'_b(0) = 10$) is hardly seen in this representation, the g.b. response ($\varepsilon'_{gb}(0) = 360$) and electrode polarization ($\varepsilon'_p(0) > 10^6$) dominate the isotherms, which were recorded from 133 to 433 K in steps of 20 K. (b) Temperature behavior of the electric resistivity is expressed as M''/ω and measured at two different frequencies $\omega/2\pi = 1.2$ and 10.0 MHz. The fact that the flanks at high temperatures do not coincide is an indication of low-dimensional ion transport; 3D ion dynamics would yield the behavior indicated by the dashed-dotted lines. From the peak maxima, two electrical relaxation rates can be deduced that are also included in Figure 3b. See text for further explanations.

corresponds to an electrical process that is dominated by g.b. regions.[75] Increasing the frequency further leads to the associated dispersive part (C) of the DC plateau, which follows a $\sigma' \propto \nu^{p=1}$ behavior as indicated by the dashed line in Figure 3a.

With decreasing temperature, $\sigma'_{DC,\,gb}$ decreases and the curves are shifted toward lower frequencies. At sufficiently low T, a second DC plateau could be revealed (see regime II). This plateau does only appear as a curvature of the isotherms shown in regime II of Figure 3a. Its dispersive regime is only hardly visible; at very low temperatures and high frequency, the exponent p in the Jonscher-type relation $\sigma' \propto \nu^p$ approaches 1, indicating the beginning of a nearly constant loss behavior.[76−81] Most importantly, while total conductivities, domi-

https://dx.doi.org/10.1021/acs.chemmater.0c02460
Chem. Mater. 2020, 32, 7445−7457

nated by the g.b. response, can easily be read off from the distinct plateaus in regime I (see Figure 3a), $\sigma'_{DC,\,b}$ values characterizing bulk ion transport are only accessible by careful evaluation of the curvature seen in regime II. Filled symbols in Figure 3a mark estimations of these values.

The temperature dependence of both values, $\sigma'_{DC,\,b}$ and $\sigma'_{DC,\,gb}$, is analyzed using the Arrhenius plot shown in Figure 3b. Conductivities dominated by ion-blocking grain boundaries obey the Arrhenius law with an activation energy $E_{a\,gb}$ of 0.58 eV. Lines in Figure 3b refer to $\sigma'_{DC}T = \sigma_0$ exp. $(-E_a/(k_BT))$ with σ_0 being the pre-exponential factor and k_B denoting Boltzmann's constant. Compared to $\sigma'_{DC,\,gb}$ the bulk conductivity values $\sigma'_{DC,\,b}$ turned out to be higher by 6 orders of magnitude, and bulk ion transport has to be characterized by an activation energy of $E_{a,\,b}$ = 0.36 eV. Extrapolating the estimated values $\sigma'_{DC,\,b}$ toward room temperature yields 0.14 mS cm^{-1} at 293 K. This value is comparable to those reported for garnet-type oxides such as cubic-$Li_7La_3Zr_2O_{12}$ being considered as powerful electrolytes for ceramic electrochemical energy storage systems.[10]

To support our claim that the curvatures in regime II of Figure 3a are suitable to estimate bulk ion conductivities of hectorite-type $Li_{0.5}[Mg_{2.5}Li_{0.5}]Si_4O_{10}F_2$, we analyzed electric modulus curves, $M''(\nu)$, which we recorded at a fixed temperature and variable frequencies.[48] The corresponding curves are shown in Figure 4a by using a half-logarithmic plot and in Figure 4b by taking advantage of the double-logarithmic scaling to illustrate the change of M'' with frequency.

In general, the complex modulus $\boldsymbol{M}^*$ is given by the inverse complex permittivity, $M^* = 1/\boldsymbol{\varepsilon}^*$. The real part of $\boldsymbol{\varepsilon}^*$, denoted as ε', is shown in Figure 5a. As seen for σ', also $\varepsilon'(\nu)$ passes through the same electrical regimes viz. electrode polarization, g.b., and bulk response. The latter is only slightly seen for the isotherms recorded at very low temperatures. The permittivity value $\varepsilon'_b(\nu \rightarrow 0) = 10$ (see Figure 5a) corresponds to $C_b < 10$ pF if we use the relation for a plate capacitor, $C = \varepsilon_0\varepsilon'_bA/d$, to estimate the associated bulk capacitance. Here, ε_0 is the vacuum permittivity, A denotes the area of the pellet and d its thickness. Importantly, the imaginary part of M^*, M'', is dominated by bulk effects as the amplitude of M'' is proportional to the inverse of $C_{b,\,(gb)}$, $M'' \propto 1/C$. Hence, we expect a clearly visible bulk $M''(\nu)$ peak accompanied by a second one, the g.b. response, being drastically reduced in magnitude. As compared to the main peak, the g.b. peak (denoted as peak 1 in the following, see Figure 4b) is expected to be shifted toward lower frequencies by at least 6 orders of magnitude, as $\sigma'_{DC,\,gb}/\sigma'_{DC,\,b} \approx 10$.[6] While in the semilog plot, see Figure 4a, only the main peak (peak 2) is seen, in the double-logarithmic representation of the data, two modulus peaks are indeed recognizable, see the arrows in Figure 4b that exemplarily point to these two peaks that belong to the curve measured at 233 K. The ratio of the peak amplitudes is given by M''_{max}(peak 2)/M''_{max}(peak 1), which, in the present case, amounts to 30−40. Of course, this value reflects the ratio $\varepsilon'_{gb}/\varepsilon'_b$ (see Figure 5a) and the ratio C_{gb}/C_b as well. Note that these values are rough estimations, as they assume Debye-like responses. In general, deviations from Debye-like behavior are seen if correlated motion or, as argued in the following, low-dimensional transport governs the electrical relaxation processes.[82,83]

Here, the most important parameter, which we deduce from the two peaks of the modulus curves shown in Figure 4b, is the characteristic relaxation rate τ_M^{-1}. It corresponds to the frequency at which the peak appears, i.e., at $M'' = M''_{max}$. In Figure 3b, $\log_{10}(\tau_{M1}^{-1})$ and $\log_{10}(\tau_{M2}^{-1})$ of the two peaks 1 and 2 are plotted vs $1000/T$. $\tau_{M2}^{-1}(1/T)$ reveals almost the same activation energy (0.35 eV) as $\sigma'_{DC,\,b}$, thus supporting our interpretation of $\sigma'_{DC,\,b}$ to represent a parameter characterizing a bulk response. The difference in activation energies is less than 0.015 eV, which is within the error range of the values. The same holds for the activation energies obtained for τ_{M1}^{-1} and $\sigma'_{DC,\,gb}$ (0.60 eV vs 0.58 eV). Note that the rates τ_M^{-1} shown in Figure 3b refer to technical frequencies ν_{max}; using angular frequencies instead ($\omega_{max} = 2\pi\,\nu_{max}$) would simply shift the Arrhenius line by an additive constant ($\log_{10}(2\pi) \approx 0.8$) upward on the $\log_{10}$ scale.

In addition to the possibility to extract characteristic relaxation rates from $M''(\nu)$ peaks, we measured the quantity M''/ω as a function of the inverse temperature at a fixed frequency.[52,84,85] M''/ω corresponds to the resistivity ρ' and is expected to pass through an electrical relaxation peak that should be parameterizable with a Lorentzian shaped function: $\rho' = M''/\omega = \tau_\rho/(1 + (\tau_\rho\omega)^\beta)$ with $1<\beta\leq 2$. Here, τ_ρ denotes the electrical relaxation time, and β is a parameter that expresses the deviation of the peak, $\log_{10}(\rho')$ vs $1/T$, from symmetric behavior. Symmetric rate peaks are obtained for β = 2; $\beta<2$, however, indicates correlated motion affecting the electrical process probed. In the case of 3D motions, the latter case would result in asymmetric peaks with the so-called low-temperature flank, showing a lower slope than the high-temperature flank. If measured at different frequencies, the rates in the latter regime are expected to coincide. This feature is indicated in Figure 5b by the dashed-dotted lines. The activation energy of the high-T flanks should correspond to E_a sensed by $\sigma_{DC\,b}$ and τ_{M2}^{-1}, which are characterized by 0.36 eV. Astonishingly, in the present case, E_a in the high-T limit ranges from only 0.06 to 0.08 eV. Moreover, the high-temperature flanks of the two peaks clearly do not coincide. As an example, at 330 K, the corresponding values M''/ω differ by more than one order of magnitude revealing a dispersive behavior of the underlying electrical relaxation function. We attribute this deviation seen by the resistivity measurements to the low-dimension, i.e., 2D ionic transport in the Li-bearing phyllosilicate $Li_{0.5}[Mg_{2.5}Li_{0.5}]Si_4O_{10}F_2$. This assignment is considered to be in analogy to the interpretation of diffusion-induced NMR spin−lattice relaxation rate $(1/T_1)$ peaks as a function of the inverse temperature at various frequencies. In the case of, e.g., the 2D Li-ion conductor Li_xTiS_2, the dispersive behavior of the NMR correlation function in the high-T, that is, the low-frequency, limit was in *quantitative* agreement with the NMR theory.[40] Although, in principle, NMR and conductivity relaxation are governed by different correlation functions,[83,86] the conclusion that the high-T flank is sensitive to the dimensionality of diffusion holds *qualitatively* also for the resistivity.

At the peak maximum, i.e., at $T = T_{max}$, the condition $\tau_\rho\omega \approx 1$ is valid. With $\nu = \omega/2\pi$ for each frequency (ν = 1.2 MHz and ν = 10.0 MHz), a rate $\tau_\rho^{-1}(1/T_{max})$ can be estimated, which we included in Figure 3b as well. τ_ρ^{-1} agrees with τ_{M2}^{-1}deduced from the $M''(\nu)$ peaks if we extrapolate the corresponding Arrhenius line toward higher temperatures. Hence, long-range ion transport in the bulk of $Li_{0.5}[Mg_{2.5}Li_{0.5}]$-$Si_4O_{10}F_2$ is given by an activation energy of 0.35 eV. This value is comparable to those energies ordinarily seen for Li^+ ionic transport in, e.g., garnet-type oxides.[10,87,88] Identifying E_a = 0.35 eV with the activation energy, which should actually be

https://dx.doi.org/10.1021/acs.chemmater.0c02460
Chem. Mater. 2020, 32, 7445−7457

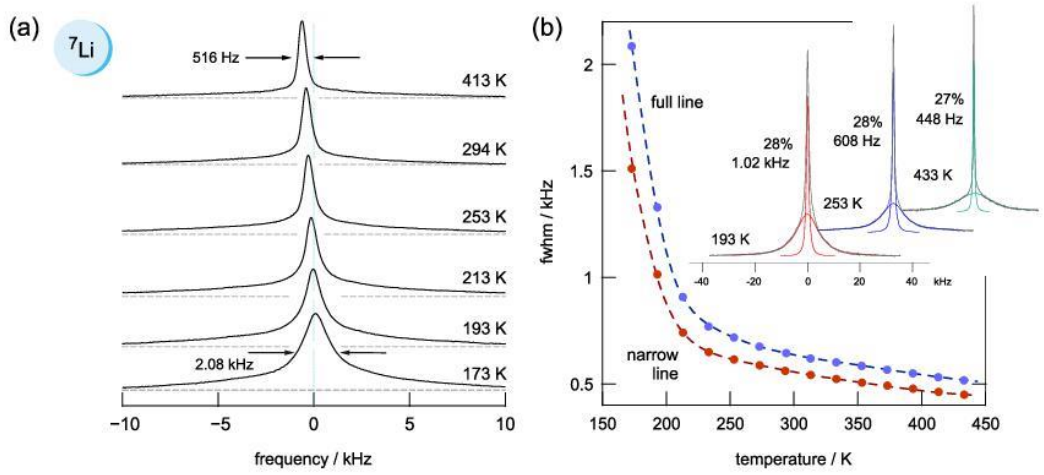

Figure 6. (a) ^{7}Li NMR line shapes recorded at the temperatures indicated. At 173 K, the fwhm of the superimposed complete line is given by 2.08 kHz. It reduces to 516 Hz at 413 K. This overall line is composed of two contributions; a deconvolution is seen in (b). In (b), the change of fwhm, either determined by using the full line shape or by analyzing the narrow component only, is shown as a function of temperature. Inset: deconvoluted ^{7}Li NMR spectra with the area of the Lorentzian (narrowed line) taking 28%, i.e., ca. 30%, of the full area under the line. See text for further explanation.

seen in the high-T regime of the $\rho'(1/T)$ peak, the parameter β would take a value of approximately 1.29, as β is given by 0.10 eV/0.35 eV = β − 1, if we adopt the analogy between conductivity and NMR relaxation more quantitatively.[5,30] In this relation, the value of 0.10 eV represents the activation energy in the low-T regime of the $\rho'(1/T)$ peak, see Figure 5b. β = 1.29 indicates rather strong ion−ion correlation effects. While such effects reduce the slope of the low-T flank, dimensionality effects will only influence the rates in the high-T regime. Semi-empirical models for 2D diffusion predict that the slope of the high-T flank should take a value that is approximately 75% of the slope in the low-T limit.[62] Here, the combination of ion−ion correlation and 2D diffusion results in apparently symmetric peak shapes even for low-dimensional dynamics. A very similar behavior has been observed earlier by Li^+ nuclear spin-relaxation in Li_xTiS_2.[40]

In conclusion, we found evidence that a 2D ionic transport is present in the phyllosilicate under study, which is governed by a rather low activation energy of only 0.35 eV. From Figure 3b, we see that the ratios $\tau_{M2}^{-1}/\tau_{M1}^{-1}$ (= τ_{M1}/τ_{M2}) and $\sigma'_{DC,\,b}/\sigma'_{DC,\,gb}$ differ by at least one order of magnitude. This observation is independent of T, as the differences in E_a for the two processes show only little change with temperature. Hence, we might have underestimated rather than overestimated the bulk ion conductivity, which we read off from the $\sigma'(\nu)$ curvatures seen in regime I (Figure 3a) by one order of magnitude. Such a rapid ionic transport process is expected to be measurable also in ^{7}Li nuclear spin relaxation. Indeed, both NMR line-shape measurements and spin-lock NMR spin−lattice relaxation rates point to temporary spin fluctuations being extremely rapid on the NMR time scale.

In Figure 6, ^{7}Li NMR line shapes are shown, which we recorded at temperatures ranging from 173 to 433 K. As can be seen in Figure 6b, the line consists of two components. A broader line with a width of ca. 12 kHz is superimposed by a narrower one whose width narrows with temperature because of increasing dipole−dipole averaging. Such averaging originates from motional processes rendering the homonuclear Li−Li dipolar interactions time dependent. The broad line can either be interpreted as a result of electric quadrupole interactions of the Li spins with nonvanishing electric field gradients or as a signal representing a group of Li ions with much lower diffusivity. As we do not recognize the emergence of a sharp quadrupole powder pattern at high temperatures, which would be in line with the universal temperature behavior of ^{7}Li NMR line shapes affected by averaging processes,[89,90] we assume that the broad line originates from a slow Li^+ subensemble. Most likely, this ensemble represents those ions sharing the same crystallographic position as Mg^{2+}. We assume that the Li ions located at 2a, i.e., between the layers, give rise to the narrow line observed.

To analyze the change in line width, we read off the fwhm of the total line; the line width as a function of temperature is shown in Figure 6. Starting from ca. 2 kHz, it reduces to values of ca. 500 Hz at 413 K, which is the so-called regime of extreme narrowing. We observe that the line width sharply increases at low temperature reaching 0.75 kHz at 250 K, at even higher temperatures, a shallower decrease is seen, which is still not fully completed at T = 450 K. To find out whether this is an exclusive feature of the overall line, we deconvoluted the lines with the help of a sum of a Lorentzian and a Gaussian function. Here, the narrow, Lorentzian-shaped line reveals the same temperature dependence as the overall line. The mainly homonuclear interactions of this line are averaged when T = 250 K is reached. Further averaging of residual couplings, likely between Li(2a) and Li(4 h), is seen at higher temperatures. Importantly, even at T = 173 K, the line has not reached its temperature-independent rigid-lattice value, i.e., rather rapid Li^+ exchange processes are present in $Li_{0.5}[Mg_{2.5}Li_{0.5}]Si_4O_{10}F_2$. We estimate that at 225 K, the associated average jump rate $1/\tau$ should be in the order of 10 kHz or higher, as full averaging will be achieved if $1/\tau$ greatly exceeds the spectral width of the NMR signal in the rigid lattice regime.

The deconvolution of the ^{7}Li NMR spectra tells us that approximately 30% (see the deconvoluted spectra shown in the inset of Figure 6b) of the total number of Li ions in $Li_{0.5}[Mg_{2.5}Li_{0.5}]Si_4O_{10}F_2$ have access to fast diffusion pathways, see the inset of Figure 6b. This value might be even higher, as

https://dx.doi.org/10.1021/acs.chemmater.0c02460
Chem. Mater. 2020, 32, 7445−7457

we cannot exclude that the broad component includes some quadrupole satellite intensities associated with the narrow line. In such a case, the value might reach 50%, which would be in line with what the chemical formula $Li_{0.5}[Mg_{2.5}Li_{0.5}]Si_4O_{10}F_2$ suggests. To shed light on this assumption, we recorded high-resolution ^{6}Li MAS NMR spectra, see Figure 7, for which first-order quadrupolar interactions and dipole−dipole broadening, both interactions being smaller for ^{6}Li anyway, are artificially averaged out through fast sample rotation. In agreement with the static line shapes, the ^{6}Li MAS line can be best approximated with a superposition of two distinct lines whereby the area under the narrow one again amounts to approximately 30%. A certain extent of Li−Mg exchange could serve as an explanation to understand the reduced spin density between the layers in $Li_{0.5}[Mg_{2.5}Li_{0.5}]Si_4O_{10}F_2$. For the sake of completeness, in Figure 7, the corresponding ^{19}F MAS NMR spectrum is shown, which reveals the two magnetically inequivalent F sites in $Li_{0.5}[Mg_{2.5}Li_{0.5}]Si_4O_{10}F_2$.

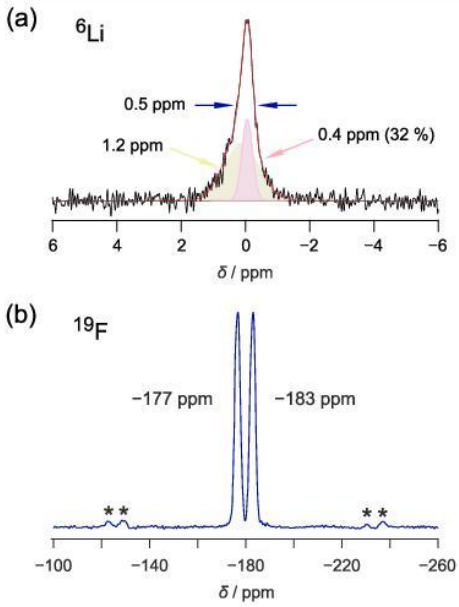

Figure 7. (a) ^{6}Li and ^{19}F MAS NMR spectra of $Li_{0.5}[Mg_{2.5}Li_{0.5}]Si_4O_{10}F_2$ recorded under ambient bearing gas conditions (300 K). The ^{6}Li MAS NMR spectrum can be best approximated with a combination of two spectral components as indicated. A deconvolution was possible with a sum of a Lorentzian line (narrow line) and a Gaussian one (broad line). Values denote line widths. Isotropic shifts were allowed to float. Approximately 32% of the Li ions, see also Figure 6b, are responsible for the narrow line. (b) In ^{19}F MAS NMR, two lines with equal intensities are seen reflecting the two magnetically inequivalent F sites in $Li_{0.5}[Mg_{2.5}Li_{0.5}]Si_4O_{10}F_2$. Asterisks mark spinning sidebands appearing at an interval of 25 kHz for each F signal.

The two-component features seen in both ^{7}Li and ^{6}Li NMR also affect the evolution of the magnetization transients, recorded in the former case, to extract diffusion-induced ^{7}Li NMR spin−lattice relaxation rates. As mentioned above, $M(t_d)$ can only be parameterized satisfactorily with a single, stretched exponential at sufficiently low temperatures (T<225 K). Above this threshold, which coincides with the beginning of the shallowly decaying part of the NMR line width (see Figure 6b), the transients start to follow a two-exponential time behavior, see also Figure S2. Therefore, we used a sum of two stretched exponentials, see the Supporting Information, to parameterize the overall transients; the same procedure, using the same terminology, is described in detail elsewhere.[31,70] The two rates $1/T_{1,slow}$ and $1/T_{1,fast}$ are shown in the Arrhenius plot of Figure 8a. The corresponding stretching exponents are displayed in the upper part of Figure 8. While $1/T_{1,slow}$ does not depend on temperature within the error limit of the analysis, $1/T_{1,fast}$ reveals a shallow diffusion-induced peak at T_{max} = 385 K. The low-T flank points to a very low activation energy of only 0.06 eV, which is likely to be dominated by strictly localized, i.e., short-range, Li^+ hopping processes and/or correlation effects.[30,32] Almost the same value was probed by the resistivity measurements, see Figure 5b.

Alternatively, we separated the two spectral contributions directly in the time domain of the underlying FIDs by individual analysis of the corresponding components that reveal quite different effective spin−spin relaxation rates. This procedure is described in detail elsewhere.[31,69,70,91] The FIDs are composed of a sharply (FID_{fast}) and a slowly decaying part (FID_{slow}), leading to two distinct rates, see Figure 7a. While the first decay reflects the broad spectral component, the latter decay, FID_{slow}, arises from the motionally narrowed component that represents fast Li^+ ions. At least for high temperatures, the rates associated with FID_{slow} agree with those obtained when analyzing the full $M(t_d)$ curves. Again, a relatively low activation energy of 0.12 eV can be estimated from the corresponding low-T flank. This value resembles that also seen in the resistivity peaks $\rho'(1/T)$ shown in Figure 5b, cf. the data recorded at 1.2 MHz. For the separated rates of the slow subensemble, a temperature independent behavior is seen for T>330 K.

To further characterize Li^+ ion hopping with methods that are also able to probe long-range ion dynamics, we performed variable-temperature spin-lock NMR measurements.[92] The corresponding $1/T_{1\rho}$ rates are shown in Figure 8b. The magnetization transients (Figure S2) do not allow for a separate investigation as it has been carried out for the $1/T_1$ measurements. Hence, they are to be regarded as averaged values. Likely, the fast Li^+ ions will dominate the overall nuclear spin response. Coming from low temperatures, the rates experience a sharp increase with temperature and pass through a maximum at T = 210 K; the maximum in$1/T_{1\rho}$ corresponds to a minimum in the stretching factor, see arrow in the upper graph of Figure 8b. The slope of the low-T flank of this prominent peak yields an activation energy of 0.39 eV, which is very similar to that seen by both conductivity spectroscopy and the modulus analysis, cf. the temperature dependence of $\sigma'_{DC,b}T$, and τ_{M2}^{-1} (Figure 3b). Thus, we found a strong indication that the peak probed by $1/T_{1\rho}$, which appeared at 205 K, reflects the same temporary fluctuations as detected by electrical relaxation. Interestingly, the activation energy of its high-T flank is comparable with those also characterizing the modulus peaks in Figure 5b. A value of 0.08 eV is also very similar to the estimated ones from $1/T_1$ NMR measurements (0.06 and 0.12 eV, see Figure 8a). Assuming a symmetric $1/T_1(1/T)$ peak, the activation energies in the high-T limit would be characterized by the same activation. In general, this similarity would be expected if the two methods probe the same (low-dimensional) diffusion process.[53] Importantly, dimensionality effects affect the slope of the NMR rate peaks in the high-T regime and yield apparent, reduced values.[32,43]

https://dx.doi.org/10.1021/acs.chemmater.0c02460
Chem. Mater. 2020, 32, 7445−7457

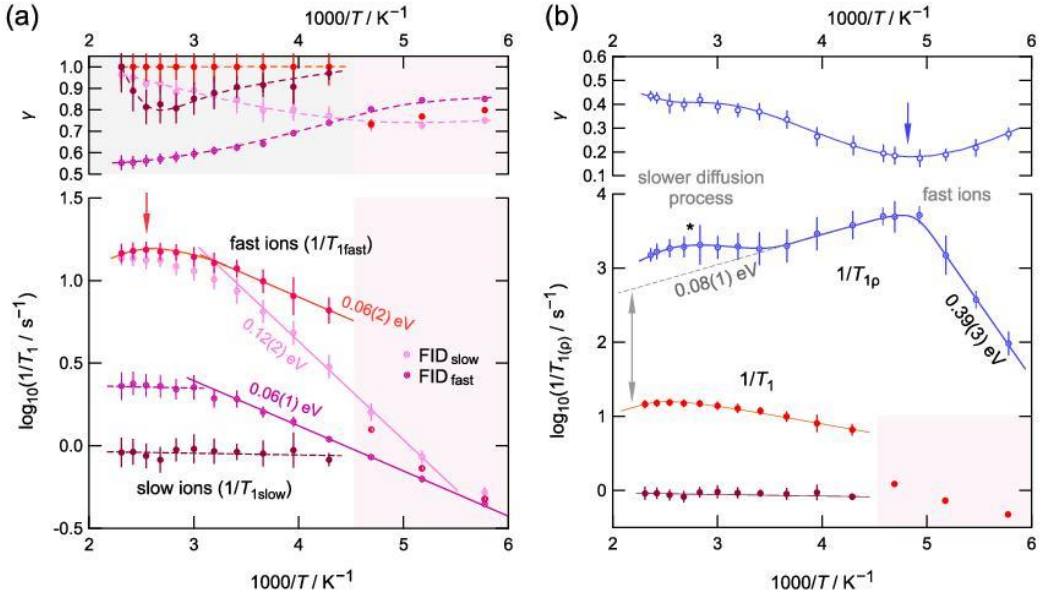

Figure 8. (a) ^{7}Li NMR spin–lattice relaxation rates of $Li_{0.5}[Mg_{2.5}Li_{0.5}]Si_4O_{10}F_2$ recorded in the laboratory frame of reference at a Larmor frequency of 116 MHz. The lower part shows an Arrhenius plot. The two-component ^{7}Li NMR line shape produces bi-exponential magnetization transients $M(t_d)$ leading to two rates $1/T_{1fast}$ and $1/T_{1slow}$ that reflect the fast and slow ions in Li-bearing fluorohectorite, also seen in ^{7}Li NMR lines. Alternatively, the stepwise analysis of the underlying FIDs also yields two relaxation rates. Stretching exponents γ are shown in the upper part of the figure. (b) Comparison of the spin-lock ^{7}Li NMR spin–lattice relaxation rates ($1/T_{1\rho}$, 20 kHz) with those measured in the laboratory frame of reference. The rate $1/T_{1\rho}$ passes through a diffusion-induced maximum at approximately 205 K. At this temperature, the corresponding γ passes through a minimum. Lines (dashed and solid) are to guide the eyes. Linear parts were analyzed with the Arrhenius law to extract the activation energies (in eV) as indicated.

In summary, electrical modulus measurements and spin-lock ^{7}Li NMR support the finding that long-range ion transport in hectorite-type $Li_{0.5}[Mg_{2.5}Li_{0.5}]Si_4O_{10}F_2$ is characterized by an activation energy of approximately 0.35 eV (see Figure 3b). In contrast to long-range transport, barriers with values of approximately 0.1 eV govern the local hopping processes. However, the values from high-T flanks, either seen in $1/T_{1\rho}$ or in $M''(\nu)$, are affected by dimensionality effects. As also recognized for the $M''(\nu)$ peaks, we observe that the rates $1/T_{1\rho}$ of the high-T flank do not coincide (see arrow in Figure 8b), with those expected from $1/T_1$ as is indicated by the dashed line in Figure 8b. This line extrapolates the high-T flank to even higher temperatures. The same feature is seen in Figure 5b. This dispersive behavior strongly supports our idea about 2D diffusion in the synthetic hectorite studied. Finally, $1/T_{1\rho}(1/T)$ revealed a second peak appearing at T_{max} = 350 K (marked by a star in Figure 8b), which, most likely, is to be assigned to the low translational ion mobility of the Li^+ ions sharing sites with Mg^{2+} in the layers of the phyllosilicate.

To directly compare the different responses seen by NMR and electrical relaxation, we finally estimated Li^+ jump rates from the maxima seen in $1/T_1$ and $1/T_{1\rho}$ at T_{max} = 385 K and T_{max} = 205 K, respectively, by using the maximum condition $\tau_{NMR}\omega_{0(1)} \approx 1$. The rates obtained are included in Figure 9. In the present case, they agree very well with those from electrical measurements. At 293 K, the Arrhenius line yields a mean jump rate $1/\tau$ of approximately 3×10^7 s^{-1}, which translates into a 2D diffusion coefficient $D_{2D} = a^2/(4\tau)$ of 4.7×10^{-13} m^2 s^{-1} if we use $a \approx 2.5$ Å. The crystallographic Li–Li distance is ca. 5 Å, which we think is too large for a single Li^+ jump. Assuming temporarily occupied interstitial positions connecting two or more regular sites in a distance of 2.5 Å seems to be more reasonable. $D = 4.7 \times 10^{-13}$ m^2 s^{-1} would indeed correspond to an estimated ionic conductivity $\sigma_{est.}$, almost reaching the order of 0.1 mS cm^{-1} if we use the (idealized) cell

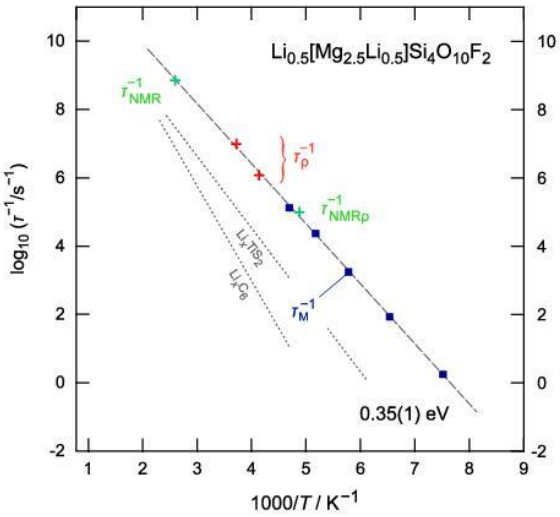

Figure 9. Arrhenius plot of the Li^+ hopping rates $1/\tau$ deduced from both nuclear spin relaxation and electrical relaxation taking advantage of the modulus representation and resistivity measurements, see Figure 3. Data from NMR, if restricted to the maxima of the spin–lattice relaxation rate peaks, agree well with the results from broadband electrical characterization. The dashed line represents a linear fit yielding 0.35(1) eV. For comparison, jump rates measured for Li_xTiS_2 (x = 0.7, 0.41 eV)[43] and Li_xC_6 (x = 1, 0.55 eV)[38] are also shown, see dotted lines.

https://dx.doi.org/10.1021/acs.chemmater.0c02460
Chem. Mater. 2020, 32, 7445−7457

volume of 490 Å^3 to estimate a charge carrier concentration of ca. $N^1 = 2 \times 10^{27}$ m^{-3}. $\sigma_{est.}$ is related to D_{NE} via the Nernst-Einstein relation, which reads in general $D_{NE} = \sigma k_B T/(N^1 q)$, with q being the charge of the Li^+ ions. We assumed that D_{2D} and D_{NE} are connected by $D_{2D} = (H_R/f)D_{NE}$ with H_R being the Haven ratio and f denoting the correlation factor. Our estimation anticipated H_R/f being of the order of unity. Taking into account that only 30% of the ions participate in Li^+ long-range ion transport, $D_{2D} = (H_R/f)D_{NE}$ is fulfilled if we chose $H_R/f \approx 0.3$. The relatively high value of D_{2D} obtained clearly renders hectorite as a fast ion conductor.

Rapid ion exchange in $Li_{0.5}[Mg_{2.5}Li_{0.5}]Si_4O_{10}F_2$ benefits from a wide interlayer gap giving the ions the necessary space to freely diffuse in the phyllosilicate. To the best of our knowledge, this is the first time that such high cation diffusivities were probed in a synthetic clay mineral. For comparison, in Figure 9, we included jump rates of two other 2D materials, Li_xTiS_2 (0.41 eV)[43] and LiC_6 (0.55 eV),[38] studied by NMR (and other methods) earlier. Inspired by the present results, one might think about crystal-chemical modifications that could lead to even higher diffusivities. Nature may offer a range of further silicate structures, including also layered ones, from which the necessary inspiration can be drawn to develop both powerful electrolytes and active materials for, e.g., lithium-ion batteries. Exemplarily, the Khan group studied hectorite-containing composite materials for this purpose.[56−59]

4. CONCLUSIONS

Li^+ ion diffusion and electrical transport in the hectorite-type phyllosilicate $Li_{0.5}[Mg_{2.5}Li_{0.5}]Si_4O_{10}F_2$ was studied by broad-band conductivity spectroscopy, modulus analysis, and ^{7}Li NMR spin−lattice relaxation measurements. Electrical and nuclear spin relaxation confirmed our hypothesis of rapid interlayer (2D) Li^+ exchange processes in the silicate. This process is characterized by an overall activation energy of approximately 0.35 eV. Under ambient conditions, conductivity spectroscopy points to an ionic conductivity as high as 0.14 mS cm^{-1}, representing a favorable starting point for further improvements by crystal-chemical engineering. In addition, we derived a consistent picture of Li^+ ion dynamics and showed that the electric and magnetic fluctuations probed originate from the same translational process. Our study supports the general idea that spatial confinement, able to guide the charge carriers over long distances, is helpful in enabling fast ion transport.

■ ASSOCIATED CONTENT

Supporting Information

The Supporting Information is available free of charge at https://pubs.acs.org/doi/10.1021/acs.chemmater.0c02460.

Simulated X-ray powder diffraction; ^{7}Li NMR magnetization transients from which the spin−lattice relaxation rates were extracted (PDF).

■ AUTHOR INFORMATION

Corresponding Authors

Paul Heitjans − *Institute of Physical Chemistry and Electrochemistry, Leibniz University Hannover, Hannover 30167, Germany;* orcid.org/0000-0003-1563-9176; Email: heitjans@pci.uni-hannover.de

H. Martin. R. Wilkening − *Institute for Chemistry and Technology of Materials, and Christian Doppler Laboratory for Lithium Batteries, Graz University of Technology, Graz 8010, Austria; Alistore−ERI European Research Institute, Amiens F-80039, France;* orcid.org/0000-0001-9706-4892; Email: wilkening@tugraz.at

Authors

Caroline Hiebl − *Institute for Chemistry and Technology of Materials, and Christian Doppler Laboratory for Lithium Batteries, Graz University of Technology, Graz 8010, Austria*

Patrick Loch − *Department of Chemistry and Bavarian Center for Battery Technology, University of Bayreuth, Bayreuth 95447, Germany*

Marina Brinek − *Institute for Chemistry and Technology of Materials, and Christian Doppler Laboratory for Lithium Batteries, Graz University of Technology, Graz 8010, Austria*

Maria Gombotz − *Institute for Chemistry and Technology of Materials, and Christian Doppler Laboratory for Lithium Batteries, Graz University of Technology, Graz 8010, Austria*

Bernhard Gadermaier − *Institute for Chemistry and Technology of Materials, and Christian Doppler Laboratory for Lithium Batteries, Graz University of Technology, Graz 8010, Austria;* orcid.org/0000-0003-2917-1818

Josef Breu − *Department of Chemistry and Bavarian Center for Battery Technology, University of Bayreuth, Bayreuth 95447, Germany;* orcid.org/0000-0002-2547-3950

Complete contact information is available at: https://pubs.acs.org/10.1021/acs.chemmater.0c02460

Author Contributions

#C.H. and M.B. contributed equally to this work.

Notes

The authors declare no competing financial interest.

■ ACKNOWLEDGMENTS

We thank the German Science Foundation (Deutsche Forschungsgemeinschaft (DFG)) for financial support (research unit FOR1277). Moreover, financial support from the Austrian Federal Ministry of Science, Research and Economy (BMWFW) and the National Foundation for Research, Technology and Development (CD-Laboratory of Lithium Batteries: Ageing Effects, Technology and New Materials) is gratefully acknowledged. The work also received funding from the European H2020 Framework program, no. 769929. P.H. is grateful to the State of Lower Saxony (Germany) for the Niedersachsen Professorship 'Mobility of Ions in Solids'.

■ REFERENCES

(1) Fergus, J. W. A review of electrolyte and electrode materials for high temperature electrochemical CO_2 and SO_2 gas sensors. *Sens. Actuators B Chem.* **2008**, *134*, 1034−1041.

(2) Fergus, J. W. Sensing mechanism of non-equilibrium solid-electrolyte-based chemical sensors. *J. Solid State Electrochem.* **2011**, *15*, 971−984.

(3) Rehman, A.; Zeng, X. Q. Ionic Liquids as Green Solvents and Electrolytes for Robust Chemical Sensor Development. *Acc. Chem. Res.* **2012**, *45*, 1667−1677.

(4) Gao, Z.; Sun, H.; Fu, L.; Ye, F.; Zhang, Y.; Luo, W.; Huang, Y. Promises, Challenges, and Recent Progress of Inorganic Solid-State Electrolytes for All-Solid-State Lithium Batteries. *Adv. Mater.* **2018**, *30*, 1705702.

(5) Uitz, M.; Epp, V.; Bottke, P.; Wilkening, M. Ion Dynamics in Solid Electrolytes for Lithium Batteries. *J. Electroceram.* **2017**, *38*, 142−156.
(6) Epp, V.; Wilkening, M. In *Handbook of Solid State Batteries*; Dudney, N. J.; West, W. C.; Nanda, J., Eds. World Scientific: Singapore, 2015; pp. 133−190.
(7) Lotsch, B. V.; Maier, J. Relevance of solid electrolytes for lithium-based batteries: A realistic view. *J. Electroceram.* **2017**, *38*, 128−141.
(8) Zhang, Z.; Shao, Y.; Lotsch, B.; Hu, Y.-S.; Li, H.; Janek, J.; Nazar, L. F.; Nan, C.-W.; Maier, J.; Armand, M.; Chen, L. New Horizons for Inorganic Solid State Ion Conductors. *Energy Environ. Sci.* **2018**, *11*, 1945−1976.
(9) Bachman, J. C.; Muy, S.; Grimaud, A.; Chang, H. H.; Pour, N.; Lux, S. F.; Paschos, O.; Maglia, F.; Lupart, S.; Lamp, P.; Giordano, L.; Shao-Horn, Y. Inorganic Solid-State Electrolytes for Lithium Batteries: Mechanisms and Properties Governing Ion Conduction. *Chem. Rev.* **2016**, *116*, 140−162.
(10) Thangadurai, V.; Narayanan, S.; Pinzaru, D. Garnet-type solid-state fast Li ion conductors for Li batteries: critical review. *Chem. Soc. Rev.* **2014**, *43*, 4714−4727.
(11) Chen, S.; Xie, D.; Liu, G.; Mwizerwa, J. P.; Zhang, Q.; Zhao, Y.; Xu, X.; Yao, X. Sulfide solid electrolytes for all-solid-state lithium batteries: structure, conductivity, stability and application. *Energy Storage Mater.* **2018**, *14*, 58−74.
(12) Janski, R.; Fugger, M.; Forster, M.; Sorger, M.; Dunst, A.; Hanzu, I.; Sternad, M.; Wilkening, M. Lithium barrier materials for on-chip Si-based microbatteries. *J. Mater. Sci. Mater. Electron.* **2017**, *28*, 14605−14614.
(13) Johnson, C. E.; Noda, K.; Roux, N. Ceramic breeder materials: Status and needs. *J. Nucl. Mater.* **1998**, *258-263*, 140−148.
(14) Roux, N.; Tanaka, S.; Johnson, C.; Verrall, R. Ceramic breeder material development. *Fusion Eng. Des.* **1998**, *41*, 31−38.
(15) Tang, T.; Zhang, Z.; Meng, J. B.; Luo, D. L. Synthesis and characterization of lithium silicate powders. *Fusion Eng. Des.* **2009**, *84*, 2124−2130.
(16) Quartarone, E.; Mustarelli, P. Electrolytes for solid-state lithium rechargeable batteries: recent advances and perspectives. *Chem. Soc. Rev.* **2011**, *40*, 2525−2540.
(17) Manthiram, A.; Yu, X.; Wang, S. Lithium battery chemistries enabled by solid-state electrolytes. *Nat. Rev. Mater.* **2017**, *2*, 16103.
(18) Zhang, B.; Tan, R.; Yang, L.; Zheng, J.; Zhang, K.; Mo, S.; Lin, Z.; Pan, F. Mechanisms and properties of ion-transport in inorganic solid electrolytes. *Energy Storage Mater.* **2018**, *10*, 139−159.
(19) Zheng, F.; Kotobuki, M.; Song, S.; Lai, M. O.; Lu, L. Review on solid electrolytes for all-solid-state lithium-ion batteries. *J. Power Sources* **2018**, *389*, 198−213.
(20) Ohno, S.; Bernges, T.; Buchheim, J.; Duchardt, M.; Hatz, A.-K.; Kraft, M. A.; Kwak, H.; Santhosha, A. L.; Liu, Z.; Minafra, N.; Tsuji, F.; Sakuda, A.; Schlem, R.; Xiong, S.; Zhang, Z.; Adelhelm, P.; Chen, H.; Hayashi, A.; Jung, Y. S.; Lotsch, B. V.; Roling, B.; Vargas-Barbosa, N. M.; Zeier, W. G. How Certain Are the Reported Ionic Conductivities of Thiophosphate-Based Solid Electrolytes? An Interlaboratory Study. *ACS Energy Lett.* **2020**, *5*, 910−915.
(21) Jay, E. E.; Rushton, M. J. D.; Chroneos, A.; Grimes, R. W.; Kilner, J. A. Genetics of superionic conductivity in lithium lanthanum titanates. *Phys. Chem. Chem. Phys.* **2015**, *17*, 178−183.
(22) Wang, Y.; Richards, W. D.; Ong, S. P.; Miara, L. J.; Kim, J. C.; Mo, Y.; Ceder, G. Design Principles for Solid-State Lithium Superionic Conductors. *Nat. Mater.* **2015**, *14*, 1026−1031.
(23) Richards, W. D.; Tsujimura, T.; Miara, L. J.; Wang, Y.; Kim, J. C.; Ong, S. P.; Uechi, I.; Suzuki, N.; Ceder, G. Design and Synthesis of the Superionic Conductor $Na_{10}SnP_2S_{12}$. *Nat. Commun.* **2016**, *7*, 1026−1031.
(24) He, X.; Zhu, Y.; Mo, Y. Origin of Fast Ion Diffusion in Superionic Conductors. *Nat. Commun.* **2017**, *8*, 15893.
(25) Di Stefano, D.; Miglio, A.; Robeyns, K.; Filinchuk, Y.; Lechartier, M.; Senyshyn, A.; Ishida, H.; Spannenberger, S.; Prutsch, D.; Lunghammer, S.; Rettenwander, D.; Wilkening, M.; Roling, B.; Kato, Y.; Hautier, G. Superionic Diffusion through Frustrated Energy Landscape. *Chem* **2019**, *5*, 2450−2460.
(26) Duvel, A.; Heitjans, P.; Fedorov, P.; Scholz, G.; Cibin, G.; Chadwick, A. V.; Pickup, D. M.; Ramos, S.; Sayle, L. W. L.; Sayle, E. K. L.; Sayle, T. X. T.; Sayle, D. C. Is Geometric Frustration-Induced Disorder a Recipe for High Ionic Conductivity? *J. Am. Chem. Soc.* **2017**, *139*, 5842−5848.
(27) Whittingham, M. S. Lithium Batteries and Cathode Materials. *Chem. Rev.* **2004**, *104*, 4271−4302.
(28) Whittingham, M. S. Inorganic Nanomaterials for Batteries. *Dalton Trans.* **2008**, 5424−5431.
(29) Epp, V.; Wilkening, M. Fast Li Diffusion in Crystalline $LiBH_4$ due to Reduced Dimensionality: Frequency-Dependent NMR Spectroscopy. *Phys. Rev. B* **2010**, *82*, 020301.
(30) Heitjans, P.; Schirmer, A.; Indris, S. NMR and β-NMR Studies of Diffusion in Interface-Dominated and Disordered Solids. In *Diffusion in Condensed Matter − Methods, Materials, Models*, Heitjans, P.; Kärger, J., Eds. Springer: Berlin, 2005; pp. 367−415.
(31) Heitjans, P.; Wilkening, M. Ion dynamics at interfaces: nuclear magnetic resonance studies. *Mater. Res. Bull.* **2009**, *34*, 915−922.
(32) Wilkening, M.; Heitjans, P. From Micro to Macro: Access to Long-Range Li^+ Diffusion Parameters in Solids via Microscopic ^6Li, ^7Li Spin-Alignment Echo NMR Spectroscopy. *Chem. Phys. Chem.* **2012**, *13*, 53−65.
(33) Kuhn, A.; Kunze, M.; Sreeraj, P.; Wiemhöfer, H. D.; Thangadurai, V.; Wilkening, M.; Heitjans, P. NMR Relaxometry as a Versatile Tool to Study Li Ion Dynamics in Potential Battery Materials. *Solid State Nucl. Magn. Reson.* **2012**, *42*, 2−8.
(34) McDowell, A. F.; Mendelsohn, C. F.; Conradi, M. S.; Bowman, R. C.; Maeland, A. J. 2-Dimensional Diffusion of Hydrogen in $ZrBe_2H_{1.4}$. *Phys. Rev. B* **1995**, *51*, 6336−6342.
(35) Vinod Chandran, C.; Heitjans, P. Solid-State NMR Studies of Lithium Ion Dynamics Across Materials Classes. *Annu. Rep. NMR Spectrosc.* **2016**, *89*, 1−102.
(36) Volgmann, K.; Epp, V.; Langer, J.; Stanje, B.; Heine, J.; Nakhal, S.; Lerch, M.; Wilkening, M.; Heitjans, P. Solid-State NMR to Study Translational Li Ion Dynamics in Solids with Low-Dimensional Diffusion Pathways. *Z. Phys. Chem. (NF)* **2017**, *231*, 1215−1241.
(37) Freiländer, P.; Heitjans, P.; Ackermann, H.; Bader, B.; Kiese, G.; Schirmer, A.; Stöckmann, H.-J.; Van der Marel, C.; Magerl, A.; Zabel, H. Diffusion-Processes in LiC_6 Studied by β-NMR. *Z. Phys. Chem. (NF)* **1987**, *151*, 93−101.
(38) Langer, J.; Epp, V.; Heitjans, P.; Mautner, F. A.; Wilkening, M. Lithium motion in the anode material LiC_6 as seen via time-domain ^7Li NMR. *Phys. Rev. B* **2013**, *88*, No. 094304.
(39) Winter, R.; Heitjans, P. Li^+ diffusion and its structural basis in the nanocrystalline and amorphous forms of two-dimensionally ion-conducting Li_xTiS_2. *J. Phys. Chem. B* **2001**, *105*, 6108−6115.
(40) Küchler, W.; Heitjans, P.; Payer, A.; Schöllhorn, R. ^7Li NMR relaxation by diffusion in hexagonal and cubic Li_xTiS_2. *Solid State Ionics* **1994**, *70-71*, 434−438.
(41) Wilkening, M.; Heitjans, P. Ultraslow diffusion in polycrystalline *h*-$LiTiS_2$ studied by ^7Li spin-alignment echo NMR spectroscopy. *Def. Diff. Forum* **2005**, *237-240*, 1182−1187.
(42) Wilkening, M.; Küchler, W.; Heitjans, P. From ultraslow to fast lithium diffusion in the 2D ion conductor $Li_{0.7}TiS_2$ probed directly by stimulated-echo NMR and nuclear magnetic relaxation. *Phys. Rev. Lett.* **2006**, *97*, 065901.
(43) Wilkening, M.; Heitjans, P. Li jump process in *h*-$Li_{0.7}TiS_2$ studied by two-time ^7Li spin-alignment echo NMR and comparison with results on two-dimensional diffusion from nuclear magnetic relaxation. *Phys. Rev. B* **2008**, *77*, No. 024311.
(44) Epp, V.; Nakhal, S.; Lerch, M.; Wilkening, M. Two-dimensional diffusion in $Li_{0.7}NbS_2$ as directly probed by frequency-dependent ^7Li NMR. *J. Phys. Condes. Matter.* **2013**, *25*, 195402.
(45) Stanje, B.; Epp, V.; Nakhal, S.; Lerch, M.; Wilkening, M. Li ion dynamics along the inner surfaces of layer-structured 2H-Li_xNbS_2. *ACS Appl. Mater. Interfaces* **2015**, *7*, 4089−4099.

https://dx.doi.org/10.1021/acs.chemmater.0c02460
Chem. Mater. 2020, 32, 7445−7457

(46) Langer, J.; Epp, V.; Sternad, M.; Wilkening, M. Diffusion-induced ^{7}Li NMR relaxation of layer-structured tin disulphide - Li diffusion along the buried interfaces in $Li_{0.17}SnS_2$. *Solid State Ionics* **2015**, *276*, 56−61.
(47) Epp, V.; Wilkening, M. Motion of Li^+ in nanoengineered $LiBH_4$ and $LiBH_4$:Al_2O_3 comparison with the microcrystalline form. *Chem. Phys. Chem.* **2013**, *14*, 3706−3713.
(48) Gombotz, M.; Lunghammer, S.; Breuer, S.; Hanzu, I.; Preishuber-Pflügl, F.; Wilkening, H. M. R. Spatial confinement - rapid 2D F^- diffusion in micro- and nanocrystalline $RbSn_2F_5$. *Phys. Chem. Chem. Phys.* **2019**, *21*, 1872−1883.
(49) Kuhn, A.; Sreeraj, P.; Pöttgen, R.; Wiemhöfer, H. D.; Wilkening, M.; Heitjans, P. Li Ion Diffusion in the Anode Material $Li_{12}Si_7$: Ultrafast Quasi-1D Diffusion and Two Distinct fast 3D Jump Processes Separately Revealed by ^{7}Li NMR Relaxometry. *J. Am. Chem. Soc.* **2011**, *133*, 11018−11021.
(50) Kuhn, A.; Dupke, S.; Kunze, M.; Puravankara, S.; Langer, T.; Pöttgen, R.; Winter, M.; Wiemhöfer, H. D.; Eckert, H.; Heitjans, P. Insight into the Li Ion Dynamics in $Li_{12}Si_7$: Combining Field Gradient Nuclear Magnetic Resonance, One- and Two-Dimensional Magic-Angle Spinning Nuclear Magnetic Resonance, and Nuclear Magnetic Resonance Relaxometry. *J. Phys. Chem. C* **2014**, *118*, 28350−28360.
(51) Nakhal, S.; Wiedemann, D.; Stanje, B.; Dolotko, O.; Wilkening, M.; Lerch, M. $LiBi_3S_5$ - A lithium bismuth sulfide with strong cation disorder. *J. Solid State Chem.* **2016**, *238*, 60−67.
(52) Preishuber-Pflügl, F.; Bottke, P.; Pregartner, V.; Bitschnau, B.; Wilkening, M. Correlated fluorine diffusion and ionic conduction in the nanocrystalline F^- solid electrolyte $Ba_{0.6}La_{0.4}F_{2.4}$ - ^{19}F T_{1r} NMR relaxation vs. conductivity measurements. *Phys. Chem. Chem. Phys.* **2014**, *16*, 9580−9590.
(53) Kuhn, A.; Narayanan, S.; Spencer, L.; Goward, G.; Thangadurai, V.; Wilkening, M. Li Self-Diffusion in Garnet-Type $Li_7La_3Zr_2O_{12}$ as Probed Directly by Diffusion-Induced ^{7}Li Spin-Lattice Relaxation NMR Spectroscopy. *Phys. Rev. B* **2011**, *83*, No. 094302.
(54) Breu, J.; Seidl, W.; Stoll, A. J.; Lange, K. G.; Probst, T. U. Charge homogeneity in synthetic fluorohectorite. *Chem. Mater.* **2001**, *13*, 4213−4220.
(55) Anthony, J. W., *Handbook of Mineralogy*. Mineral Data Pub.: Tucson, Ariz., 1990.
(56) Riley, M.; Fedkiw, P. S.; Khan, S. A. Transport Properties of Lithium Hectorite-Based Composite Electrolytes. *J. Electrochem. Soc.* **2002**, *149*, A667.
(57) Riley, M. W.; Fedkiw, P. S.; Khan, S. A. Lithium Hectorite Clay as the Ionic Conductor in $LiCoO_2$ Cathodes. *J. Electrochem. Soc.* **2003**, *150*, A933.
(58) Walls, H. J.; Riley, M. W.; Singhal, R. R.; Spontak, R. J.; Fedkiw, P. S.; Khan, S. A. Nanocomposite Electrolytes with Fumed Silica and Hectorite Clay Networks: Passive versus Active Fillers. *Adv. Funct. Mater.* **2003**, *13*, 710−717.
(59) Singhal, R. G.; Capracotta, M. D.; Martin, J. D.; Khan, S. A.; Fedkiw, P. S. Transport properties of hectorite based nanocomposite single ion conductors. *J. Power Sources* **2004**, *128*, 247−255.
(60) Yu, C.; Ganapathy, S.; de Klerk, N. J. J.; Roslon, I.; van Eck, E. R. H.; Kentgens, A. P. M.; Wagemaker, M. Unravelling Li-Ion Transport from Picoseconds to Seconds: Bulk versus Interfaces in an Argyrodite Li_6PS_5Cl-Li_2S All-Solid-State Li-Ion Battery. *J. Am. Chem. Soc.* **2016**, *138*, 11192−11201.
(61) Ganapathy, S.; Yu, C.; van Eck, E. R. H.; Wagemaker, M. Peeking across Grain Boundaries in a Solid-State Ionic Conductor. *ACS Energy Lett.* **2019**, *4*, 1092−1097.
(62) Richards, P. M., Magnetic Resonance in Superionic Conductors. In *Physics of Superionic Conductors*; Salamon, M. B., Ed., Topics in Current Physics, *Vol 15*, Springer: Berlin, 1979; pp. 141−(174) .
(63) Stöter, M.; Kunz, D. A.; Schmidt, M.; Hirsemann, D.; Kalo, H.; Putz, B.; Senker, J.; Breu, J. Nanoplatelets of Sodium Hectorite Showing Aspect Ratios of approximate to 20 000 and Superior Purity. *Langmuir* **2013**, *29*, 1280−1285.
(64) Rosenfeldt, S.; Stöter, M.; Schlenk, M.; Martin, T.; Albuquerque, R. Q.; Förster, S.; Breu, J. In-Depth Insights into the Key Steps of Delamination of Charged 2D Nanomaterials. *Langmuir* **2016**, *32*, 10582−10588.
(65) Daab, M.; Eichstaedt, N. J.; Edenharter, A.; Rosenfeldt, S.; Breu, J. Layer charge robust delamination of organo-clays. *RSC Adv.* **2018**, *8*, 28797−28803.
(66) Daab, M.; Eichstaedt, N. J.; Habel, C.; Rosenfeldt, S.; Kalo, H.; Schiebling, H.; Förster, S.; Breu, J. Onset of Osmotic Swelling in Highly Charged Clay Minerals. *Langmuir* **2018**, *34*, 8215−8222.
(67) Fukushima, E.; Roeder, S. B. W., *Experimental Pulse NMR. A Nuts and Bolts Approach*. Addison-Wesley Publ. Comp.: Reading, 1981.
(68) Look, D. C.; Lowe, I. J. Nuclear Magnetic Dipole-Dipole Relaxation along Static and Rotating Magnetic Fields - Application to Gypsum. *J. Chem. Phys.* **1966**, *44*, 2995−3000.
(69) Indris, S.; Heitjans, P. Heterogeneous ^{7}Li NMR Relaxation in Nanocrystalline Li_2O:B_2O_3 Composites. *J. Non-Cryst. Solids* **2002**, *307-310*, 555−564.
(70) Wilkening, M.; Indris, S.; Heitjans, P. Heterogeneous Lithium Diffusion in Nanocrystalline Li_2O:Al_2O_3 Composites. *Phys. Chem. Chem. Phys.* **2003**, *5*, 2225−2231.
(71) Kalo, H.; Müller, M. W.; Kunz, D. A.; Breu, J. How to maximize the aspect ratio of clay nanoplatelets. *Nanoscale* **2012**, *4*, 5633−5639.
(72) Gast, R. G.; Klobe, W. D. Sodium-Lithium Exchange Equilibria on Vermiculite at 25 Degrees and 50 Degrees C. *Clays Clay Miner.* **1971**, *19*, 311−319.
(73) Mermut, A. R.; Lagaly, G. Baseline studies of The Clay Minerals Society Source Clays: Layer-charge determination and characteristics of those minerals containing 2 : 1 layers. *Clays Clay Miner.* **2001**, *49*, 393−397.
(74) Kalo, H.; Milius, W.; Breu, J. Single crystal structure refinement of one- and two-layer hydrates of sodium fluorohectorite. *RSC Adv.* **2012**, *2*, 8452−8459.
(75) Irvine, J. T. S.; Sinclair, D. C.; West, A. R. Electroceramics: Characterization by Impedance Spectroscopy. *Adv. Mater.* **1990**, *2*, 132−138.
(76) Macdonald, J. R. Nearly Constant Loss or Constant Loss in Ionically Conducting Glasses: A Physically Realizable Approach. *J. Chem. Phys.* **2001**, *115*, 6192−6199.
(77) Funke, K.; Ross, I.; Banhatti, R. D. Nearly constant loss behavior in g-$RbAg_4I_5$: microwave conductivity plateau identified. *Solid State Ionics* **2004**, *175*, 819−822.
(78) Laughman, D. M.; Banhatti, R. D.; Funke, K. Nearly Constant Loss Effects in Borate Glasses. *Phys. Chem. Chem. Phys.* **2009**, *11*, 3158−3167.
(79) Laughman, D. M.; Banhatti, R. D.; Funke, K. New Nearly Constant Loss Feature Detected in Glass at Low Temperatures. *Phys. Chem. Chem. Phys.* **2010**, *12*, 14102−14108.
(80) Banhatti, R. D.; Laughman, D.; Badr, L.; Funke, K. Nearly Constant Loss Effect in Sodium Borate and Silver Meta-phosphate Glasses: New Insights. *Solid State Ionics* **2011**, *192*, 70−75.
(81) Rizos, A. K.; Alifragis, J.; Ngai, K. L.; Heitjans, P. Near constant loss in glassy and crystalline $LiAlSi_2O_6$ from conductivity relaxation measurements. *J. Chem. Phys.* **2001**, *114*, 931−934.
(82) Ngai, K. L., *Relaxation and Diffusion in Complex Systems*. Springer: New York, 2011, DOI: 10.1007/978-1-4419-7649-9.
(83) Habasaki, J.; León, C.; Ngai, K. L., *Dynamics of Glassy, Crystalline and Liquid Ionic Conductors*. Springer: New York, 2017; *132*.
(84) Munro, B.; Schrader, M.; Heitjans, P. AC Impedance Studies of Glassy and Crystalline Lithium Aluminosilicate Compounds. *Ber. Bunsenges. Phys. Chem. Chem. Phys.* **1992**, *96*, 1718−1723.
(85) Winter, R.; Siegmund, K.; Heitjans, P. Nuclear magnetic and conductivity relaxations by Li diffusion in glassy and crystalline $LiAlSi_4O_{10}$. *J. Non-Cryst. Solids* **1997**, *212*, 215−224.

https://dx.doi.org/10.1021/acs.chemmater.0c02460
Chem. Mater. 2020, 32, 7445−7457

(86) Bunde, A.; Dieterich, W.; Maass, P.; Meyer, M., Ionic Transport in Disordered Materials. In *Diffusion in Condensed Matter - Methods, Materials, Models*, Heitjans, P.; Kärger, J., Eds. Springer: Berlin, 2005; pp. 813−856.
(87) Buschmann, H.; Dölle, J.; Berendts, S.; Kuhn, A.; Bottke, P.; Wilkening, M.; Heitjans, P.; Senyshyn, A.; Ehrenberg, H.; Lotnyk, A.; Duppel, V.; Kienle, L.; Janek, J. Structure and Dynamics of the Fast Lithium Ion Conductor "$Li_7La_3Zr_2O_{12}$". *Phys. Chem. Chem. Phys.* **2011**, *13*, 19378−19392.
(88) Posch, P.; Lunghammer, S.; Berendts, S.; Ganschow, S.; Redhammer, G. J.; Wilkening, A.; Lerch, M.; Gadermaier, B.; Rettenwander, D.; Wilkening, H. M. R. Ion dynamics in Al-Stabilized $Li_7La_3Zr_2O_{12}$ single crystals - Macroscopic transport and the elementary steps of ion hopping. *Energy Storage Mater.* **2020**, *24*, 220−228.
(89) Bertermann, R.; Müller-Warmuth, W. Universality of NMR results in LISICON systems and other solid lithium conductors. *Z. Naturforsch. A J. Phys. Sci.* **1998**, *53*, 863−873.
(90) Bertermann, R.; Müller-Warmuth, W.; Jansen, C.; Hiltmann, F.; Krebs, B. NMR studies of the lithium dynamics in two thioborate superionic conductors: $Li_9B_{19}S_{33}$ and $Li_{4-2x}Sr_{2+x}B_{10}S_{19}$. *Solid State Ionics* **1999**, *117*, 245−255.
(91) Breuer, S.; Uitz, M.; Wilkening, H. M. R. Rapid Li Ion Dynamics in the Interfacial Regions of Nanocrystalline Solids. *J. Phys. Chem. Lett.* **2018**, *9*, 2093−2097.
(92) Epp, V.; Gün, Ö.; Deiseroth, H.-J.; Wilkening, M. Long-Range Li^+ Dynamics in the Lithium Argyrodite Li_7PSe_6 as Probed by Rotating-Frame Spin-Lattice Relaxation NMR. *Phys. Chem. Chem. Phys.* **2013**, *15*, 7123−7132.

https://dx.doi.org/10.1021/acs.chemmater.0c02460
Chem. Mater. 2020, 32, 7445−7457

4 Conclusion and Outlook

The main topic of the present doctoral thesis was the investigation of the ion dynamics of different classes of solid-state electrolyte materials concerning structural influences. As shown in chapter (2.2) a variety of promising inorganic solid electrolytes exist. However, many challenges concerning their fabrication, ionic conductivity and stability still remain. To improve the engineering of those materials, knowledge about the influence of their structure on the ionic conductivity is essential.

Here, the model substances included the halide-containing thiophosphate Li_6PS_5I and the synthetic hectorite $Li_{0.5}[Mg_{2.5}Li_{0.5}]Si_4O_{10}F_2$. The polycrystalline samples were analyzed by means of nuclear magnetic resonance, conductivity spectroscopy, electric modulus analysis and x-ray diffraction. The scope of these studies was to gain insight into structure-conductivity relationships within thiophosphate and hectorite samples. The combination of various techniques allowed for the investigation of the lithium ion mobility over a wide temperature range and length scale. The results of these studies were published in peer-reviewed journals. The articles can be found in chapter (3).

The first two publications focused on the study of the ionic transport in the lithium containing halide thiophosphate Li_6PS_5I. Here, a micrometer sized material, derived via a solid-state reaction, was chosen for further treatment and investigations. As those former studies showed a much lower lithium ion conductivity for Li_6PS_5I than for its bromide and chloride analogues, an attempt to enhance its ionic conductivity by a mechanical treatment was made.

High energy ball milling of the micrometer sized starting material for a duration of only two hours at 400 rpm yielded nanometer sized Li_6PS_5I and structural disorder was introduced. This change in morphology was verified by x-ray powder diffractometry. The samples were further investigated by means of broadband conductivity spectroscopy, ^{7}Li and ^{31}P NMR as well as ^{6}Li and ^{31}P MAS NMR. Via

broadband conductivity spectroscopy we were able to show an increase of the ionic conductivity by two orders of magnitude at ambient conditions and a concurrent significant decrease of the activation energy (T > 293 K). Charge carrier concentration and density are thought to be the reason for the boost in ionic conductivity. ^{31}P MAS NMR revealed, that all P sites are affected by the soft mechanical treatment and therefore, the whole sample volume is structurally distorted. This proves the success of this simple method. By fitting the diffusion-induced ^{7}Li and ^{31}P NMR spin-lattice relaxation rates of the nanostructured Li_6PS_5I, a change in the shape of both rates became visible in contrast to the pristine sample. For ^{7}Li a second rate peak appeared at approximately the same temperature as for the bromide analogue. We attributed this feature to long distance lithium ion diffusion, made possible by inter-cage jumping. Because the ^{31}P NMR relaxation rate peak was observed in the same region, we assumed the rotational motion of PS_4^{3-} polyanions to be in resonance with the translational motion of Li^+. In contrast to this the rotations of PS_4^{3-} are much faster in ordered Li_6PS_5I. We think that the slowed down PS_4^{3-} rotations in disordered nanocrystalline Li_6PS_5I influence lithium ion diffusion, making it faster. Overall, Li_6PS_5I is a perfect model system to investigate the influence of structural disorder on lithium ion transport.

Another research topic was the study of lithium ion hopping in the layer-structured synthetic hectorite $Li_{0.5}[Mg_{2.5}Li_{0.5}]Si_4O_{10}F_2$. This phyllosilicate served as a model for low-dimensional transport of lithium ions. Again, the methods of choice for the investigation were broadband conductivity spectroscopy, ^{7}Li NMR and ^{6}Li MAS NMR. Indeed, fast 2D ionic conduction processes were detected. ^{7}Li NMR line shape analysis showed two superimposed processes with one of them having a much lower lithium ion diffusivity. The broad component of the line shape is most likely attributed to slow lithium ions sharing a lattice position with Mg^{2+} and the narrow part originating from fast Li^+ being located between the layers of the phyllosilicate. Around 30 % of the lithium ions can take part in the fast hopping process. The activation energy of this two-dimensional ion hopping is 0.35 eV and a bulk conductivity of 0.1 mS cm^{-1} was reached.

In conclusion, for the successful implementation of solid-state batteries as energy storage systems, fundamental knowledge of ionic transport in materials is essential. The development of highly conductive electrolytes that are stable against other cell components is key. Synthesis routes, that are inexpensive and straightforward while yielding highly conductive phase pure substances, are needed. Therefore, structure - conductivity relationships must be deeply understood in order to enhance ionic conductivities via (mechano-)chemical engineering. Problems like stability issues must be solved in order to optimize production processes and not to impair battery performance. Solid-state electrolytes will play a key role in the development of energy storage systems for all kinds of applications, and thus will hopefully help to realize climate targets.

A Bibliography

[1] T. Kober, H. W. Schiffer, M. Densing, E. Panos, *Energy Strateg. Rev.* **2020**, *31*.

[2] "Paris Agreement," can be found under https://ec.europa.eu/clima/policies/international/negotiations/paris_en, (accessed on 2020-12-03)

[3] P. Knauth, *Solid State Ionics* **2009**, *180*, 911–916.

[4] J. C. Bachman, S. Muy, A. Grimaud, H. H. Chang, N. Pour, S. F. Lux, O. Paschos, F. Maglia, S. Lupart, P. Lamp, L. Giordano, Y. Shao-Horn, *Chem. Rev.* **2016**, *116*, 140–162.

[5] J. Schnell, T. Günther, T. Knoche, C. Vieider, L. Köhler, A. Just, M. Keller, S. Passerini, G. Reinhart, *J. Power Sources* **2018**, *382*, 160–175.

[6] C. H. Hamann, W. Vielstich, *Elektrochemie*, Wiley-VCH, Weihnheim, **2005**.

[7] C. Daniel, J. O. Besenhard, *Handbook of Battery Materials*, 2nd edition, Wiley-VCH, Weihnheim, **2012**.

[8] A. Cisak, L. Werblan, *High-Energy Non-Aqueous Batteries*, Ellis Horwood Ltd, Chichester, **1993**.

[9] A. J. Bard, L. R. Faulkner, *Electrochemical Methods - Fundamentals and Applications*, 2nd edition, John Wiley & Sons, Inc, NY, **2001**.

[10] G.-A. Nazri, G. Pistoia, *Lithium Batteries - Science and Technology*, Springer Science + Business Media, LLC, NY, **2009**.

[11] K. Ozawa, *Solid State Ionics* **1994**, *69*, 212–221.

[12] M. K. Gulbinska, *Lithium-ion Battery Materials and Engineering*, Springer-Verlag, London, **2014**.

[13] X. Yuan, H. Liu, J. Zhang, *Lithium-Ion Batteries Advanced Materials and Technologies*, CRC Press, Boca Raton, FL, **2012**.

[14] A. Zhou, Q. Liu, Y. Wang, W. Wang, X. Yao, W. Hu, L. Zhang, X. Yu, J. Li, H. Li, *J. Mater. Chem. A* **2017**, *5*, 24361–24370.

[15] Y. Oh, D. Ahn, S. Nam, B. Park, *J. Solid State Electrochem.* **2010**, *14*, 1235–1240.

[16] M. M. Thackeray, P. J. Johnson, L. A. de Picciotto, P. G. Bruce, J. B. Goodenough, *Mater. Res. Bull.* **1984**, *19*, 179–187.

[17] M. M. Thackeray, M. F. Mansuetto, J. B. Bates, *J. Power Sources* **1997**, *68*, 153–158.

[18] Z. Zhang, Y. Shao, B. Lotsch, Y. S. Hu, H. Li, J. Janek, L. F. Nazar, C. W. Nan, J. Maier, M. Armand, L. Chen, *Energy Environ. Sci.* **2018**, *11*, 1945–1976.

[19] Z. Gao, H. Sun, L. Fu, F. Ye, Y. Zhang, W. Luo, Y. Huang, *Adv. Mater.* **2018**, *30*, 1–27.

[20] J. Janek, W. G. Zeier, *Nat. Energy* **2016**, *1*, 1–4.

[21] V. Thangadurai, S. Narayanan, D. Pinzaru, *Chem. Soc. Rev.* **2014**, *43*, 4714–4727.

[22] R. Murugan, V. Thangadurai, W. Weppner, *Angew. Chemie - Int. Ed.* **2007**, *46*, 7778–7781.

[23] V. Thangadurai, H. Kaack, W. J. F. Weppner, J. Am. Ceram. Soc. **2003**, 86, 437–40.

[24] E. J. Cussen, *J. Mater. Chem.* **2010**, *20*, 5167–5173.

[25] H. Xie, J. A. Alonso, Y. Li, M. T. Fernández-Díaz, J. B. Goodenough, *Chem. Mater.* **2011**, *23*, 3587–3589.

[26] E. J. Cussen, *Chem. Commun.* **2006**, 412–413.

[27] V. Thangadurai, W. Weppner, *J. Solid State Chem.* **2006**, *179*, 974–984.

[28] J. Awaka, N. Kijima, H. Hayakawa, J. Akimoto, *J. Solid State Chem.* **2009**, *182*, 2046–2052.

[29] H. Buschmann, J. Dölle, S. Berendts, A. Kuhn, P. Bottke, M. Wilkening, P. Heitjans, A. Senyshyn, H. Ehrenberg, A. Lotnyk, V. Duppel, L. Kienle, J. Janek, *Phys. Chem. Chem. Phys.* **2011**, *13*, 19378–19392.

[30] R. Wagner, G. J. Redhammer, D. Rettenwander, A. Senyshyn, W. Schmidt, M. Wilkening, G. Amthauer, *Chem. Mater.* **2016**, *28*, 1861–1871.

[31] N. Bernstein, M. D. Johannes, K. Hoang, *Phys. Rev. Lett.* **2012**, *109*, 1–5.

[32] W. G. Zeier, *Dalt. Trans.* **2014**, *43*, 16133–16138.

[33] Q. Liu, Z. Geng, C. Han, Y. Fu, S. Li, Y. bing He, F. Kang, B. Li, *J. Power Sources* **2018**, *389*, 120–134.

[34] M. Nyman, T. M. Alam, S. K. McIntyre, G. C. Bleier, D. Ingersoll, *Chem. Mater.* **2010**, *22*, 5401–5410.

[35] L. Truong, V. Thangadurai, *Chem. Mater.* **2011**, *23*, 3970–3977.

[36] C. Ma, E. Rangasamy, C. Liang, J. Sakamoto, K. L. More, M. Chi, *Angew. Chemie - Int. Ed.* **2015**, *54*, 129–133.

[37] L. Cheng, W. Chen, M. Kunz, K. Persson, N. Tamura, G. Chen, M. Doeff, *ACS Appl. Mater. Interfaces* **2015**, *7*, 2073–2081.

[38] Z. F. Yow, Y. L. Oh, W. Gu, R. P. Rao, S. Adams, *Solid State Ionics* **2016**, *292*, 122–129.

[39] R. H. Brugge, A. K. O. Hekselman, A. Cavallaro, F. M. Pesci, R. J. Chater, J. A. Kilner, A. Aguadero, *Chem. Mater.* **2018**, *30*, 3704–3713.

[40] K. Hofstetter, A. J. Samson, S. Narayanan, V. Thangadurai, *J. Power Sources* **2018**, *390*, 297–312.

[41] H. M. Chen, C. Maohua, S. Adams, *Phys. Chem. Chem. Phys.* **2015**, *17*, 16494–16506.

[42] H. J. Deiseroth, S. T. Kong, H. Eckert, J. Vannahme, C. Reiner, T. Zaiß, M. Schlosser, *Angew. Chemie - Int. Ed.* **2008**, *47*, 755–758.

[43] I. Hanghofer, B. Gadermaier, H. M. R. Wilkening, *Chem. Mater.* **2019**, *31*, 4591–4597.

[44] P. R. Rayavarapu, N. Sharma, V. K. Peterson, S. Adams, *J. Solid State Electrochem.* **2012**, *16*, 1807–1813.

[45] I. Hanghofer, M. Brinek, S. L. Eisbacher, B. Bitschnau, M. Volck, V. Hennige, I. Hanzu, D. Rettenwander, H. M. R. Wilkening, **2019**, *12*, 8489–8507.

[46] M. A. Kraft, S. P. Culver, M. Calderon, F. Böcher, T. Krauskopf, A. Senyshyn, C. Dietrich, A. Zevalkink, J. Janek, W. G. Zeier, *J. Am. Chem. Soc.* **2017**, *139*, 10909–10918.

[47] M. A. Kraft, S. Ohno, T. Zinkevich, R. Koerver, S. P. Culver, T. Fuchs, A. Senyshyn, S. Indris, B. J. Morgan, W. G. Zeier, *J. Am. Chem. Soc.* **2018**, *140*, 16330–16339.

[48] S. Ohno, B. Helm, T. Fuchs, G. Dewald, M. A. Kraft, S. P. Culver, A. Senyshyn, W. G. Zeier, *Chem. Mater.* **2019**, *31*, 4936–4944.

[49] L. Zhou, A. Assoud, Q. Zhang, X. Wu, L. F. Nazar, *J. Am. Chem. Soc.* **2019**, *141*, 19002–19013.

[50] R. J. D. Tilley, *Defects in Solids*, John Wiley & Sons, Hoboken, New Jersey, **2008**.

[51] P. Heitjans, J. Kärger, *Diffusion in Condensed Matter Methods, Materials, Models*, Springer-Verlag Berlin Heidelberg, **2005**.

[52] H. Mehrer, *Diffusion in Solids Fundamentals, Methods, Materials, Diffusion-Controlled Processes*, Springer-Verlag Berlin Heidelberg, **2007**.

[53] P. J. Gellings, H.J.M. Bouwmeester *The CRC Handbook of Solid State Electrochemistry*, CRC Press Inc., Boca Raton, FL, **1997**.

[54] C. B. Carter, M. G. Norton, *Ceramic Materials: Science and Engineering*, Springer Science+Business Media, LLC., NY, **2007**.

[55] H. Ibach, H. Lüth, *Solid-State Physics An Introduction to Principles of Materials Science*, 4th edition, Springer-Verlag Berlin Heidelberg, **2009**.

[56] M. A. Alim, *Immittance Spectroscopy Applications to Material Systems*, John Wiley & Sons, Inc, Hoboken, NJ, **2018**.

[57] B. J. T. S. Irvine, D. C. Sinclair, A. R. West, Adv. Mater. **1990**, *2*, 132–138.

[58] V. F. Lvovich, *Impedance Spectroscopy Applications to Electrochemical and Dielectric Phenomena*, John Wiley & Sons, Inc, Hoboken, NJ, **2012**.

[59] E. Barsoukov, J. R. Macdonald, *Impedance Spectroscopy Theory, Experiment , and Applications*, 2nd edition, John Wiley & Sons, Inc, Hoboken, NJ, **2005**.

[60] M. E. Orazem, B. Tribollet, *Electrochemical Impedance Spectroscopy*, 2nd edition, John Wiley & Sons, Inc, Hoboken, NJ, **2017**.

[61] F. Preishuber-Pflügl, M. Wilkening, *Dalt. Trans.* **2016**, *45*, 8675–8687.

[62] D. L. Sidebottom, B. Roling, K. Funke, *Phys. Rev. B - Condens. Matter Mater. Phys.* **2000**, *63*, 1–7.

[63] S. Breuer, D. Prutsch, Q. Ma, V. Epp, F. Preishuber-Pflügl, F. Tietz, M. Wilkening, *J. Mater. Chem. A* **2015**, *3*, 21343–21350.

[64] D. L. Sidebottom, *Rev. Mod. Phys.* **2009**, *81*, 999–1014.

[65] A. K. Jonscher, *Nature* **1977**, *267*, 673–679.

[66] D. Almond, G. Duncan, A. West, *Solid State Ionics* **1983**, *8*, 159–164.

[67] J. C. Dyre, P. Maass, B. Roling, D. L. Sidebottom, *Reports Prog. Phys.* **2009**, *72*.

[68] M. Brinek, C. Hiebl, H. M. R. Wilkening, *Chem. Mater.* **2020**, *32*, 4754–4766.

[69] M. H. Levitt, *Spin Dynamics Basics of Nuclear Magnetic Resonance*, 2nd edition, John Wiley & Sons Ltd., Chichester, England, **2008**.

[70] H. Friebolin, *Basic One-and Two-Dimensional NMR Spectroscopy*, 5th edition, Wiley-VCH Verlag, Weinheim, **2011**.

[71] M. J. Duer, *Solid-State NMR Spectroscopy*, Blackwell Publishing Ltd, Garsington, UK, **2004**.

[72] J. Keeler, *Understanding NMR Spectroscopy*, John Wiley & Sons Ltd., Chichester, England, **2005**.

[73] A. Abragam, *Principles of Nuclear Magnetism*, Oxford University Press, Oxford, **1961**.

[74] G. Schatz, A. Weidinger, *Nukleare Festkörperphysik Kernphysikalische Meßmethoden Und Ihre Anwendungen*, 3. Auflage, B.G. Teubner, Stuttgart, **1997**.

[75] A. Kuhn, M. Kunze, P. Sreeraj, H. D. Wiemhöfer, V. Thangadurai, M. Wilkening, P. Heitjans, *Solid State Nucl. Magn. Reson.* **2012**, *42*, 2–8.

[76] M. Uitz, V. Epp, P. Bottke, M. Wilkening, *J. Electroceramics* **2017**, *38*, 142–156.

[77] N. Bloembergen, E. M. Purcell, R. V. Pound, *Phys. Rev.* **1948**, *73*, 679–712.

[78] M. Wilkening, P. Heitjans, *ChemPhysChem* **2012**, *13*, 53–65.

[79] M. Ladd, R. Palmer, *Structure Determination by X-Ray Crystallography* - Analysis by X-rays and Neutrons, 5th edition, Springer Science+Business Media, NY, **2013**.

[80] V. K. Pecharsky, P. Y. Zavalij, *Fundamentals of Powder Diffraction and Structural Characterization of Materials*, 2nd edition, Springer Science+Business Media, LLC, NY, **2009**.

[81] W. Massa, *Crystal Structure Determination*, Springer-Verlag Berlin Heidelberg, **2000**.

[82] T. Oeser, *Kristallstrukturanalyse durch Röntgenbeugung Spektroskopiekurs kompakt*, Springer Fachmedien Wiesbaden GmbH, Wiesbaden, **2019**.

[83] L. Spieß, G. Teichert, R. Schwarzer, H. Behnken, C. Genzel, *Moderne Röntgenbeugung Röntgendiffraktometrie Für Materialwissenschaftler, Physiker Und Chemiker*, 3. Auflage, Springer Fachmedien Wiesbaden GmbH, Wiesbaden, **2019**.

[84] W. Borchardt-Ott, H. Sowa, *Kristallographie Eine Einführung Für Studierende Der Naturwissenschaften*, 9. Auflage, Springer-Verlag Berlin Heidelberg, **2018**.

[85] I. Hanghofer, M. Brinek, S. L. Eisbacher, B. Bitschnau, M. Volck, V. Hennige, I. Hanzu, D. Rettenwander, H. M. R. Wilkening, *Phys. Chem. Chem. Phys.* **2019**, *21*, 8489–8507.

B Publications

B.1 Publications in peer-reviewed journals

Proton Bulk Diffusion in Cubic $Li_7La_3Zr_2O_{12}$ Garnets as Probed by Single X-ray Diffraction
C. Hiebl, D. Young, R. Wagner, H. M. R. Wilkening, G. J. Redhammer, and D. Rettenwander
The Journal of Physical Chemistry C **2019** *123* (2), 1094-1098

Rapid Low-Dimensional Li^+ Ion Hopping Processes in Synthetic Hectorite-Type $Li_{0.5}[Mg_{2.5}Li_{0.5}]Si_4O_{10}F_2$
C. Hiebl, P. Loch, M. Brinek, M. Gombotz, B. Gadermaier, P. Heitjans, J. Breu, and H. M. R. Wilkening
Chemistry of Materials **2020** *32* (17), 7445-7457

Understanding the Origin of Enhanced Li-Ion Transport in Nanocrystalline Argyrodite-Type Li_6PS_5I
M. Brinek, C. Hiebl, and H. M. R. Wilkening
Chemistry of Materials **2020** *32* (11), 4754-4766

Structural Disorder in Li_6PS_5I Speeds ^7Li Nuclear Spin Recovery and Slows Down ^{31}P Relaxation–Implications for Translational and Rotational Jumps as Seen by Nuclear Magnetic Resonance
M. Brinek, C. Hiebl, K. Hogrefe, I. Hanghofer, and H. M. R. Wilkening
The Journal of Physical Chemistry C **2020** *124* (42), 22934-22940

B.2 Oral Presentations

Lithium-Ion Transport in Mechanochemically Synthesized Nanocrystalline Garnets
C. Hiebl, M. Uitz, D. Rettenwander, and H. M. R. Wilkening
International Conference on Functional Nanomaterials and Nanodevices, September 24-27, 2017 Budapest, Hungary

The impact of humidity and aqueous solutions on the structural and ion dynamical properties of cubic $Li_7La_3Zr_2O_{12}$ garnets studied on single crystals
C. Hiebl, D. Young, M. Gombotz, R. Wagner, S. Ganschow, M. Meven, G. J. Redhammer, D. Rettenwander, and H. M. R. Wilkening
*DocDays 2019***,** April 24-25, 2019, Graz, Austria

B.3 Poster Presentations

Degradation of Li-Oxide Garnets in Humidity, Air and Aqueous Solutions: A Study using a large $Li_6La_3ZrTaO_{12}$ Single Crystal
C. Hiebl, S. Smetacek, M. Gombotz, S. Berendts, R. Uecker, G. Redhammer, A. Limbeck, J. Fleig, D. Rettenwander, and H. M. R. Wilkening
AiMES, September 30 - October 4, 2018, Cancun, Mexico

The Impact of Humidity and Aqueous Solutions on the Structural and Ion Dynamical Properties of cubic $Li_7La_3Zr_2O_{12}$ Garnets studied on Single Crystals
C. Hiebl, D. Young, M. Gombotz, R. Wagner, S. Ganschow, M. Meven, G. J. Redhammer, D. Rettenwander and H. M. R. Wilkening
$F^2c\pi^2$, July 14 - 19, 2019, Lausanne, Switzerland

C Acknowledgement

Zuallererst möchte ich mich bei Prof. Dr. Martin Wilkening bedanken, der mir die Möglichkeit für meine Dissertation am Institut für Chemische Technologie von Materialien (ICTM) an der TU Graz gegeben hat. Er schuf eine beispiellos gute Umgebung für seine Mitarbeiter indem er nötige Freiräume schuf und wertvolle wissenschaftliche Hilfestellungen gab. Ich hatte über all die Jahre das Gefühl, immer ein offenes Ohr zu bekommen und bei allen Problemstellungen unterstützt zu werden. Weiters möchte ich mich bei Dr. Daniel Rettenwander für seine kreativen Ideen und sein geteiltes Know-how bedanken. Auch Dr. Ilie Hanzu stand mir jederzeit mit Rat zur Seite, vielen Dank.

Überdies gilt mein großer Dank den aktuellen und ehemaligen Mitgliedern der Arbeitsgruppe. Die Zeit mit euch am Institut, sowie auf Konferenzen bleibt unvergesslich. Man konnte sich immer auf Unterstützung verlassen und der Zusammenhalt war außerordentlich. Im Besonderen möchte ich mich bei meinen Bürokollegen Marina Brinek, Maria Gombotz und Roman Zettl bedanken. Ich fand in euch nicht nur Arbeitskollegen, sondern auch gute Freunde, die einem in jedem Hoch und Tief in diesen Jahren stets zur Seite standen.

Abseits von der Universität möchte ich noch meinen großen Dank meinen Eltern, Großeltern und meinem Freund Alexander gegenüber aussprechen. Sie haben mich all die Jahre stets unterstützt und mir den nötigen Rückhalt gegeben.